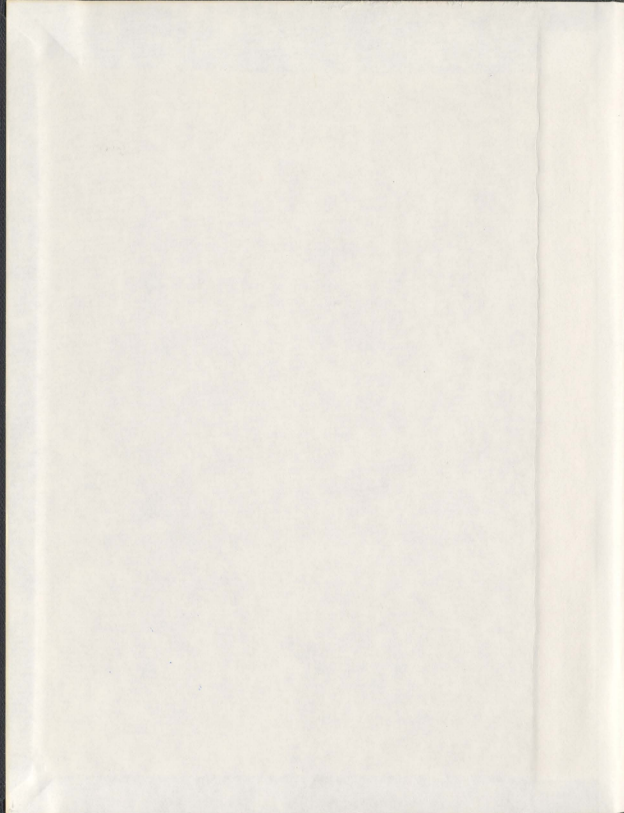


STRUCTURES OF METAL-DICATION/URACIL COMPLEXES
IN THE GAS AND MATRIX ISOLATED-HYDROGEN
BONDED COMPLEXES

OSAMA YOUSEF ALI



001311



**Structures of Metal-Dication/Uracil Complexes in
the Gas Phase and Matrix Isolated-Hydrogen
Bonded Complexes**

by

Osama Yousef Ali

A thesis submitted to the
School of Graduate Studies
in partial fulfillment of the
requirements for the degree of

Doctor of Philosophy

Department of Chemistry
Memorial University of Newfoundland

October, 2011

St. John's

Newfoundland

Abstract

Ionic complexes have long been studied by mass spectrometry while leisurely spectroscopic studies of neutral complexes can be studied using matrix isolation spectroscopy. Experimental results aiming to elucidate the structures of neutral and ionic complexes are often complemented by electronic structure calculations as has been done in this work.

Complexes of divalent metal ions and uracil have been investigated using FTICR mass spectrometry. Positive ion electrospray mass spectra show that $[M(\text{Ura-H})(\text{Ura})]^+$, where M is formally a divalent metal ion, are the most abundant ions even at low concentrations of uracil. MS/MS experiments show that the lowest energy decomposition pathway for $[M(\text{Ura-H})(\text{Ura})]^+$ complexes is loss of HNC O for all metals studied with the exception of Sr, Ba and Pb which do lose a molecule of uracil. The computed binding energies between neutral uracil and $[M(\text{Ura-H})]^+$, M= Zn, Cu, Ni, Fe, Cd, Pd, Mg, Ca, Sr, Ba, and Pb have also been calculated and are consistent with the experimentally-observed differences in fragmentation pathways. The potential energy surfaces associated with the fragmentation pathways of $[\text{Cu}(\text{Ura-H})(\text{Ura})]^+$ were computed to help explain the collision induced dissociation spectra.

Complexes of uracil and Pb^{2+} , as well the water-solvated complexes have been studied by infrared multiple photon dissociation (IRMPD) spectroscopy in the N-H and O-H stretching region. The computed IR spectra for the lowest energy structures are consistent with the experimental IRMPD spectrum. The experimental spectra for $[\text{Pb}(\text{Ura-H})(\text{H}_2\text{O})_n]^+$ ($n=1-2$) revealed that the first water molecule binds to the lead ion

and indicates the presence of intramolecular hydrogen bonding to a carbonyl of uracil. The second molecule of water also attaches directly to the lead ion, but does not participate in any hydrogen bonding.

The infrared absorption spectra of hydrogen-bonded complexes of propylene oxide with either ethanol or 2-fluoroethanol have been recorded in neon matrices. The results indicate that hydrogen-bonded complexes were formed with propylene oxide as the hydrogen bond acceptor and either ethanol or 2-fluoroethanol as the hydrogen bond donors. The features assigned to the O-H stretch were red-shifted by 175 cm^{-1} and 193 cm^{-1} for ethanol and 2-fluoroethanol containing complexes. From the peak shifts and the comparison with the calculations, a 1:1 propylene oxide/ethanol and propylene oxide/2-fluoroethanol complexes are formed.

Acknowledgement

I would like to offer my thanks to the people who have helped me along the way to make this thesis possible. I would like to express my deepest gratitude to my supervisor, Dr. Travis Fridgen, who introduced me to fascinating fields of Matrix Isolation and FTICR mass spectrometry. His support, encouragement, and advice have been a great help during these years. Also, his kindnesses, valuable guidance, and endless hours of help and contribution have made this a remarkable learning experience.

I would like to thank my supervisory committee, Dr. Peter Pickup and Dr. Christina Bottaro, for their help and suggestions. I would like to thank our research group, for their continual support, help and encouragements throughout my program.

Finally, and most importantly, I would like to express my deepest gratitude for the continuous support and encouragement that I received from my parents, my love, and brothers and sisters. This work would never have been completed without their support. Also, I cannot forget to thank my friends who have helped throughout my program.

Contents

Table of Contents

Title Page	i
Abstract	ii
Acknowledgement	iv
Table of Contents	vi
List of Figures	x
List of Tables	xvi
List of Schemes	xvii
List of Abbreviations	xviii
Co-Authorship Statement	xx
1. Introduction	1
1.1. General Introduction	1
1.2 Mass Spectrometric Techniques for Studying the Structures of Gaseous Ions	2
1.2.1 Fourier Transform Ion Cyclotron Resonance (FT-ICR) Mass Spectrometry	3
1.2.2 Fragmentation Processes in the FTICR	8
1.2.2.1 Collision-Induced Dissociation (CID) method	8
1.2.2.1.1 CID External to ICR cell	9
1.2.2.1.2 SORI/CID	14
1.2.2.2 Infrared Multiple Photon Dissociation (IRMPD)	15
1.2.3 Infrared Multiple Photon Dissociation (IRMPD) Spectroscopy	19
1.3 The Matrix Isolation Technique for Studying Weakly Intermolecular Complexes	20

1.3.2 The Matrix Isolation Technique.....	22
1.3.2.1 Sample Preparation	22
1.3.3.2 Closed-Cycle Refrigerator	24
1.3.2.3 Sample Deposition	25
1.3.3 Spectroscopic Techniques of Matrix Isolated Species.....	25
1.3.3.1 FTIR	26
1.3.3.2 Annealing Method.....	31
1.3.3.3 Molecular Complexes in Inert Gas Matrices	31
1.4 Pyrimidic Nucleobases.....	36
1.4.1 Nucleic Acid Bases	36
1.4.2 Hydrogen Bonding in Base-Pairing	38
1.4.3 Uracil.....	40
1.4.3.1 Chemical and Physical Properties	40
1.4.3.2 Tautomerization	41
1.5 Theoretical Methods.....	43
1.5.1 Ab initio	43
1.5.2 Density Functional Theory (DFT)	44
1.5.3 Basis Set	46
1.5.4 Computational Procedure.....	46
1.6 References	49
2. Structures and Fragmentation of [Cu(Uracil-H)(Uracil)]⁺ in the Gas Phase.....	58
2.1. Introduction.....	58
2.2. Methods.....	61
2.2.1 Experimental	61

2.2.2 Computational	62
2.3. Result and Discussion	63
2.3.1 Positive Ion Electrospray Spectra of Copper (II)/ Nucleobase Solutions.....	63
2.3.2 Results of Fragmentation Experiments on [Cu(Ura-H)(Ura)] ⁺	65
2.3.2.1 MS ⁿ Experiments on [Cu(Ura-H)(Ura)] ⁺	66
2.3.2.2 MS ⁿ Experiments with 2- ¹³ C Labeled Uracil.....	68
2.3.2.3 MS ⁿ Experiments with 3- ¹⁵ N and 1,3- ¹⁵ N Labeled Uracil.....	70
2.3.2.4 MS ⁿ Experiments with 5-d- and 6-d- Labeled Uracil	72
2.3.2.5 IRMPD Experiments	73
2.3.3 Discussion	75
2.3.3.1 [Cu(Ura-H)(Ura)] ⁺ Structures	75
2.3.3.2 Mechanistic Aspects of [Cu(Ura-H)(Ura)] ⁺ CID	80
2.4. Conclusions.....	87
2.5 Acknowledgments.....	87
2.6 References	88
3. Fragmentation Pathways of Gas Phase [M(Uracil-H)(Uracil)]⁺ Complexes (M= Zn, Cu, Ni, Co, Fe, Mn, Cd, Pd , Mg, Ca, Sr, Ba, and Pb).....	91
3.1. Introduction	91
3.2. Methods.....	94
3.2.1 Experimental	94
3.2.2 Computational	95
3.3. Results and Discussion.....	96
3.3.1 SORI/CID spectra of [M(Ura)(Ura-H)] ⁺	97

3.3.2 IRMPD dissociation of $[M(\text{Ura-H})(\text{Ura})]^+$	101
3.4. Computational study	104
3.5. Conclusion.....	110
3.6 References	112
4. Structures of Electrosprayed Pb(Uracil-H)⁺ Complexes by Infrared Multiple Photon Dissociation Spectroscopy	115
4.1. Introduction	115
4.2. Methods.....	118
4.2.1 Experimental	118
4.2.2 Computational	119
4.3. Results and Discussion.....	119
4.3.1. Comparison of IRMPD Spectra of $[\text{Pb}(\text{Ura-H})(\text{Ura})]^+$, $[\text{Pb}(\text{Ura-H})(\text{H}_2\text{O})]^+$, and $[\text{Pb}(\text{Ura-H})(\text{H}_2\text{O})_2]^+$	119
4.3.2. $[\text{Pb}(\text{Ura-H})(\text{Ura})]^+$	122
4.3.3. $[\text{Pb}(\text{Ura-H})(\text{H}_2\text{O})]^+$	126
4.3.4. $[\text{Pb}(\text{Ura-H})(\text{H}_2\text{O})_2]^+$	129
4.3.5 Structure of $[\text{Pb}(\text{Ura-H})]^+$	133
4.4. Summary	136
4.5. Acknowledgements	136
4.6 References	137
5. Infrared Characterization of Hydrogen-Bonded Propylene Oxide/Ethanol and Propylene Oxide/ 2-Fluoroethanol Complexes Isolated in Solid Neon Matrices	141
5.1. Introduction	141
5.2. Methods.....	144

5.2.1. Experimental	144
5.2.2. Computational	145
5.3. Results and Discussion	147
5.3.1. Infrared Spectra of Ethanol, d ₆ -Ethanol, and Propylene Oxide: A Scaling "Equation"	147
5.3.2. The Ethanol-Propylene Oxide Hydrogen Bonded Complex	154
5.3.3. The 2-Fluoroethanol-Propylene Oxide Hydrogen Bonded Complex	163
5.3.4. Towards a "Universal" Correlation of the Position of the Hydrogen Bonded OH (XH) Stretch in Hydrogen Bonded Complexes	167
5.4. Conclusions	173
5.5. Acknowledgments	174
5.6. References	175
6. Conclusion and Future work	181
Appendix	186

List of Figures	X
Figure 1.1. Cyclotron motion of positively charged ion moving in the magnetic field	4
Figure 1.2. Steps in ion excitation and detection in a FTICR MS	6
Figure 1.3. Electrospray ionization process	7
Figure 1.4. Schematic of 7.0 T FT-ICR mass spectrometer. Figure reproduced from J. Am. Soc. Mass Spectrom. 2009, 20, 411 with permission from Elsevier.....	7
Figure 1.5. Fragmentation of $[M+H]^+$ of tryptophan under conditions a) collision induced dissociation (CID) and (b) electron-induced dissociation (EID) 23 eV. Figure reproduced from Anal. Bioanal. Chem. 2007, 389, 1429 with permission from Springer.10	
Figure 1.6. CID spectrum of protonated uracil. Figure reproduced from J. Am. Soc. Mass Spectrom. 1994, 5, 339 with permission from Elsevier	12
Figure 1.7. (a) Schematic representation of IRMPD mechanism and (b) vibrational state density in a molecular ion	17
Figure 1.8. (a) CID and (b) IRMPD of protonated erythromycin A. Figure reproduced from J. Am. Soc. Mass Spectrom. 2002, 13, 630 with permission from Elsevier.....	18
Figure 1.9. Diagram representing, a guest species (in black circle) isolated in solid host matrix (in open circle)	21
Figure 1.10. Schematic of gas-handling apparatus used for preparation of gas samples for matrix isolation experiments	23
Figure 1.11. IR spectra of the SO_2 (symmetric stretch) near 1150 cm^{-1} (a) in the gas phase at room temperature, and (b) matrix isolated in N_2 at 12 K ($N_2: SO_2 = 100:1$). Dunkin, I. R. <i>Matrix isolation techniques: a practical approach</i> ; Oxford University; New York, 1998	29
Figure 1.12. Portion of the FT-infrared spectrum of methanol isolated in N_2 , Ar, Kr and Xe showing the effect of different environments on the CO stretching fundamental. The vertical line shows the position of the vapour-phase band centre. Figure reproduced	

from, Travis D. Fridgen, PhD thesis; Queen's University; Canada, 1999, with permission from the author.....	30
Figure 1.13. T FT-infrared spectra of argon matrices containing water($1:10^3$ H ₂ O/Ar) and $1:10^3$ (A), $1:3 \times 10^2$ (B), $1:10^2$ (C), $1:50$ (D) acetone/Ar, in the region 3800-3450 and 1645-1560 cm^{-1} . Figure reproduced from J. Phys. Chem. 1993, 97, 4320 with permission from American Chemical Society.....	33
Figure 1.14. FTIR spectrum for uracil/Ar (A) and uracil/HCl/Ar (B, C) at 12 K. (B, HCl/Ar =1/200; C annealed of B). Figure reproduced from J. Mol. Struct. 1994, 318, 37 with permission from Elsevier.....	35
Figure 1.15. Structures of the common pyrimidine and purine bases of nucleic acids...37	
Figure 1.16. Watson-Crick base pairing for A-T and G-C.....	39
Figure 1.17. The six possible tautomer of uracil.....	42
Figure 2.1. Positive-ion electrospray mass spectrum of an aqueous solution of CuCl ₂ and uracil.....	64
Figure 2.2A. MS/MS spectra of $[\text{Cu}(\text{Ura})(\text{Ura-H})]^+$ complex were recorded at different SORI collision energies; a) 0.39 b) 0.66 c) 0.99 , and d) 1.39 eV (c.o.m.) by using SORI method in fragmentation.....	66
Figure 2.2B. SORI MS/MS of the main fragment ions (i) m/z 286 (ii) m/z 243 (iii) m/z 216, and (iv) 174.....	68
Figure 2.2C. SORI MS/MS of the main fragment ions of $[\text{Cu}(\text{Ura}-2\text{-}^{13}\text{C})_2\text{-H}]^+$ (i) m/z 288 (ii) m/z 244 (iii) m/z 217, and (iv) 175.....	70
Figure 2.2D. SORI MS/MS of the main fragment ions of $[\text{Cu}(\text{Ura}-3\text{-}^{15}\text{N})_2\text{-H}]^+$ (i) m/z 288 (ii) m/z 244 (iii) m/z 217, and (iv) 175.....	71
Figure 2.2E. SORI MS/MS of the main fragment ions of $[\text{Cu}(\text{Ura-d}5)_2\text{-H}]^+$ (i) m/z 288 (ii) m/z 244 (iii) m/z 217, and (iv) 175.....	74
Figure 2.2F. SORI MS/MS of the main fragment ions of $[\text{Cu}(\text{Ura-d}6)_2\text{-H}]^+$ (i) m/z 288 (ii) m/z 244 (iii) m/z 217, and (iv) 175.....	74

Figure 2.3. Isomers of $[\text{Cu}(\text{Ura-H})]^+$ as determined by theoretical methods as well as B3LYP/6-311+G(2df,2p) calculated Gibbs free energies, the relative enthalpies in parentheses. The Gibbs energies and the enthalpies in parentheses in <i>italic</i> are for the solvent-phase calculations.....	77
Figure 2.4. Nine of the lowest energy $[\text{Cu}(\text{Ura-H})(\text{Ura})]^+$ structures, of the twenty-seven computed structures (see Appendix 4 for all structures). Enthalpies and Gibbs energies (parentheses) are computed at the MP2/6-311+G(2df,2p)//B3LYP/6-31+G(d,p) level of theory and are in kJ mol^{-1} relative to the lowest energy structure.....	79
Figure 2.5. Potential energy surface corresponding to manipulating the lowest energy possible structure to the complex N1/O2 (N1-O2)	81
Figure 2.6. Proposed fragmentation pathways for the observed fragments from $[\text{Cu}(\text{Ura-H})(\text{Ura})]^+$	82
Figure 2.7. The proposed neutral fragments with origin in a lowest energy structure $[\text{Cu}(\text{Ura-H})(\text{Ura})]^+$. Relative Gibbs energy level diagram with respect to the lowest energy structure are in kJ/mol	86
Figure 3.1 A. SORI/CID spectra of the $[\text{M}(\text{Ura-H})(\text{Ura})]^+$ complex obtained with (i) $[\text{Zn}(\text{Ura-H})(\text{Ura})]^+$, (ii) $[\text{Cu}(\text{Ura-H})(\text{Ura})]^+$, (iii) $[\text{Ni}(\text{Ura-H})(\text{Ura})]^+$ and (iv) $[\text{Co}(\text{Ura-H})(\text{Ura})]^+$ recorded with a SORI power 0.656 eV	98
Figure 3.1 B. SORI/CID spectra of the $[\text{M}(\text{Ura-H})(\text{Ura})]^+$ complex obtained with (i) $[\text{Fe}(\text{Ura-H})(\text{Ura})]^+$, (ii) $[\text{Mn}(\text{Ura-H})(\text{Ura})]^+$, (iii) $[\text{Cd}(\text{Ura-H})(\text{Ura})]^+$ and (iv) $[\text{Pd}(\text{Ura-H})(\text{Ura})]^+$ recorded with a SORI power 0.656 eV	99
Figure 3.1 C. SORI/CID spectra of the $[\text{M}(\text{Ura-H})(\text{Ura})]^+$ complex obtained with (i) $[\text{Mg}(\text{Ura-H})(\text{Ura})]^+$, (ii) $[\text{Ca}(\text{Ura-H})(\text{Ura})]^+$, (iii) $[\text{Sr}(\text{Ura-H})(\text{Ura})]^+$, (iv) $[\text{Ba}(\text{Ura-H})(\text{Ura})]^+$, (v) $[\text{Pb}(\text{Ura-H})(\text{Ura})]^+$ recorded with a SORI power 0.656 eV.....	100
Figure 3.2: (i) SORI/CID spectrum of the $[\text{Ca}(\text{Ura-H})(\text{Ura})]^+$ complex obtained with a SORI power 0.656 eV, (ii) IRMPD spectrum of the $[\text{Ca}(\text{Ura-H})(\text{Ura})]^+$ complex.....	102

Figure 3.3. (a) Proposed energy profile for loss of HNCO and uracil from $[\text{Ca}(\text{Ura-H})(\text{Ura})]^+$ and (b) a rate constant vs internal energy scheme corresponding to the proposed energy profile in (a)	103
Figure 3.4. A plot between the computed uracil binding energies vs. the effective ionic radius of the M^{2+} ion	110
Figure 4.1. Comparison of the IRMPD spectra of $[\text{Pb}(\text{Ura-H})(\text{Ura})]^+$, $[\text{Pb}(\text{Ura-H})(\text{H}_2\text{O})]^+$, and $[\text{Pb}(\text{Ura-H})(\text{H}_2\text{O})_2]^+$	121
Figure 4.2. Eight of the lowest-energy structures of $[\text{Pb}(\text{Ura-H})(\text{Ura})]^+$. The 298 K relative enthalpies and Gibbs free energies (in parentheses) reported in kJ mol^{-1} were calculated at the MP2/6-311++G(2d,p)//B3LYP/6-31+G(d,p) level of theory. All species have a single positive charge.....	123
Figure 4.3. Experimental IRMPD spectra of $[\text{Pb}(\text{Ura-H})(\text{Ura})]^+$ compared with B3LYP/6-31+G(d,p) spectra for $[\text{Pb}(\text{Ura})(\text{Ura-H})]^+$ structures shown in Figure 4.2	125
Figure 4.4. Seven computed structures for $[\text{Pb}(\text{Ura-H})(\text{H}_2\text{O})]^+$. The 298 K, MP2/6-311+G(2d,p)//B3LYP/6-31++G(d,p) relative enthalpies, and Gibbs energies (in parentheses) in kJ mol^{-1} are provided for each structure. All species have a single positive charge	127
Figure 4.5. Comparison of the experimental IRMPD spectrum for $[\text{Pb}(\text{Ura-H})(\text{H}_2\text{O})]^+$ and the predicted IR spectra for the computed structures in Figure 4.4	129
Figure 4.6. B3LYP/6-31+G(d,p) structures of five $[\text{Pb}(\text{Ura-H})(\text{H}_2\text{O})_2]^+$ structures. The 298 K, MP2/6-311++G(2d,p)//B3LYP/6-31+G(d,p) relative enthalpies and Gibbs energies (in parentheses) in kJ mol^{-1} are provided. All species have a single positive charge	132
Figure 4.7. The IRMPD spectrum for $[\text{Pb}(\text{Ura-H})(\text{H}_2\text{O})_2]^+$ in the 3200-3900 cm^{-1} range compared to the computed spectra for the five complexes shown in Figure 4.6	133
Figure 4.8. Three lowest energy B3LYP/6-31+G(d,p) structures for $[\text{Pb}(\text{Ura-H})]^+$. The 298 K, MP2/6-311++G(2d,p)//B3LYP/6-31+G(d,p) relative enthalpies and Gibbs	

energies (in parentheses) as well as the B3LYP/6-31+G(d,p) energies (in italics top), all in kJ/ mol are provided. All species have a single positive charge.....	135
Figure 5.1. Schematic of matrix isolation instrumentation showing the optical configuration for FT-infrared spectroscopy.....	146
Figure 5.2: FTIR spectrum of neon matrix isolated propylene oxide in the 700 to 1550 cm^{-1} and 2900 to 3100 cm^{-1} range.....	150
Figure 5.3: Six conformers of the ethanol-propylene oxide hydrogen bonded complex. The MP2/6-311++G(2d,2p)//B3LYP/6-311++G(2d,2p) relative free energies and (enthalpies) in kJ mol^{-1} are also provided.....	154
Figure 5.4. A) Infrared spectra in the 3350-3650 cm^{-1} region of mixtures deposited at 4.2 K, (a) ethanol: neon 1:3000 (b) propylene oxide: neon 1:200, and at the ethanol: propylene oxide ratios in neon of (c) 1:2:3000 (d) 1:3.3:3000 (e) 1:5:3000, and (f) 1:15:3000. B) Infrared spectra in the the 3350-3650 cm^{-1} region of mixture deposited at 4.2 k, (i) EtOH/PO/Ne 1:15:3000, (ii-vii) the predicted frequencies of OH mode in all possible geometries of EtOH/PO complexes.....	156
Figure 5.5. Neon matrix infrared spectra of a) 1 part in 200 propylene oxide, b) 1 part in 3000 ethanol and c) 1:15:3000 ethanol:propylene oxide:neon in the 500 to 920 cm^{-1} region.....	157
Figure 5.6. Neon matrix infrared spectra of i) 1 part in 200 propylene oxide, ii) 1 part in 3000 ethanol and iii) 1:15:3000 ethanol:propylene oxide:neon in the 1025 to 1400 cm^{-1} regions. Also shown are the computed spectra for the a) AntiG+, b) AntiG-, c) AntiT, d) SynG+, e) SynG-, and f) SynT structures.....	159
Figure 5.7. FTIR spectra in the 2500 to 2700 cm^{-1} region of a) 1 part in 200 propylene oxide, b) 1 part in 3000 d6-ethanol and c) 1:15:3000 d6-ethanol:propylene oxide:neon as well as the computed spectra for the six hydrogen bonded complexes.....	161
Figure 5.8. Neon matrix infrared spectra of i) 1 part in 200 propylene oxide, ii) 1 part in 3000 d6-ethanol and iii) 1:15:3000 d6-ethanol:propylene oxide:neon in the 1025 to 1400	

cm⁻¹ regions. Also shown are the computed spectra for the a) AntiG+, b) AntiG-, c) AntiT, d) SynG+, e) SynG-, and f) SynT structures 162

Figure 5.9. FTIR spectra in the 3300 to 3600 cm⁻¹ region of a) 1 part in 200 propylene oxide, b) 1 part in 3000 2-fluoroethanol and c) 1:15:3000 2-fluoroethanol:propylene oxide:neon as well as the computed spectra for the six hydrogen bonded complexes 165

Figure 5.10. FTIR spectra in the 950-1150cm⁻¹ region of fluoroethanol:propylene oxide:neon complexes as well as the computed spectra for the fourteen hydrogen bonded complexes..... 166

Figure 5.11. Plot of reduced frequency vs gas-phase acidity for various matrix isolated hydrogen-bound dimers with water or dimethyl ether as the hydrogen bond donor 168

Figure 5.12. Plot of reduced frequencies vs the enthalpy of proton transfer for various matrix isolated hydrogen bonded complexes (filled circles) and gas-phase proton-bound dimers (open circles). The curves are to guide the eye and are discussed in the text 170

List of Tables	xvi
Table 3.1. The computed binding enthalpies and Gibbs energies (kJ mol^{-1}) between uracil and $[\text{M}(\text{Ura-H})]^+$ complexes (see Scheme 3.2) as determined by electronic structure calculations.....	108
Table 5.1. Observed and calculated (scaled) IR absorptions for the anti conformer of ethanol. All positions in cm^{-1}	151
Table 5.2. Observed and calculated (scaled) absorption for the d_6 isotopomer of ethanol. All positions in cm^{-1}	152
Table 5.3. Observed and calculated (scaled) absorption for propylene oxide. All positions in cm^{-1}	153
Table 5.4. New bands observed after deposition of 1:15:3000 ethanol:propylene oxide: Ne, their tentative assignments, and comparison with the calculated and scaled (equation) infrared spectra.....	157
Table 5.5. New bands observed after deposition of 1:15:3000 d_6 -ethanol: propylene oxide: Ne, their tentative assignments, and comparison with the calculated and scaled (equation) infrared spectra.....	161
Table 5.6. New bands observed upon codeposition of 2-fluoroethanol and propylene oxide in solid Neon at 4.2 K.....	164

List of Schemes	xvii
Scheme 1.1. Likely mechanism for the formation of the fragment ions in the collision induced dissociation (CID) and electron-induced dissociation (EID) spectra of protonated tryptophan. Figure modified from Anal. Bioanal. Chem. 2007, 389, 1429 with permission from Springer.....	11
Scheme 1.2. CID pathways of protonated uracil, determined from isotopic labeling patterns and by mass selection and activation of fragment ions, m/z 70 and 96. Figure modified from J. Am. Soc. Mass Spectrom. 1994, 5, 339 permission from Elsevier.....	13
Scheme 1.3. Initial reaction of protonated uracil following collisional activation	13
Scheme 1.4. Dissociation of protonated erythromycin A. Figure reproduced from J. Am. Soc. Mass Spectrom. 2002, 13, 630 with permission from Elsevier	19
Scheme 1.5. Possible structures of the uracil/HCl/Ar complexes	36
Scheme 3.1. The lowest energy possible structures for the $[M(\text{Ura})(\text{Ura-H})]^+$; M= Mg, Ca, Ba, Pb, Fe, Ni, Cu, Zn, and Cd	105
Scheme 3.2: The computed binding energy between neutral uracil and $[M(\text{Ura-H})]^+$ M= Mg, Ca, Ba, Pb, Fe, Ni, Cu, Zn, and Cd	106
Scheme 4.1. Numbering scheme for uracil.....	117
Scheme 5.1. Structure of the acetone-water hydrogen bonded complex.....	143
Scheme 5.2. Symmetric proton-bound dimers composed of a proton and two identical bases	173

List of Abbreviations..... xviii

Ade	Adenine
B	Magnetic field strength
CID	Collision induce dissociation
Cyt	Cytosine
<i>d</i>	Diameter of the ICR cell
DFT	Density functional theory
DNA	Deoxyribonucleic acid
ECD	Electron capture dissociation
ESI	Electrospray ionization
EtOH	Ethanol
ESR	Electron spin resonance
F_B	Lorentz force
f_c	Cyclotron frequency
FE	2-Fluoroethanol
FTICR	Fourier transform ion cyclotron resonance
FTIR	Fourier transform infrared
FWHM	Lorentzian function with a width
GA	Gas-phase acidity
Gua	Guanine
HF	Hartree-Fock
IR	Infrared

IRC	Intrinsic reaction coordination
IRMPD	Infrared multiple photon dissociation
IVR	Intramolecular vibrational redistribution
m	Mass of ions
PA	Proton acceptor
PCM	Polarizable continuum model
PD	Proton donor
PO	Propylene Oxide
q	Charge of ions
RF	Radio frequency
RNA	Ribonucleic acid
SE	Scaling equation
SF	Scaling factor
SORI	Sustained off resonance irradiation
Thy	Thymine
Ura	Uracil
m/z	Mass- to- charge ratio
Δv	The difference between the cyclotron and the RF excitation frequencies
$V_{p,p}$	Peak-to-peak excitation voltage
$\Delta_{PT}H$	Enthalpy of proton transfer
β	Geometrical factor of the ICR
ω_C	Angular velocity

Co-Autorship statment

I, Osama Ali, performed the experiments and calculations, analyzed the data, and wrote the first draft of the manuscript for chapters two, three, four, and five of this thesis, as well as helped edited supplementary drafts.

Chapter 1

Introduction

1.1 General Introduction

Molecular complexes are vital components of many biological processes and play essential roles in these processes. Certain ionic molecular complexes result from non-covalent interactions such as the interaction between metal ions and DNA nucleobases. Some of the biological processes impacted by these complexes include DNA and RNA synthesis and stabilization. Gas phase interactions provide chemists and biochemists with valuable information that aids in the understanding of the behavior of many biochemical and biological processes. Determining the gaseous ion structure of molecular complexes can provide a comprehensive understanding of the chemical properties of the molecules. Also, neutral molecular complexes are formed through hydrogen bonding like $C-H \cdots O$ or $O-H \cdots O$. These types are of particular interest because they play a very significant role in determining the shapes and conformations of molecules in the gas phase.

Weakly bound complexes can be observed in many chemical and biological studies; therefore, it is important to understand the nature of the intermolecular interactions involved in a wide range of molecular complexes. Studying these weak interactions in the gas phase is very important to investigate and identify the intermolecular interactions in the absence of solvents.

Ion-trapping mass spectrometry and matrix isolation are two main methods used for generating and isolating the complexes described in this dissertation. A large part of

this thesis describes studies of the interactions between uracil and divalent metal ions using mass spectrometry. This study is divided into three subparts. The first part is a study of the interaction between copper (II) ions with uracil using various fragmentation methods such as SORI/CID and IRMPD in combination with the theoretical calculations. The second part is a comparison of the interaction of uracil with different divalent metal ions using various fragmentation methods. The third part is elucidation of the structures of the complexes between uracil and Pb (II) ions, as well as singly and doubly water solvated complexes using infrared multiple photon dissociation (IRMPD) spectroscopy. In addition, we present an experimental observation of very weakly bound complexes in the form of the hydrogen-bonded complexes between propylene oxide and ethanol and between propylene oxide and 2-fluoroethanol in cryogenic neon-matrices. Density functional theory (DFT) calculations for the geometry optimizations and frequencies were also carried out.

1.2 Mass Spectrometric Techniques for Studying the Structures of Gaseous Ions

Mass spectrometry has played an important role in the life sciences during the past decade and has become particularly useful for identification and characterization of biological molecules. In general, analyte molecules are ionized and are separated in the gas phase, according to their mass-to-charge ratio (m/z). Mass spectrometry techniques differ in the types of ion sources, mass analyzers, and detectors. Fourier transform ion cyclotron resonance (FT-ICR) is one type of mass spectrometry and was used in many of the experiments described in this thesis. The following sections explain how the FTICR

specific to the present work operates. Techniques, such as those which initiate fragmentation processes which are available to us for the identification of the gas phase ions are also described.

1.2.1 Fourier Transform Ion Cyclotron Resonance (FT-ICR) Mass Spectrometry

Fourier transform ion cyclotron resonance is a type of mass spectrometry used to determine the ratio of mass-to-charge by measurement of the cyclotron frequency of the ions orbiting in a magnetic field.¹ This technique is considered very high resolution because it allows masses of ions to be resolved with great accuracy and provides accurate mass measurements.^{1,2} High resolution allows single compounds to be characterized from complex mixtures. The advantages of using high magnetic fields are improved mass resolution, signal-to-noise ratio, and mass accuracy. Ions are trapped in the radial dimension by a magnetic field (7.0T) and under high vacuum (10^{-10} torr).

The ions experience a magnetic Lorentz force (F_B) perpendicular to the magnetic field as illustrated in Figure 1.1. This Lorentz force is counterbalanced by the centrifugal force when entering the magnetic field. The cyclotron frequency, f_c , and the angular velocity, ω_c , depend on the mass to charge ratio (m/z) and are independent of the kinetic energy of the ions (velocity), as seen in the following equations (Eq.1.1 and Eq.1.2.)

$$f_c = \frac{\omega_c}{2\pi} \quad \text{Eq.1.1}$$

$$\omega_c = \frac{qB}{m} \quad \text{Eq.1.2}$$

These equations can be rearranged to obtain an expression for the m/z in terms of the magnetic field strength (B) and the cyclotron frequency, as seen in Eq.1.3.

$$\frac{m}{q} = \frac{B}{2\pi f_c} \quad \text{Eq.1.3}$$

where m is mass of ions and q is charge of ions.

The type of cells used for FT-ICR can have a number of different geometries however the most commonly used is the cylinder design. This cell consists of a pair of end cap trapping plates, pair of excitation plates and detection plates.

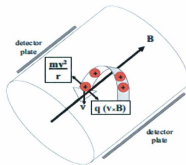


Figure 1.1: Cyclotron motion of positively charged ion moving in the magnetic field.

A small potential voltage is applied across two trapping plates at either the end of the cell, in the axial direction to keep ions trapped in this dimension. It is the magnetic field, B , which causes the ions to orbit the axis of the cell in a cyclic motion. The trapping voltage produces a radial force which is in an opposite direction of the Lorentz

force and this keeps the ions from drifting out of the B field. The use of a cell to trap the ions enhances the time to do experiments such as, kinetic studies, spectroscopy, and ion-molecule reactions.

To detect a signal from the ion cyclotron motion, the ions need to be excited to larger orbits. An application of a sinusoidal voltage to the excitation plates is used to excite the ions. The steps of the detection of ions are depicted in Figure 1.2. The ions are excited as a coherent ion packet and the cyclotron frequencies of these packets are m/z dependent. These ions absorb energy while maintaining a constant cyclotron frequency leading to an increase in their radii of cyclotron orbit. As the ions pass close to the plates they produce an image current on the two detector plates. When ions (positively charged) approach a detection plate, electrons are attracted to that plate. When the ions approach the opposite detection plate, electrons are attracted to that plate and drawn from the first plate. This results in an oscillation of current that allows the cyclotron frequency of the ions to be detected and measured. By applying a fast Fourier transform, the time domain signal is transformed to the frequency domain which is converted to mass spectrum through equation 1.2.

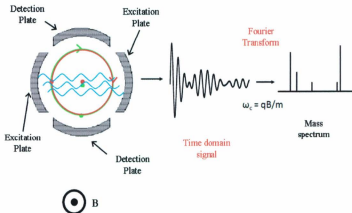


Figure 1.2: Steps in ion excitation and detection in a FTICR MS.

Electrospray ionization (ESI) was used to generate gaseous ions from a solution of dissolved ions. The generation of ions occurs in a number of steps. In this process a high voltage (kV) electric field is applied to a steel capillary containing the sample solution at atmospheric pressure. This voltage results in the accumulation of charges at the capillary tip that eventually break off and disperse into space forming a highly charged droplet. Evaporation of the solvent causes the droplet to shrink. As the droplet becomes smaller the electrostatic repulsion of the charges increases and fission occurs. Therefore, the process of fission leads to the formation of charged positive ions in the gas phase through evaporation of the solvent. The evaporation process and fission produces small droplets until it contains only one ion in each droplet,³ as seen in Figure 1.3.

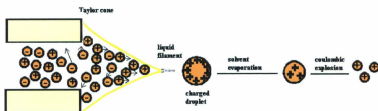


Figure 1.3: Electrospray ionization process.

The ESI process occurs at atmospheric pressure, while the ICR cell is at ultra high vacuum. Thus, differential pumping is required to drop from atmospheric pressure in the source to 10^{-10} mbar in the ICR cell,⁴ as seen in Figure 1.4. A gate valve separates the region containing the high vacuum from the rest of the instrument. After producing the ions, they are then injected into the ICR cell.

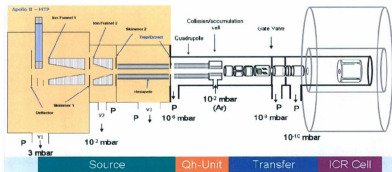


Figure 1.4: Schematic of 7.0 T FT-ICR mass spectrometer. Figure reproduced from J. Am. Soc. Mass Spectrom. 2009, 20, 411 with permission from Elsevier.

1.2.2 Fragmentation Processes in the FTICR

There are a number of activation methods that can be used to fragment precursor ions producing MS/MS spectra. Through fragmentation it is possible to obtain structural information by investigating the ionic fragments. One of the most commonly used methods for ion activation is collision induced dissociation (CID). Ion-traps allow easy implementation of other methods such as infrared multiple photon dissociation (IRMPD) and electron capture dissociation (ECD), as well.

1.2.2.1 Collision-Induced Dissociation (CID) method

Collision-induced dissociation (CID) is a technique that is used to fragment molecular ions in the gas phase in order to obtain ionic fragments. In general, this technique is used to achieve structural information of the analyte ion by looking at the fragments ion.⁵⁻⁷

The principle of CID is that the molecular ions are accelerated using an electrical potential to reach high kinetic energies and then collide with neutral gas molecules (collision gas). During the collision, some of the kinetic energy of the ion is converted to internal energy (vibrational/rotational). The excited precursor ion will then fragment into smaller ions, which can be observed using the mass spectrometer. The CID process depends on the conditions of the experiment such as the nature of the collision gas, the kinetic energy, the parent ion, and the number of collisions. Depending on the type of mass spectrometer in use, there are two main collision regimes. Low energy CID is used with a collision energy below 100 eV, while in high energy CID kinetic energies of several thousands of electronvolts are commonly used for fragmentation. High-energy

CID is typically performed in sector mass spectrometers, where keV accelerations are required for mass and energy analysis. Since in FTICR, and most other mass spectrometers, CID is done at low energy that is discussed in more detail here.

1.2.2.1.1 CID External to ICR cell

In low energy CID, in the FTICR instrument used in this work, a precursor ion is first isolated in a quadrupole mass filter then accelerated into a region of high pressure in the storage/collision hexapole, which has 10^{-2} mbar Ar (see Figure 1.4). Ions leaving the quadrupole are accelerated by less than 100 eV into the collision gas. With these low energy collisions, the excitation energy imparted to the ion is typically consistent with vibrational excitation.⁸ The law of conservation of momentum states that kinetic energy of a fast particle that collides with a stationary target is not entirely converted into internal energy, therefore this implies that only a fraction of the translational energy is converted into internal energy. Through multiple collisions, the ion gains enough energy for bond cleavage.

$$E_{com} = E_{lab} \frac{M_t}{M_t + M_i} \quad \text{Eq.1.4}$$

where M_i is the ion mass, M_t is the target mass (i.e the collision gas), E_{lab} is the ion kinetic energy in the laboratory frame, and E_{com} is the maximum energy fraction converted into internal energy for the fragmentation. For example, when using Ar collision gas, collision of a singly-charged ion with a mass of 300 Da, the maximum energy that can be converted to internal energy of the ion at 10 eV (laboratory frame) is 1.2 eV.

The CID technique has been used in many fields for determination and characterization of the structures of biological molecules. For example, singly protonated aromatic amino acids have been examined using FT-ICR MS defined previously.⁹ Low energy collision induced dissociation (CID) for protonated tryptophan was compared with the electron-induced dissociation (EID) or simply electron ionization. In the CID spectrum of protonated tryptophan, the primary fragmentation pathway is the loss of NH_3 and then a very minor loss of $(\text{H}_2\text{O} + \text{CO})$ as in Figure 1.5a. In contrast the EID spectrum shows that the dominate fragmentation is loss of the side chain benzyl cations at m/z 130 as in Figure 1.5b. The mechanism for loosing NH_3 has been proposed to occur through formation of a spirocyclopropane ion by attacking the C-3 of the indole aromatic side chain, while the formation of the tryptophan radical via hydrogen atom loss has been shown to fragment to give two stable fragments, as seen in Scheme 1.1. These types of experiments are beneficial and help to gain insight into the structure of simple peptide molecules.

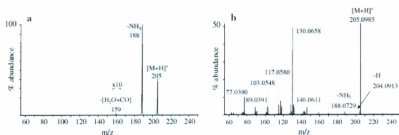
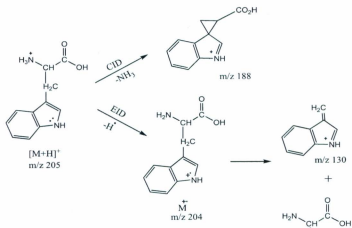


Figure 1.5: Fragmentation of $[\text{M}+\text{H}]^+$ of tryptophan under conditions a) collision induced dissociation (CID) and (b) electron-induced dissociation (EID) 23 eV. Figure reproduced from *Anal. Bioanal. Chem.* 2007, 389, 1429 with permission from Springer.



Scheme 1.1: Likely mechanism for the formation of the fragment ions in the collision induced dissociation (CID) and electron-induced dissociation (EID) spectra of protonated tryptophan. Figure modified from *Anal. Bioanal. Chem.* 2007, 389, 1429 with permission from Springer.

Nelson and McCloskey¹⁰ have studied the structure of protonated uracil using collision induced dissociation. The protonation of uracil may occur at either the O2 or O4 positions. However, uracil is predominantly protonated at the O4 position which corresponds to the keto form tautomer.¹¹⁻¹³ The CID spectrum of protonated uracil (m/z 113) is shown in Figure 1.6. The dissociation of protonated uracil formed three main dissociation product ions (m/z 96, 95, 70). The first pathway is the loss of NH_3 (m/z 96) followed by elimination of a molecule of CO (m/z 68). The second pathway is the loss of H_2O (m/z 95) followed by elimination of CO (m/z 67) or HNCO (m/z 52). The spectrum shows that the major dissociation pathway is loss of HNCO (m/z 70) with further losses

of NH_3 , CO , HCN , $\text{C}_2\text{H}_2\text{O}$, and C_2HNO to produce ions at m/z 53, 42, 43, 28 and 15, respectively, as seen in Scheme 1.2.

The loss of HNCO is the major decomposition pathway which is nonexistent in the EI mass spectrum of uracil.¹⁴ By using isotopically labeled uracil, the major elimination pathway was shown to involve loss of C_2 and N_3 through a retro-Diels-Alder mechanism, as in Scheme 1.3.

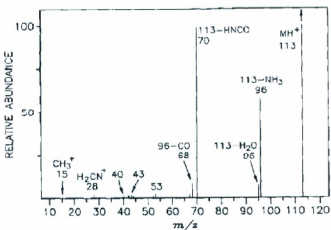
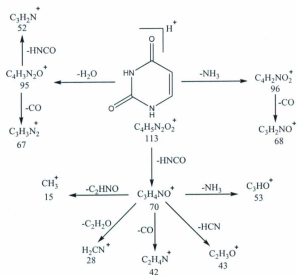
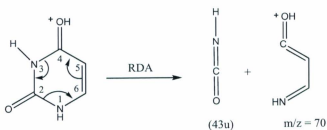


Figure 1.6: CID spectrum of protonated uracil. Figure reproduced from *J. Am. Soc. Mass Spectrom.* 1994, 5, 339 with permission from Elsevier.



Scheme 1.2: CID pathways of protonated uracil, determined from isotopic labeling patterns and by mass selection and activation of fragment ions, m/z 70 and 96. Figure modified from *J. Am. Soc. Mass Spectrom.* 1994, 5, 339 with permission from Elsevier.



Scheme 1.3: Initial reaction of protonated uracil following collisional activation.

1.2.2.1.2 SORI/CID

Ion activation and fragmentation via off-resonance irradiation (SORI) collision induced dissociation is commonly used in FTICR MS and is essentially a special name given to CID performed in the FT-ICR cell. In this technique, the collision gas is introduced into the cell through a pulse valve at a pressure of about 10^{-8} mbar. The fragmentation in the ICR cell is affected by applying a short radio frequency (RF) pulse to kinetically excite the ion. The ions are accelerated and their translational energy is converted to internal energy by collisions with the neutral collision gas resulting in fragmentation. The mean laboratory frame collision energy in SORI/CID is calculated according to the method described in the literature,^{15,16} as seen in Eq. 1.5. After obtaining the laboratory frame collision energy the maximum kinetic energy can be determined and used to describe the collision process, as seen in Eq. 1.4. In this equation, the heavier of the collision gases are preferred, which allows multiple collisions (tens to hundreds) to occur.

$$E_{lab} = \frac{\beta^2 q^2 V_{p-p}^2}{32\pi^2 m d^2 \Delta\nu^2} \quad \text{Eq.1.5.}$$

where β is the geometrical factor of the ICR cell, q and m are the charge and the mass of the ion respectively, V_{p-p} is the peak-to-peak excitation voltage, d is the diameter of the ICR cell, and $\Delta\nu$ is the difference between the cyclotron and the RF excitation frequencies.

1.2.2.2 Infrared Multiple Photon Dissociation (IRMPD)

Infrared multiple photon dissociation can be a very useful method to determine ion structures and it is possible to gain a vast amount of structural information with this technique. In particular, it can be used to study the structures of proteins and other biological molecules. In this method, a laser with high intensity is used to obtain structural information of gaseous ions. This method depends on the absorption of several IR photons. The gaseous precursor ions are trapped inside the ICR cell and directly irradiated with the laser through a window. The trapped ions are heated through absorption of one or more photons. The absorption of subsequent photons increases the internal energy of the precursor ions to a point sufficient to cause the dissociation of the ion. Consequently, the number of photons depends on the wavelength of the incident radiation.¹⁷ In addition to the CID method, this technique was used for fragmentation of the precursor ions in the research described in this thesis.

The mechanism of IRMPD has been explored extensively in the literature.¹⁸⁻²¹ An integral factor in the absorption of photons by an ion is resonance, particularly resonance between a vibrational mode and the laser source in the $v=0$ to the $v=1$ state. However, IRMPD is not a single photon process, therefore it is important to illustrate three vital changes in energy levels that result in complete energy randomization and consequently the dissociation of ions. As seen in Figure 1.7, these levels can be categorized into a lower energy level, middle level also known as quasicontinuum and an upper level where dissociation occurs. The lower level requires resonance between the laser and the molecule in order for absorption to occur. The energy absorbed gets transferred to other

modes in the ion in a process called intramolecular vibrational energy redistribution (IVR). As the molecule absorbs more photons and the internal energy increases the density of states increases such that the middle energy level is reached. This middle level is called quasicontinuum and at this level the laser is absorbed through "accidental resonances" due to the anharmonicity of the vibrational mode. The process of absorption will continue until the internal energy inside a molecule reaches the necessary energy requirement to surpass the dissociation threshold and dissociation occurs. Note that for dissociation to be observed on the time scale of the experiment, the internal energy must be in excess of the dissociation energy.

Similar to CID, IRMPD is a valuable method that can be used to fragment ions and thus provide a comprehensive understanding of an ion's structure. Although both methods are useful when attempting to obtain structural information on a particular ion, CID does have some limitations. CID requires a collision gas to excite the ions. This results in differing degrees of fragmentations due to the fact that all of the translational energy is not converted entirely into internal energy on collision. On the other hand, IRMPD uses a CO₂ laser to irradiate the gaseous ions. This method has some advantages over other ion activation methods such as it is faster and more selective.

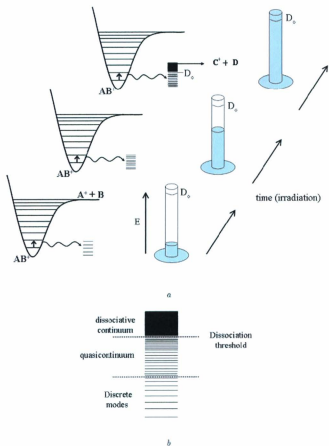


Figure 1.7: (a) Schematic representation of IRMPD mechanism and (b) vibrational state density in a molecular ion.

Hergenrother *et al.*²² compared the effectiveness between using IRMPD and CID in characterizing erythromycin A, (m/z 734), analogs in a quadruple ion trap. Both IRMPD and CID show that the most prevalent fragment pathway includes dehydration

and loss of cladinose sugar (m/z 576), as seen in Scheme 1.4. They found that the IRMPD spectra identified a dominant fragment ion, which was the desosamine ion. However, when using CID, this ion was not observed because the mass is too low to be trapped efficiently under the conditions used, as seen in Figure 1.8. IRMPD allows for selective dissociation based upon the wavelength of the incident radiation. In this method only ions that absorb at the wavelength can be dissociated.

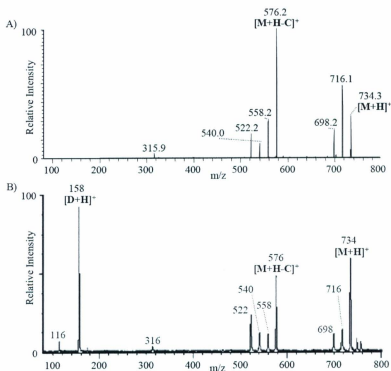
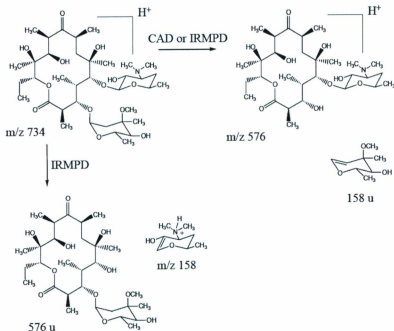


Figure 1.8: (a) CID and (b) IRMPD of protonated erythromycin A. Figure reproduced from *J. Am. Soc. Mass Spectrom.* 2002, 13, 630 with permission from Elsevier.



Scheme 1.4: Dissociation of protonated erythromycin A. Figure reproduced from *J. Am. Soc. Mass Spectrom.* 2002, 13, 630 with permission from Elsevier.

1.2.3 Infrared Multiple Photon Dissociation (IRMPD) Spectroscopy

The ability to trap ions inside the ICR cell for extended periods permits the use of different techniques for studying the ions. One of these techniques is infrared multiphoton dissociation (IRMPD) spectroscopy. A CO_2 laser which is high powered and is efficient in affecting IRMPD is not broadly tunable, so is not useful for such a technique. Tunable sources of infrared radiation have been recently developed to increase the ability of recording the infrared spectra of gaseous ions over a usable range.

Free electron lasers (FELs)^{23,24} and the optical parametric oscillator/amplifier (OPO/A)²⁵ are used as tunable sources for infrared radiation. The FELIX (Free-Electron Laser for Infrared eXperiments) in the Netherlands and CLIO (Centre Laser Infrared d'Orsay) in France are two facilities capable of performing IRMPD spectroscopy. Thus, they can be used to measure IR spectra over a broad range of the mid-IR. Despite the use of a different laser, the mechanism of IRMPD spectroscopy is the same as for the IRMPD fragment mode explained in the previous section. IRMPD is an effective method for obtaining structural insight into ion structures. This technique allows gas phase molecule ions to be studied over a wide spectral range.

1.3 The Matrix Isolation Technique for Studying Weakly Bound Intermolecular Complexes

1.3.1 Principle of the Matrix Isolation Technique

Matrix isolation spectroscopy is an important tool in experimental chemistry and physics. It is a powerful method for gaining information and determining mechanistic data for transient species. Matrix isolation is used for carrying out leisurely spectroscopic studies at low temperature by trapping a transient species in a solidified rare-gas matrix. Solidified rare-gas matrices have many advantages such as chemical inertness and good transparency in the infrared (IR) region.

The matrix isolation technique was invented by George Pimentel (considered the father of matrix isolation). In 1954, the concept of matrix isolation was first published from Pimentel's group using a xenon matrix at 66 K.²⁶ In this technique, individual molecules or atoms are trapped and isolated from one another by the rare gas matrix at

low temperature. The matrix isolation technique was developed to study highly reactive molecules such as free radicals and other thermodynamically unstable species. It also allows for the study of interactions in weakly bound species such as hydrogen-bonded and van der Waal complexes that may be transient at room temperature.

The main components in the matrix isolation technique are the guest species and the host. In this technique, the trapped species cannot undergo any bimolecular reactions with any species except perhaps with the host material. Figure 1.9 is a cartoon structure representing a matrix when some analyte is trapped in a rigid matrix.

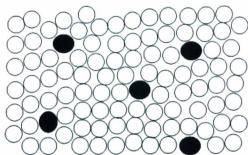


Figure 1.9: Diagram representing, a guest species (in black circle) isolated in solid host matrix (in open circle).

In order to prepare a solid matrix, the species is deposited with a large amount of host gas onto a cold substrate, which is cooled to a suitable temperature of 4.2 K (neon gas). All the experiments are carried out under high vacuum to prevent any contamination from unwanted gases that may freeze on the cold window. In general, rare gases are used as common host materials for matrix isolation; however, nitrogen, oxygen,

methane, hydrogen, and water have also been used as host materials.

The main method of studying matrix isolation is by spectroscopic means. These experiments can also help to determine the structures of reactive species,²⁷ and characterize molecular complexes which have weak interactions between species.²⁸⁻³⁰

Since the main process in matrix isolation involves depositing the matrix gas and sample on a cold window, the species to be trapped in matrix must be somewhat volatile or it must be able to be volatilized. There are two ways to mix the guest species with the host, which depends on the volatility of the guest. The vapour pressure must be easily measured in order for the guest and host gas to be capable of mixing and producing a gas mixture that is then deposited as a solid matrix. This mixing of a guest and a host is known as proportions; on the other hand, the ratio of the host to guest is known as the matrix ratio. If the guest species has low volatility, it evaporates from one side of the vacuum shroud in the cold cell. Simultaneously, as the guest species is being evaporated the host gas is also being deposited into the cold cell.

1.3.2 The Matrix Isolation Technique

The matrix isolation technique has been thoroughly discussed in the literature³¹⁻³⁶ and a brief discussion of this experimental technique is outlined in this section, along with some examples relevant to the study described in Chapter 5 of this thesis.

1.3.2.1 Sample Preparation

To prepare the matrix at low temperature, it is essential to mix the host gas and the guest gas in the vapour phase. The sample is prepared in a stainless steel pipeline that uses high vacuum gauges and valves, which is separated from the matrix isolation

apparatus, as seen in Figure 1.10.

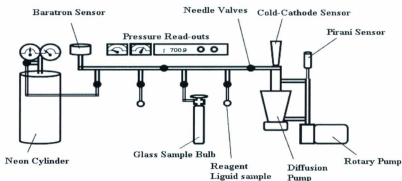


Figure 1.10: Schematic of gas-handling apparatus used for preparation of gas samples for matrix isolation experiments.

A rotary pump is used to achieve a pressure of 10^{-3} torr on the line. As a pressure of 10^{-3} torr is reached a diffusion pump is opened and the pressure is reduced to 10^{-8} torr. During this process two different vacuum gauges are used to read the appropriate pressure. The first one is the Pirani sensor which is used to monitor the pressure down to 10^{-3} torr. The second gauge is a cold cathode gauge which monitors the pressure to between 10^{-4} - 10^{-8} torr. Also, a series of Baratron sensors is used to measure gas pressure up to 1000 torr when mixing matrix and sample gases. Needle valves are used to control gas flowing in and out of the line. A neon cylinder is attached as the reagent sample to the lines by using a stainless steel compression fitting.

In every experiment, the reservoir was evacuated for a few hours and the pressure

on it remained constant between 10^{-6} - 10^{-7} Torr prior to use. Liquid samples were degassed through freeze-pump-thaw cycles. Accordingly, the partial pressure of the host gas (neon) will be much larger than the partial pressure of the sample. As a result, the host gas is sealed after the sample. The sample gas is pumped from the reagent bulb to the gas reservoir until it reaches the appropriate pressure which is read by the Baratron sensor. After that the sample in the reservoir is diluted with the host gas (neon) to the desired concentration.

The mixture ratio between the host gas and sample be varied, so that the molecules of the sample gas are fully separated from one another. In all our experiments, the gaseous solutions were mixed in ratios of approximately 1/1-15/3000 between ethanol/propylene oxide/neon gases respectively. For example for a preparation of a 900 Torr sample with a concentration of 1/15/3000 of ethanol and propylene oxide to neon gas, 0.3 Torr of ethanol and 4.5 Torr of propylene oxide is prepared then diluted by 900 Torr of neon.

1.3.3.2 Closed-Cycle Refrigerator

The development of closed cycle helium refrigerators provides an approach to utilize liquified gases as a coolant for all matrix experiments. The purpose of the refrigeration cycle is to use helium gas from a helium compressor to form low temperatures at the sample holder. When the system is evacuated to an appropriate level, the closed helium refrigeration system is turned on to start cooling the system. In this system, the expander head is supplied with the helium to expand and to cool the area down to 4.2 K. Using a second hose, the helium gas returns to the compressor to close

the cycle, so in this process no helium is consumed. As a result, continued cycles of pumping helium allow the spectroscopic window to cool down to 4.2 K. At this temperature the pressure is reduced further from 10^{-8} to around 10^{-9} torr. In our lab, a cryogenic system is used, which allows the temperature to reach 4.2 K.

This system (refrigerator) needs only an electrical supply and cooling water to remove heat during the compression cycle. Some of the advantages for this refrigerator include its ability to work for thousands of hours with little maintenance and the time needed to cool the spectroscopic window of matrix isolation to a low temperature of 4.2 K takes less than an hour and a half.

1.3.2.3 Sample Deposition

Pure gases or mixture of gases can be deposited as low temperature matrices by using the slow spray-on method. This method and the process of the gas mixture deposition are described in Chapter 5.

1.3.3 Spectroscopic Techniques of Matrix Isolated Species

Several spectroscopic techniques, such as infrared (IR), ESR, Raman, Ultraviolet and visible spectroscopy (UV/Vis), can be used to characterize the appropriate species in matrix isolation. Although a variety of techniques exist, infrared spectroscopy has been used for the identification of trapped species for the purpose of this thesis.

1.3.3.1 FTIR

FTIR is one of the many spectroscopic techniques which can be used with low temperature matrices. Infrared spectroscopy can be used to identify compounds and investigate the structural components of the sample being used. When absorption occurs in a molecule, vibrational modes become excited. These vibrational modes in a molecule are activated through infrared spectroscopy, and only the vibrational modes which result in a change in dipole moment of the molecule will be observed in the spectrum.³⁷ These modes are classified as stretching of the bonds or non-stretching modes such as bending, torsion, wagging, rocking, and deformations. The vibrational modes produced are dependent on the number of atoms in the molecules; there are $3N-6$ vibrational modes for a non linear polyatomic species.

The positions of vibrational bands for the stretching sites of molecules are determined depending on the oscillator between two adjacent nuclei while the motions of the other nuclei are ignored as Eq. 1.6.³⁸ These vibrational bands depend on the reduced mass, μ , and the force constant, k , which is a measure of the strength of the bond formed:

$$\bar{\nu} = \frac{1}{2\pi c} \sqrt{\frac{k}{\mu}} \quad \text{Eq.1.6}$$

The positions of IR absorptions can be used as a tool for identifying a given molecule and for determining what functional groups are present in the molecule. In order to assign particular molecules to their appropriate modes isotopic substitution can be used. For example, the ratio between the vibrational wavenumber for an X-H stretch

to a X-D stretch depends on the reduced masses, μ , of the H and D with any other atom X, as seen in the following equation.

$$\frac{\bar{\nu}_H}{\bar{\nu}_D} = \frac{\frac{1}{2\pi c} \sqrt{\frac{k}{\mu_{H-X}}}}{\frac{1}{2\pi c} \sqrt{\frac{k}{\mu_{D-X}}}} \quad \text{Eq.1.7}$$

Equation 1.7 can be reduced to

$$\frac{\bar{\nu}_H}{\bar{\nu}_D} = \frac{\sqrt{\mu_{D-X}}}{\sqrt{\mu_{H-X}}} = \frac{\sqrt{2}}{\sqrt{1}} = 1.4 \quad \text{Eq.1.8}$$

Consequently, for many stretching motions the ratio between the vibrational wavenumber for hydrogen over deuterium is approximately 1.4.

This approach is beneficial for determining and characterizing the type of complex which is produced by interactions in matrix isolation. The ratio of an H-X over a D-X is around 1.4 because the deuterium mass is twice that of the hydrogen. However, the ratio for a bending motion may be as low as 1.10. A 1.4 ratio indicates that a 1:1 binary complex is formed. For example, Kim and Han³⁹ have studied the interaction between dimethyl ether (DME) and methanol in a solid argon matrix at 9 K. When the samples of DME and methanol were deposited, the OH stretching peak appeared at 3534.1 cm^{-1} . In addition, when samples of DME and methanol-d4 were deposited a new peak was seen at 2610.9 cm^{-1} on the cold window which corresponds to the O-D stretching. In this case, the isotopic stretching frequency ratio $\nu(\text{OH})/\nu(\text{OD})$ is computed to be 1.3516 which suggests a 1:1 binary complex.

Molecular aggregations can form when the samples are used in high

concentrations. In this case, unwanted complexes may form which make it difficult to characterize the desired spectrum. At high dilution, the trapped molecules should be isolated properly and aggregation via guest-guest interactions minimized.

Using matrix isolation infrared spectroscopy has many advantages over gas phase studies. In the gas phase, the molecules can rotate which causes a broadening of the vibrational bands in the IR spectrum. The broadening in the gas phase infrared spectrum can make it difficult to identify the product by making it hard to decipher some of the information contained within the spectrum. Comparatively in matrix isolation, the host material acts as a cage and clamp which eliminates the ability of the guest to rotate. Figure 1.11, shows a comparison between the gas phase and matrix IR spectra for the symmetric stretching vibration for sulfur dioxide, SO_2 , molecule where the small bandwidth is very clear.⁴⁰ The matrix isolation absorption is a narrow band at 1151 cm^{-1} with a small sub-band at 1146 cm^{-1} instead of a broad band compared to those seen in the gas phase.

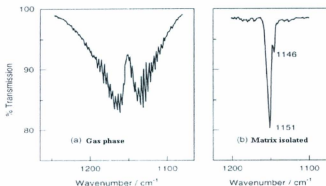


Figure 1.11: IR spectra of the SO₂ (symmetric stretch) near 1150 cm⁻¹ (a) in the gas phase at room temperature, and (b) matrix isolated in N₂ at 12 K (N₂: SO₂ = 100:1). Dunkin, I. R. *Matrix isolation techniques: a practical approach*; Oxford University; New York, 1998.

Chemical effects caused by the matrix itself may also cause changes in the IR spectrum and the noble gases and N₂ gas are used to limit this effect. Neon matrices have become the most widely used choice for matrix experiments as they are expected to show the weakest host-guest interaction due to its small polarizability.⁴⁰

There are a number of factors which can affect vibrational spectroscopy and these factors can influence the spectrum by causing existing bands to move to a new location. Such effects on spectra can be seen when comparing the effect of the matrix on the isolated species with a gas-phase spectrum.

Comparison of a gas-phase spectrum with one from an isolated matrix species shows shifts in the band centre which depends on guest-host interactions. For example, Figure 1.12 depicts an infrared spectrum in the region of the CO stretching of methanol

isolated in N_2 , Ar, Kr and Xe matrices.⁴¹ A blue shift is observed in N_2 , in comparison with the gas-phase band which is indicated by the vertical line, and this suggests that a repulsive interaction between the matrix cage and oscillator is in effect. An increase in the magnitude of the red shifts, from Ar to Kr and Xe, is noted, and as the polarization of the host increases the shift should become more prominent as seen in Figure 1.12.

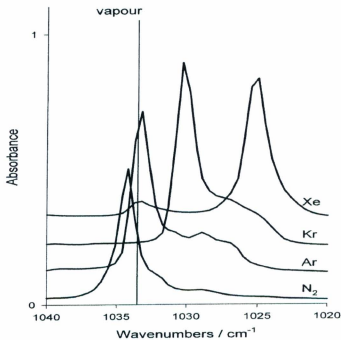


Figure 1.12: Portion of the FT-infrared spectrum of methanol isolated in N_2 , Ar, Kr and Xe showing the effect of different environments on the CO stretching fundamental. The vertical line shows the position of the vapour-phase band centre. Figure reproduced from, Travis D. Fridgen, PhD thesis; Queen's University; Canada, 1999, with permission from the author.

1.3.3.2 Annealing Method

Annealing is a method used in matrix isolation to see if any changes occur in the spectrum. Annealing is performed by warming the matrix to a suitable point but not to evaporate the matrix, which enables the guest species to diffuse throughout the matrix. This method is achieved after the matrix has formed and a spectrum has been taken. Throughout the process, a temperature controller is monitored to control the temperature of the system that is located near the cold window. The maximum annealing temperatures depends on the type of the gas (host) that is used. In our experiments, the matrix was annealed at 10 and 14 K each for an hour and IR spectra recorded after each annealing.

The typical temperatures for the matrices are; 10-15 K for neon, 35 K for argon, 50 K for krypton, and 65 K for xenon. The low temperature of matrix isolation prevents the species from rotating. So, annealing the matrix allows the guest species to diffuse and removes the effect of the rigid cage that occurred by the host gas. After annealing the molecules are able to obtain their thermodynamically stable structures in the matrix. Thus, annealing can be used to identify bands due to the splitting at the site of the matrix. In particular, small atoms and molecules such as hydrogen, sulfur dioxide, may still rotate within the matrix cage.^{42,43}

1.3.3.3 Molecular Complexes in Inert Gas Matrices

Many studies have been published examining weak molecular complexes in the gas phase⁴⁴ and in matrices.⁴⁵ Matrix isolation coupled with infrared spectroscopy provides useful information that can be utilized when studying weak complexes that

occur between reactive molecules.

The vibrational spectra of weakly bound binary complexes provide insight into the changes in the structure of molecules and/or complexes. In order to obtain meaningful results and explain the assignments of the infrared spectrum of a binary complex observed in matrix isolation experiments, an isotopmer of the target is required. In addition, theoretical calculations are beneficial when attempting to explain the spectrum. Accurate predictions for the calculated frequencies can be used to make accurate comparisons with the experimental frequencies.

Intermolecular interactions are an important factor in many molecular and biological processes in chemistry and biology.⁴⁶ These interactions can be studied experimentally by using matrix isolation techniques.^{26,47} In fact a weak molecular interaction like C-H- π in complexes plays a significant role in determining the shape of conformations of molecules in the gas phase.

One very important type of molecular complex is the hydrogen bonded complex. Hydrogen bonding is one type of strong intermolecular forces. It is a prominent interaction in many of life's processes and a vital component in the fields of chemistry, physics, and biology.

The structure of a H-bond is of the type X-H \cdots Y, where X and Y are electronegative elements. These elements are usually oxygen, nitrogen, and halogens but Y, which contains one or two non-bonding electron pairs, can be a region of excess electron density, such as a π -system. In matrix isolation, weak complexes between molecules have shown that in the majority of cases one molecule acts as proton donor

(PD) while the other molecule acts as proton acceptor (PA). For example, matrix studies have revealed that alcohols act as proton donors and various bases such as acetone,⁴⁸ acetonitrile,⁴⁹ dimethyl ether,⁵⁰ and water⁵¹ act as proton acceptors.

Parnis *et al.*⁵² have studied the hydrogen-bonded acetone-water complex by matrix isolation experiments as well as theoretical calculations. Spectra of the acetone-water complex in argon matrices were recorded at 12 K in regions 3800-3450 cm^{-1} and 1640-1560 cm^{-1} as seen in Figure 1.13. Upon complexation, red shifts were observed for the O-H stretching modes of water and for the C=O stretching mode of acetone. These shifts indicate that a 1:1 complex is formed, in which water is hydrogen-bonded to the carbonyl oxygen of acetone.

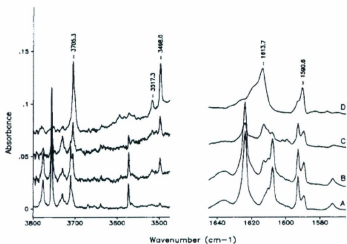


Figure 1.13: FT-infrared spectra of argon matrices containing water(1:10³ H₂O/Ar) and 1:10³ (A), 1:3x10² (B), 1:10² (C), 1:50 (D) acetone/Ar, in the region 3800-3450 and 1645-1560 cm^{-1} . Figure reproduced from *J. Phys. Chem.* 1993, 97, 4320 with permission from American Chemical Society.

Nelander⁵³ has studied the infrared spectra of the formaldehyde-water complex in inert matrices. He found a blue shift in the water bending mode and a red shift in the carbonyl and OH stretching modes. The shifts were similar to those observed for the acetone-water complex.⁵² These red shifts of the OH stretching, compared to the substantial blue shifts of the OH bending modes, indicate that water acts as a proton donor in forming these complexes. Johnson and Andrew⁵⁴ observed red-shifts for the fundamental modes for 1:1 complexes between HF or DF, and acetone or formaldehyde and these shifts are similar to the modes observed for the acetone-water complex.⁵²

The intermolecular hydrogen bond that exists between nucleic acid bases is very important in molecular biology. Therefore, the vibrational spectroscopy of the nucleobases has been studied in low-temperature matrices.⁵⁵⁻⁶⁰ In particular, the FTIR spectra of uracil, thymine, and of their derivatives have been performed in low temperature inert matrices.^{61,62} The interactions between uracil and models of proton donor molecules and their ability to form hydrogen bond complexes have been studied. In fact, the interaction of uracil and hydrogen chloride in argon matrices demonstrates that hydrogen bonds are formed. Uracil has many sites to form a hydrogen bond with proton donor molecules, the basic C=O site and the acidic N-H sites are involved in H-bonding with other molecules.

Maes *et al.*⁵⁸ have studied a series of interactions between uracil derivatives and their hydrogen-bonded complexes with proton donor molecules such as H₂O and HCl in argon matrices. Figure 1.14 shows the FTIR spectra of uracil with HCl/Ar in matrices. When samples of uracil/HCl/Ar gas were deposited at 12 K, new features were found

that were not present in either of the uracil or hydrogen chloride molecules. The presence of these new bands provides characteristic evidence that uracil/HCl complexes have been found. A new band is observed at 1685 cm^{-1} which refers to red shift of $\nu(\text{C4=O})$, and the $\nu(\text{C2=O})$ mode appears at 1775 cm^{-1} . Also, as in Figure 1.14(c), new absorptions are noted at 814 , 764 and $676\text{--}673\text{ cm}^{-1}$ which are attributed to $\gamma(\text{C4=O})$, $\gamma(\text{C2=O})$, and $\gamma(\text{N3-H})$, respectively. An additional band is observed at 3375 cm^{-1} due to shift of $\nu(\text{N3-H})$. These bands indicate that the uracil interacts with HCl at two different sites, the basic (C4=O) site to form $\text{C4=O}\cdots\text{HCl}$ H-bond, and N-H group to allow $\text{N-H}\cdots\text{Cl-H}$ H-bonds to be formed in the argon matrices as seen in Scheme 1.5.

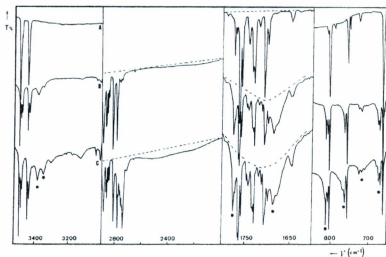
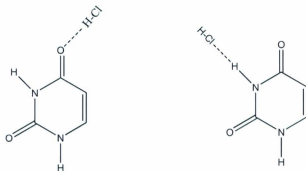


Figure 1.14: FTIR spectrum for uracil/Ar (A) and uracil/HCl/Ar (B,C) at 12 K. (B, HCl/Ar = 1/200; C annealed of B). Figure reproduced from *J. Mol. Struct.* 1994, 318, 37 with permission from Elsevier.



Scheme 1.5: Possible structures of the uracil/HCl/Ar complexes.

1.4 Pyrimidic Nucleobases

1.4.1 Nucleic Acid Bases

Nucleobase molecules are one of the important macromolecules found in cells and obviously play an essential role in cell function and reproduction. The importance of these nucleobases has become more apparent since the discovery of the double helix structure (DNA) by Watson and Crick.⁶³ By using X-ray diffraction, they discovered that the DNA molecule is constructed of two strands to form a double helix. The two strands have a different order of nucleobases and are bound to each other by hydrogen bonding.

The nucleobases in DNA and RNA refer to two of the heterocyclic compounds, purine and pyrimidine.⁶⁴⁻⁶⁶ The pyrimidine nucleobase is a ring containing nitrogen atoms and it is a significant compound in biological processes. The monocyclic pyrimidines; such as uracil (Ura), thymine (Thy), and cytosine (Cyt), consist of six-membered rings which contains nitrogen and carbon atoms. On the other hand, the

purines adenine (Ade) and guanine (Gua) consist of two bicyclic rings, as seen in Figure 1.15. These nucleobases contain oxygen, hydrogen, and at least one N-H site. Thus, these atoms may be attached to other molecules through hydrogen bonds. Consequently, the nucleobases may exist in different tautomeric forms which provide it with other possible functionalities.

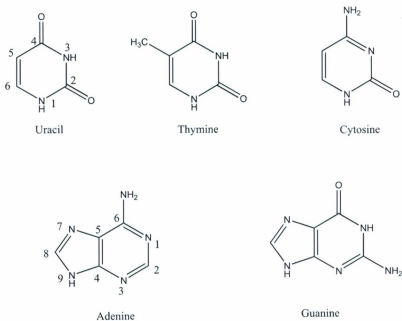


Figure 1.15: Structures of the common pyrimidine and purine bases of nucleic acids.

1.4.2 Hydrogen Bonding in Base-Pairing

Hydrogen bonding plays an important role in a variety of scientific fields and occurs in inorganic molecules and organic molecules as seen in DNA. This type of bond is responsible for forming the base-pair interactions in DNA which play a large part in the transfer of genetic information. Basically, there are different functional groups in the nucleobase which form the hydrogen bonds. The nitrogen bases N-H and amino group – NH₂ are hydrogen bond donors. On the other hand, the nitrogen atom on the ring and the carbonyl group are hydrogen bond acceptors.

Due to the hydrogen bonding of nucleic acid bases in DNA, one strand binds with the other strand to form a double helix which is known as Watson-Crick pairing. In this pairing, pyrimidines attach to the purines through hydrogen bonds. Specifically, cytosine nucleobase bonds to guanine through three hydrogen bonds (C-G), while adenine bonds to thymine via two hydrogen bonds (T-A), Figure 1.16.

The double helix in DNA is stabilized via hydrogen bonds between these pairs and through the hydrophobic interactions between bases. Many theoretical studies have focused on studying the hydrogen-bonding of the base pairs in DNA.⁶⁷⁻⁷⁰ In particular, studies of the imino-enol tautomers of bases concluded that these tautomers may form a spontaneous mutation.

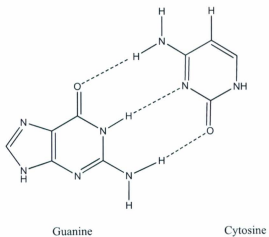
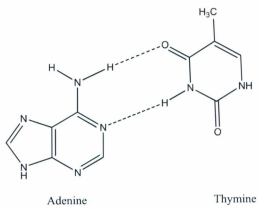


Figure 1.16: Watson-Crick base pairing for A-T and G-C.

1.4.3 Uracil

1.4.3.1 Chemical and Physical Properties

Uracil is an important nucleobase component of nucleic acid. It is found in RNA and pairs with adenine through hydrogen bonding. In base pairs, it behaves as a hydrogen bond acceptor and donor to form two hydrogen bonds with adenine. Due to the importance of this component, many studies have investigated its reactivity, acidity,⁷¹⁻⁷⁴ basicity,⁷³⁻⁷⁵ hydrogen-bonding with DNA species,⁷⁴ and interaction with metal ions.

Uracil is a weak acid with the acidic $pK_a = 9.38$. However, it has a number of sites which are responsible for its acidic behavior, such as N1 and N3. The two NH bonds in uracil and their acidities have been studied.⁷⁶⁻⁷⁹ In the gas phase, the acidities of the N1 and N3 sites are different, and the experiments indicate that the N1 is more acidic than the N3 site by at least 42 kJ/mol.⁷² In contrast, the two sites are close in acidity in aqueous solution. However, the difference in acidity in the gas phase may be explained by the fact that the N1 site is the preferred glycosylation site in nature.

In addition, metalation can play an important role in stabilization of nucleic acids and structural organization of proteins. Thus, several papers have discussed the interaction of nucleic acid bases with metal cations including the metalated uracil.⁸⁰⁻⁸²

Uracil has many derivatives which can be used in the development of medicinal drugs. An example, 5-bromouracil and 5-fluorouracil are biologically active and 5-fluorouracil has been used as anticancer drug.

1.4.3.2 Tautomerization

Tautomerization is a form of chemical reaction, isomerization, in which the same compounds differ by the position of a hydrogen atom and a pi bond. The tautomerization of nucleic acid bases is very important to the structure of nucleic acids and they have an ability to form spontaneous mutations during DNA replication.⁸³ Several studies have been carried out on the tautomerism of nucleic acids including uracil.⁸⁴⁻⁸⁹ So, uracil may exist in several tautomeric forms. The six possible tautomers of uracil are shown in Figure 1.17, where U1 is the 2,4-diketo tautomer, U2-U5 are keto-enol tautomers, and U6 is the 2,4-dienol tautomer.

Tsuchiya⁹⁰ found that the diketo tautomer was the most stable tautomer. The order of stability is $U1 > U2 > U3 > U4 > U5 > U6$. For example, the U2 tautomer is less stable than U1 by 81.8 kJ/mol in the gas phase.⁸⁶ So, the predominant tautomer in the gas phase should be U1, based on thermodynamics.

Many studies have utilized theoretical calculations which can provide information about the possible structure for the interaction of metal cations with the stable tautomer of uracil. Different tautomers of uracil show the possible positions (oxygen and/or nitrogen atom) of the metal-coordinating sites that lead to the formation of metal-base complex. In particular, the N1 and O2 positions are the preferred sites for interaction of copper ion with uracil, whereas N3 and O4 appear to be the favored positions for interactions of lead ion with uracil. The theoretical and chemical explanations of the structures of $Cu^{2+}/uracil$ and $Pb^{2+}/uracil$ as well as other $M^{2+}/uracil$ complexes are discussed in Chapter 2, 4 and 3, respectively.

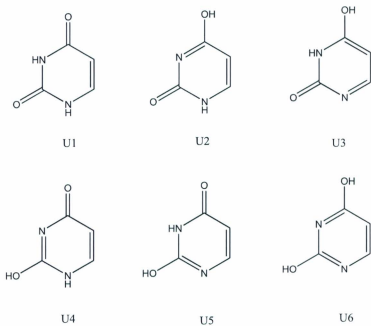


Figure 1.17: The six possible tautomers of uracil.

1.5 Theoretical Methods

Computational chemistry can be used to study the physical and chemical properties of molecular complexes such as weakly bound complexes and those involved in molecular biology. Computational methods are an important tool for helping explain experimental results and to further characterize molecular complexes.

Accordingly, computational methods have been developed to determine and study the structure of molecules with more accuracy.⁹¹⁻⁹⁴ In particular, the level of theory (method) and a basis set are used to describe the molecular orbitals. Different methods are used in theoretical studies, but the most commonly used methods in our calculations are the wavefunction theory (ab initio) and density functional theory (DFT).

1.5.1 Ab initio

The most common methods used in ab initio calculations are the Hartree-Fock (HF) and post Hartree-Fock method. Hartree-Fock theory is the simplest approximation used to solve the Schrödinger equation,⁹⁵⁻⁹⁷ as in Eq.1.9.

$$\hat{H}\Psi = E\Psi \quad \text{Eq.1.9}$$

where \hat{H} is a Hamiltonian representing the total energy, E is the total energy, and Ψ is the wavefunction. The HF theory takes into account the exchange between electrons with the same spin, while electrons with the opposite spin are not correlated.⁹⁵ So, the difference between the Hartree-Fock limit energy and the exact (experimental) is called the correlation energy (E_{corr}), as in Eq.1.10.

$$E_{corr} = E_o - E_{HFL} \quad \text{Eq.1.10}$$

where E_o is the exact non-relativistic energy and E_{HFL} is the Hartree-Fock limit energy.

Actually, the E_{HFL} would be higher than the exact energy, thus the correlation energy is always negative. However, to include electron correlation in a calculation, the wavefunction can be written as a multi-determinantal wavefunction. Therefore, many methods are used to compute the correlation energy. These methods provide more accurate results than HF due to inclusion of electron correlation. In fact, Møller-Plesset perturbation theory, MP_n , is a common type of calculation for including correlation energy into the results. MP_2 theory was used in our calculations and is the simplest cost effective perturbation theory. It is important to note that all these methods are ab initio, and do not depend on empirical parameters.

1.5.2 Density Functional Theory (DFT)

Density functional theory (DFT) is another approach to calculate molecular properties. The DFT theory depends on the electron density $\rho(r)$ rather than the wavefunction. In this theory the electron density is non-negative, and integrates to the number of electrons,⁹⁸⁻¹⁰⁰ as in the following equation.

$$N[\rho(r)] = \int \rho(r) dr = N \quad \text{Eq.1.11}$$

where $\rho(r)$ is a function of three variables (x, y, z) and $\rho(r)dr$ is the probability of finding an electron in the volume element dr at r .

Electron density is observable and can be measured by X-ray diffraction. DFT was introduced by theorems proven by Hohenberg and Kohn,¹⁰¹ which were used to establish

the DFT. Then, Kohn and Sham¹⁰² devised a method for finding ground state densities ρ_0 and ground state energies E_0 . This method depends on non-interacting electrons and their orbitals. The energy density functional has the form as in Eq.1.12.

$$E[\rho(r)] = T_s[\rho(r)] + V_{ne}[\rho(r)] + V_{ee}[\rho(r)] + \Delta T[\rho(r)] + \Delta V_{ee}[\rho(r)] \quad \text{Eq.1.12}$$

where T_s is the kinetic energy for the system of non-interacting electrons, V_{ne} is the classical potential energy in terms of the density, V_{ee} is the electrostatic electron-electron repulsion functional, ΔT is the corrections to the kinetic energy from the interacting system of the electrons, and ΔV_{ee} is the non-classical corrections to the electron-electron repulsion.

The Kohn-Sham equations are appropriate for giving the ground state density that is taken into account by using an exchange-correlation functional. For example, B3LYP is the Becke three parameters exchange functional, B3, and Lee-Yang-Parr correlation functional, LYP. B3LYP is the most popular hybrid density functional that is used and yields good structural and thermochemical properties.¹⁰³⁻¹⁰⁵ In particular, B3LYP is used exclusively as the method for optimizing structures and providing thermal contributions to energy in this thesis in our calculations. In general, DFT has advantages that include less computer time and efforts, an acceptable accuracy, and in most cases, better correlation with experimental results than those results obtained from the Hartree-Fock theory.

1.5.3 Basis Set

Choosing a good basis set is important aspect of computational calculations. Basis sets are used to create molecular orbitals. The main basis sets used in this research were 6-311++G(2d,2p) and 6-31+G(d,p). The numbers 6-311 and 6-31 represent the Gaussian function that is used to approximate each atom's atomic orbital for describing the core and valence electrons. On other hand, other common additions to the basis sets are used to enhance and improve the approximation of atomic orbitals.

As an example, diffuse functions, single plus (+) and double plus (++), describe the distance from the electrons to the nucleus. The single plus increases the diffuse functions for heavy metals, while the double plus uses diffuse functions on lighter atoms. Also, the (d,p) and (2d,2p) represent the polarization function which is used to provide flexibility for the wavefunction to change shape. These common additions are essential to describe the equilibrium geometry.

These basis sets are beneficial because they provide accurate geometries and vibrational frequencies. In addition, effective core potentials were used for the heavy elements. For example, the LANL2DZ basis set was used for Pb, while for other atoms including C, H, N, and O a 6-31+G(d,p) basis set was used to optimize the structures and calculate the vibrational frequencies.

1.5.4 Computational Procedure

Computational chemistry is an essential method used to help determine ion molecular complex structures and can even offer a useful alternative to experimental measurements if experiments are not possible. It can also be used to identify the potential

energy surface for a process and to help explain and characterize the structure of complexes. The computational method is used to attain geometry optimization, vibrational frequency, and ionic thermochemistry.

In addition, computational methods were used to simulate the IR spectra for gaseous molecules and to identify the structure of species containing divalent metals. The experimental FTIR in cryogenic matrices spectra were compared with the simulated IR spectra. Actually, to compare the experimental IR spectrum with the calculated (theoretical) IR, the scaling factor is typically used. Since, the calculations of the computed IR frequencies are done by using the harmonic approximation; the scaling factor is used to account for the anharmonicity in the calculated IR.

Most of the structure calculations were performed with Gaussian (G03)¹⁰⁶ and Gaussian (G09).¹⁰⁷ First, the structures were optimized and vibrational frequencies calculated using B3LYP with a double-zeta basis set with additional polarization and diffuse functions. These structures were submitted to single point calculations at the MP2 level of theory with triple-zeta quality basis sets, and added polarization and diffuse functions. These levels of theory are practical and give relative energetic results throughout this research. Accordingly, the thermal and Gibbs corrections were used to determine the enthalpy and Gibbs free energy values, as seen the following equations.

$$\Delta H_{\text{Theor}} = \text{Thermal correction} + E_{\text{elec}}$$

$$\Delta G_{\text{Theor}} = \text{Gibbs correction} + E_{\text{elec}}$$

In addition, we have also used density functional theory B3LYP calculations to determine the potential energy surfaces for the fragmentations.¹⁰⁵ Also, we have carried out intrinsic reaction coordinates (IRC) analysis to characterize the optimized transition states.¹⁰⁸⁻¹¹⁰ This method provides a picture for all the mechanisms proposed.

1.6 References

- (1) Marshall, A. G.; Hendrickson, C. L.; Jackson, G. S. *Fourier Transform Ion Cyclotron Resonance Mass Spectrometry: a primer. Mass Spectrom Rev* 17,1-35, 1998.
- (2) Comisarow, M. B.; Marshall, A. G. *Chem. Phys. Letter*. **1974**, 25, 282.
- (3) Dole, M.; Mack, L. L.; Hines, R. L.; Mobley, R. C.; Ferguson, L. D.; Alice, M. B. *J. Chem. Phys.* **1968**, 49, 2240.
- (4) Polfer, N. C.; Oomens, J. *Mass Spectrom. Rev.* **2009**, 28, 468.
- (5) Douglas, D. J. *J.Phys.Chem.* **1982**, 86, 185.
- (6) McLuckey, S. A. *J. Am. Chem. Soc. Mass Spectrom.* **1992**, 3, 599.
- (7) Shukla, A. K.; Futrell, J. H. *J. Mass Spectrom.* **2000**, 35, 1060.
- (8) Schwartz, R. N.; Slawsky, Z. I.; Herzfeld, K. F. *J. Chem. Phys.* **1952**, 20, 1591.
- (9) Lioe, H.; O'Hair, R. A. J. *Anal. Bioanal. Chem.* **2007**, 389, 1429.
- (10) Nelson, C. C.; McCloskey, J. A. *J.Am. Soc. Mass Spectrom.* **1994**, 5, 339.
- (11) Tso, P. O. P. *In Basic Principle in Nucleic Acid Chemistry. Academic Press, New York*, 1994.
- (12) Saegner, W. *Principles of Nucleic Acid Structure. Springer-Verlag, Berlin*, 1984.
- (13) Del Bene, J. E. *J. Phys. Chem.* **1983**, 87, 367.
- (14) Rice, J. M.; Dudek, G. O.; Barber, M. *J. Am. Chem. Soc.* **1965**, 87, 4569.
- (15) Laskin, J.; Byrd, M.; Futrell, J. *Int. J. Mass. Spectrom.* **2000**, 195/196, 285.
- (16) Laskin, J.; Futrell, J. *J. Phys. Chem. A.* **2000**, 104, 5484.
- (17) Fridgen, T. D.; McMahon, T. B. *Encyclopedia of Mass Spectrometry.* **2005**, 4, 327.
- (18) Grant, E. R.; Schulz, P. A.; Sudbo, A. S.; Shen, Y. R.; Lee, Y. T. *Phys. Rev. Lett.*

1978, *40*, 115.

- (19) Nesbitt, D. J.; Field, R. W. *J. Phys. Chem.* **1996**, *100*, 12735.
- (20) Fridgen, T. D.; McMahon, T. B. *Encyclopedia of Mass Spectrometry*. **2005**, *4*, 327.
- (21) Oomens, J.; Sartakov, B. G.; Meijer, G.; Von Helden, G. *Int. J. Mass Spectrom.* **2006**, *254*, 1.
- (22) Crowe, M. C.; Brodbelt, J. S.; Goolsby, B. J.; Hergenrother, P. *J. Am. Soc. Mass Spectrom.* **2002**, *13*, 630.
- (23) Elias, L. R.; Fairbank, W. M.; Madey, J. M.; Schwettan, H. A.; Smith, T. I. *Phys. Rev. Lett.* **1976**, *36*, 717.
- (24) O'Shea, P. G.; Freund, H. P. *Science*. **2001**, *292*, 1853.
- (25) Van Herpen, M. M. J. W.; Bisson, S. E.; Nagi, A. K. Y.; Harren, F. J. M. *Appl. Phys. B. Lasers Opt.* **2004**, *78*, 281.
- (26) Whittle, E.; Dows, D. A.; Pimentel, G. C. *J. Chem. Phys.* **1954**, *22*, 1943.
- (27) Masamune, S.; Sonto-Bachiller, F. A.; Machiguchi, T.; Bertie, J. E. *J. Am. Chem. Soc.* **1978**, *100*, 4889.
- (28) Yeo, G. A.; Ford, T. A. *Spectrochim. Acta. A*. **1991**, *47*, 485.
- (29) Nelander, B.; Nord, L. *J. Phys. Chem.* **1982**, *86*, 4375.
- (30) Engdahl, A.; Nelander, B. *J. Chem. Phys.* **1989**, *91*, 6604.
- (31) Andrews, L.; Moskovits, M. *Chemistry and Physics of Matrix Isolated Species.*; North Holland, Amsterdam, 1989.
- (32) Apkarian, V. A.; Schwentner, N. *Chem. Rev.* **1999**, *99*, 1481.
- (33) Barnes, A. J.; Orville-Thomas, W. J.; Muller, A.; Gaufres, R. *Matrix Isolation*

- Spectroscopy*; Reidel, Dordrecht., 1981.
- (34) Clark, R. J. H.; Hester, R. E. *Adv. in Spectroscopy*; Wiley, 1989.
- (35) Dunkin, I. R. *Matrix-Isolation Techniques, A Practical Approach*; Oxford University Press, UK, 1998.
- (36) Fausto, R. *Low Temperature Molecular Spectroscopy*; Kluwer Inc., Amestrdam, The Netherlands, 1996.
- (37) Wilson, E. B. J.; Decius, J. C.; Cross, P. C. *molecular Vibrations:The Theory of Infrared and Raman Vibrational Spectra*; Dover, New York, 1980.
- (38) Atkins, P. W. *Molecular Quantum Mechanics: An Introduction to Quantum Chemistry*; Clarendon Press:Oxford., 1970.
- (39) Han, S. W.; Kim, K. *J. Mol. Struct.* **1999**, 475, 43.
- (40) Dunkin, I. R. *Matrix isolation techniques:a practical approach*; Oxford University Press; New York, 1998.
- (41) Travis, D. F. FT-infrared spectroscopic and computational studies of the matrix-isolated products formed following gas phase electron bobmardment of rare-gas/organic molecule mixtures., Queen's University, 1999.
- (42) Willard, J. E. *Cryogenics.* **1982**, 359.
- (43) Hallam, H. E. *Vibrational Spectroscopy of Trapped Species*; Wiley: London, 1973.
- (44) Weber, A. *Structure and dynamics of weakly bound molecular complexes.*; Reidel,Dordrecht., 1987.
- (45) Ball, D. W.; Kafafi, Z. H.; Hauge, R. H.; Margrave, J. L. *ed.: A bibilography of matrix isolation spectroscopy*; Rice Univ.Press, Houston, 1988.

- (46) Jeffery, G. A. *An Introduction to Hydrogen Bonding*; Oxford University, Press, Oxford, 1997.
- (47) Viswanathan, K. S.; Sankaran, K.; Sundararajan, K. *Encyclopedia of Analytical Chemistry*; edited by Myers, J. B. (Wiley, New York), 2000.
- (48) Schriver-Mazzouli, L.; Schriver, A.; Schrems, O. *Can. J. Chem.* **1991**, *69*, 1520.
- (49) Luck, W. A. P.; Peil, S.; Schriver-Mazzouli, L.; Schriver, A. *J. Mol. Struct.* **1990**, *224*, 185.
- (50) Schrems, O.; Oberhoffer, H. M.; Luck, W. A. P. *J. Phys. Chem.* **1984**, *88*, 4335.
- (51) Bakkas, N.; Boutellier, Y.; Loutellier, A.; Perchard, J. P.; Racine, S. *J. Chem. Phys.* **1993**, *99*, 3335.
- (52) Zhang, X. K.; Lewars, E. G.; March, R. E.; Parnis, J. M. *J. Phys. Chem.* **1993**, *97*, 4320.
- (53) Nelander, B. *J. Chem. Phys.* **1980**, *72*, 77.
- (54) Andrews, L.; Johnson, G. L. *J. Phys. Chem.* **1984**, *88*, 5887.
- (55) Graindourze, M.; Smets, J.; Zeegers-Huyskens, T.; Maes, G. *J. Mol. Struct.* **1990**, *222*, 345.
- (56) Graindourze, M.; Grootaers, T.; Smets, J.; Zeegers-Huyskens, T.; Maes, G. *J. Mol. Struct.* **1990**, *237*, 389.
- (57) Maes, G.; Graindourze, M.; Smets, J. *J. Mol. Struct.* **1991**, *248*, 89.
- (58) Smets, J.; Graindourze, M.; Zeegers-Huyskens, T.; Maes, G. *J. Mol. Struct.* **1994**, *318*, 37.
- (59) Barnes, A. J.; Stuckey, M. A.; LeGall, L. *Spectrochim. Acta. A.* **1984**, *40*, 419.

- (60) Szczesniak, M.; Nowak, M. J.; Rostowska, H.; Szczepaniak, K.; Person, W. B.; Shugar, D. *J. Am. Chem. Soc.* **1983**, *105*, 5969.
- (61) Graindourze, M.; Grootaers, T.; Smets, J.; Zeegers-Huyskens, T.; Maes, G. *J. Mol. Struct.* **1991**, *243*, 37.
- (62) Maes, G.; Smets, J. *Vib. Spectrosc.* **1992**, *3*, 121.
- (63) Watson, J. D.; Crick, F. H. *Nature.* **1953**, *171*, 737.
- (64) Blackburn, G. M.; Gait, M. J. *Nucleic Acid in Chemistry and Biology*. Oxford University Press, New York 1996.
- (65) Neidle, S. *Oxford Hand Book of Nucleic Acid Structure*. Oxford University Press Inc.; New York, 1999.
- (66) Ulbricht, T. L. V. *Purines Pyrimidines and Nucleotides and the Chemistry of Nucleic Acids*. Pergamon Press, New York, 1964.
- (67) Florian, J.; Leszczynski, J. *J. Am. Chem. Soc.* **1996**, *118*, 3010.
- (68) Hroudá, V.; Florian, J.; Hobza, P. *J. Phys. Chem.* **1993**, *97*, 1542.
- (69) Scheiner, S.; Kern, C. W. *J. Am. Chem. Soc.* **1979**, *101*, 4081.
- (70) Florian, J.; Hroudá, V.; Hobza, P. *J. Am. Chem. Soc.* **1994**, *116*, 1457.
- (71) Lee, J. K. *Int. J. Mass. Spectrom.* **2005**, *240*, 261.
- (72) Kurinovich, M. A.; Lee, J. K. *J. Am. Chem. Soc.* **2000**, *122*, 6258.
- (73) Miller, T. M.; Arnold, S. T.; Viggiano, A. A.; Miller, A. E. S. *J. Phys. Chem. A.* **2004**, *108*, 3439.
- (74) Chandra, A. K.; Nguyen, M. T.; Uchimarú, T.; Zeegers-Huyskens, T. *J. Phys.*

Chem. A. **1999**, *103*, 8853.

- (75) Kurinovich, M. A.; Phillips, L. M.; Sharma, S.; Lee, J. K. *Chem. Commun.* **2002**, 2354.
- (76) Nguyen, M. T.; Chandra, A. K.; Zeegers-Huyskens, T. *J. Chem. Soc. Faraday Trans.* **1998**, *94*, 1277.
- (77) Meot-Ner, M. *J. Am. Chem. Soc.* **1979**, *101*, 2396.
- (78) Green-Church, K. B.; Limbach, P. A. *J. Am. Soc. Mass Spectrom.* **2000**, *11*, 24.
- (79) Greco, F.; Liguori, A.; Sindona, G.; Uccella, N. *J. Am. Chem. Soc.* **1990**, *112*, 9092.
- (80) Burda, J.; Sponer, J.; Leszczynski, J.; Hobza, P. *J. Phys. Chem. B.* **1997**, *101*, 9670.
- (81) Prado, M. A. S.; Garcia, E.; Martins, J. B. L. *Chem. Phys. Lett.* **2006**, *418*, 264.
- (82) Sponer, J.; Burda, J.; Sabat, M.; Leszczynski, J.; Hobza, P. *J. Phys. Chem. A.* **1998**, *102*, 5951.
- (83) Lowdin, P. O. *Rev. Mod. Phys.* **1963**, *35*, 724.
- (84) Broo, A.; Holmen, A. *J. Phys. Chem. A.* **1997**, *101*, 3589.
- (85) Estrin, D. A.; Paglieri, L.; Corongiu, G. *J. Phys. Chem.* **1994**, *98*, 5653.
- (86) Scanlan, M. J.; Hillier, I. H. *J. Am. Chem. Soc.* **1984**, *106*, 3737.
- (87) Civcir, P. U. *J. Mol. Struct.* **2000**, *532*, 157.
- (88) Becker, P. S.; Kogan, G. *Photochem. Photobiol.* **1980**, *31*, 5.
- (89) Leszczynski, J. *J. Phys. Chem.* **1992**, *96*, 1649.
- (90) Tsuchiya, Y.; Tamura, T.; Fujii, M.; Ito, M. *J. Phys. Chem.* **1988**, *92*, 1760.
- (91) Hehre, W. J. *Practical Strategies for Electronic Structure Calculations*. Wavefunction, Irvine, CA., 1995.

- (92) Cramer, C. J. *Essential of Computational Chemistry: Theories and Models*. Wiley, 2002.
- (93) Young, D. *Computational Chemistry: A Practical Guide for Applying Techniques to Real World Problems*. John Wiley and Sons Ltd., 2001.
- (94) Encyclopedia of Computational Chemistry. John Wiley and Sons Ltd., 1998; Vol. 5.
- (95) Szabo, A.; Ostlund, N. *Modern Quantum Chemistry: Dover publication, INC., New York*, 1996.
- (96) Levine, I. N. *Quantum Chemistry*. Prentice-Hall, Inc., New Jersey, 2000.
- (97) Pilar, F. L. *Elementary Quantum Chemistry*. McGraw-Hill publishing Company, New York, 1990.
- (98) Sahní, V. *Quantal Density Functional Theory*. Springer, Berlin, Germany, 2004.
- (99) Gross, E. K. U.; Dreizler, R. M. *Density Functional Theory*. Plenum Press, New York, 1995.
- (100) Holthausen, M. C.; Koch, W. *A Chemist's Guide to Density Functional Theory*. Wiley-VCH, Weinheim, Germany, 2001.
- (101) Hohenberg, P.; Kohn, W. *Phys. Rev.* **1964**, *136*, 864.
- (102) Kohn, W.; Sham, L. *J.Phys. Rev.* **1965**, *140*, 1133.
- (103) Lee, C.; Yang, W.; Parr, R. G. *Phys. Rev. B.* **1988**, *37*, 785.
- (104) Becke, A. D. *J. Chem. Phys.* **1993**, *98*, 5648.
- (105) Becke, A. D. *J. Chem. Phys.* **1996**, *104*, 1040.
- (106) Frisch, M. J. T., G. W.; Schlegel, H. B.; Scuseria, G. E.; Robb, M. A.; Cheeseman,

J. R.; Montgomery, J. A., Jr.; Vreven, T.; Kudin, K. N.; Burant, J. C.; Millam, J. M.; Iyengar, S. S.; Tomasi, J.; Barone, V.; Mennucci, B.; Cossi, M.; Scalmani, G.; Rega, N.; Petersson, G. A.; Nakatsuji, H.; Hada, M.; Ehara, M.; Toyota, K.; Fukuda, R.; Hasegawa, J.; Ishida, M.; Nakajima, T.; Honda, Y.; Kitao, O.; Nakai, H.; Klene, M.; Li, X.; Knox, J. E.; Hratchian, H. P.; Cross, J. B.; Adamo, C.; Jaramillo, J.; Gomperts, R.; Stratmann, R. E.; Yazyev, O.; Austin, A. J.; Cammi, R.; Pomelli, C.; Ochterski, J. W.; Ayala, P. Y.; Morokuma, K.; Voth, G. A.; Salvador, P.; Dannenberg, J. J.; Zakrzewski, V. G.; Dapprich, S.; Daniels, A. D.; Strain, M. C.; Farkas, O.; Malick, D. K.; Rabuck, A. D.; Raghavachari, K.; Foresman, J. B.; Ortiz, J. V.; Cui, Q.; Baboul, A. G.; Clifford, S.; Cioslowski, J.; Stefanov, B. B.; Liu, G.; Liashenko, A.; Piskorz, P.; Komaromi, I.; Martin, R. L.; Fox, D. J.; Keith, T.; Al-Laham, M. A.; Peng, C. Y.; Nanayakkara, A.; Challacombe, M.; Gill, P. M. W.; Johnson, B.; Chen, W.; Wong, M. W.; Gonzalez, C.; Pople, J. A.; . Gaussian 03 ed.; Gaussian, Inc.: Wallingford, 2004.

(107) Frisch, M. J. T., G. W.; Schlegel, H. B.; Scuseria, G. E.; Robb, M. A.; Cheeseman, J. R.; Montgomery, J. A., Jr.; Vreven, T.; Kudin, K. N.; Burant, J. C.; Millam, J. M.; Iyengar, S. S.; Tomasi, J.; Barone, V.; Mennucci, B.; Cossi, M.; Scalmani, G.; Rega, N.; Petersson, G. A.; Nakatsuji, H.; Hada, M.; Ehara, M.; Toyota, K.; Fukuda, R.; Hasegawa, J.; Ishida, M.; Nakajima, T.; Honda, Y.; Kitao, O.; Nakai, H.; Klene, M.; Li, X.; Knox, J. E.; Hratchian, H. P.; Cross, J. B.; Adamo, C.; Jaramillo, J.; Gomperts, R.; Stratmann, R. E.; Yazyev, O.; Austin, A. J.; Cammi, R.; Pomelli, C.; Ochterski, J. W.; Ayala, P. Y.; Morokuma, K.; Voth, G. A.; Salvador, P.; Dannenberg, J. J.; Zakrzewski, V. G.; Dapprich, S.; Daniels, A. D.; Strain, M. C.; Farkas, O.; Malick, D. K.; Rabuck, A. D.;

Raghavachari, K.; Foresman, J. B.; Ortiz, J. V.; Cui, Q.; Baboul, A. G.; Clifford, S.; Cioslowski, J.; Stefanov, B. B.; Liu, G.; Liashenko, A.; Piskorz, P.; Komaromi, I.; Martin, R. L.; Fox, D. J.; Keith, T.; Al-Laham, M. A.; Peng, C. Y.; Nanayakkara, A.; Challacombe, M.; Gill, P. M. W.; Johnson, B.; Chen, W.; Wong, M. W.; Gonzalez, C.; Pople, J. A.; . . . *Gaussian 09.; Gaussian, Inc.: Wallingford, 2008.*

(108) Fukui, K. *Acc. Chem. Res.* **1981**, *14*, 363.

(109) Gonzalez, C.; Schlegel, H. B. *J. Phys. Chem.* **1989**, *90*, 2154.

(110) Gonzalez, C.; Schlegel, H. B. *J. Phys. Chem.* **1990**, *94*, 5523.

Chapter 2

Structures and Fragmentation of [Cu(Uracil-H)(Uracil)]⁺ in the Gas Phase

2.1. Introduction*

The nucleobases, adenine, cytosine, guanine, and thymine are obviously important components of DNA, as is thymine's substitute uracil in the RNA. Many research efforts have been devoted to studying the structure and reactivity of the protonated DNA and RNA bases or those complexed with metal cations.¹⁻¹² Some studies have focused on the ability of uracil and thymine to form hydrogen bonds with other nucleobases.¹³ The presence of trace amounts of metal cations with nucleic acids plays an important role in determining the functionalities of many biological systems.^{14,15} The binding of metal ions with nucleobases may be one out of a number of factors that are responsible for stabilizing a particular conformer of the nucleic acid. In particular, copper is one of the metals which interacts with nucleic acids and it has demonstrated the highest affinity for DNA compared to other divalent metals.¹⁶ It also can cause toxicity when its concentration is over the optimal levels in cells. It has been shown that the reduction of

*This chapter has been accepted to be published as O. Y. Ali, and T.D. Fridgen, *Chem. Phys. Chem.* 2011, DOI: 10.1002/cphc.201100661.

hydrogen peroxide by a copper ion in mitochondria can produce highly reactive hydroxyl radicals that can affect DNA and cause membrane damage.^{17,18}

The interactions of bases such as uracil and thymine with various metal cations including K^+ , Li^+ , Mg^{2+} , Ca^{2+} , Zn^{2+} and Pb^{2+} have been studied using various techniques.¹⁹⁻²³ Gillis *et al.*²⁴ used IRMPD spectroscopy in the 2500-4000 cm^{-1} region to study the structures of complexes of $B_m-Li^+-(H_2O)_n$ ($n = 0, 1, 2$; $m = 1, 2$), where B= thymine or uracil. In all complexes the lithium cation was determined to be bonded to the O4 oxygen atom in both thymine and uracil, and water bound directly to the lithium cation. Furthermore, Gillis *et al.*²⁵ used the IRMPD technique to study the interaction of lithium ions with the hydrated Li^+ -bound mixed adenine and thymine complexes. Based on the experimental and theoretical results, the lithium cation was again bonded to the O4 oxygen of thymine and the A7 tautomer of adenine was attached to Li^+ through N3 and N9. Water was also found to bind directly to Li^+ .

Tautomerism of thymine has been investigated by looking at the structure of nucleobases when interacting with metal ions. As a result, many studies have examined the energetics and structures of thymine and uracil with metals such as Mg^{2+} , Zn^{2+} and Cu^{2+} .²⁶ Through computational methods Lamsabhi *et al.*²⁷ found that the lowest energy complex between Cu^{2+} and uracil is deprotonated at N1 and that Cu^{2+} binds to the deprotonated nitrogen and the oxygen atom of the adjacent carbonyl group. These studies¹ consisted of detailed collision induced dissociation (CID) experiments of electrosprayed $[Cu(Ura-H)]^+$ augmented by electronic structure calculations on the structures and potential energy surfaces for dissociation to the various fragments. Low

energy CID of $[\text{Cu}(\text{Ura-H})]^+$ showed primary losses of HNCO and NCO radicals with CO loss being a minor decomposition route. By using different isotopically labeled uracils, the spectra indicated that both the loss of HNCO and NCO radical correspond to the N3 and C2 atoms, while the loss of CO involves the C4 atom. Their experiments and calculations supported the existence of the N1/O2 bound complex (deprotonated at N1 with Cu bound to N1 and carbonyl oxygen of C2) but also other-much higher energy-isomers.

The purpose of the present study is to explore the structures of copper (II) complexes comprised of two uracils by studying the fragmentation of these complexes in the gas phase. Tandem mass spectrometry techniques, such as CID and CO_2 laser IRMPD of the ions trapped in a Fourier transform ion cyclotron resonance mass spectrometer, were used in combination with theoretical calculations to determine the structures of these $[\text{Cu}(\text{Ura-H})(\text{Ura})]^+$ complexes. In order to better understand the structure of electrosprayed $[\text{Cu}(\text{Ura-H})(\text{Ura})]^+$, it was deemed important to better understand the structure(s) of the $[\text{Cu}(\text{Ura-H})]^+$ complex. Gas phase calculations of $[\text{Cu}(\text{Ura-H})]^+$ structures were also done and these results are also presented herein. Since the ions are born in solution, we also performed calculations using a solvent model to shed some light on which structures may be present in solution. Rajabi et al.²⁸ studied the solvent effect on the stability of the protonated dimers of adenine and found that the solvent stabilizes the observed isomers such that those seen in the gas phase represent those in solutions.

2.2. Methods

2.2.1 Experimental

All experiments were conducted on a Bruker ApexQe hybrid quadrupole-Fourier transform ion cyclotron resonance (FT-ICR) mass spectrometer equipped with an Apollo II electrospray ion source which is considered to be a fairly soft method of ionization. The uracil and copper (II) chloride used in this study were purchased from Aldrich and used without any further purification. 1 mM solutions of uracil and copper chloride were prepared in 18 M Ω H₂O. [Cu(Ura-H)(Ura)]⁺ complexes were electrosprayed from 1 mM solutions of nucleobase (10 ml) to which a few (5-10) drops of the 1 mM copper chloride solution have been added. The solutions were introduced to the electrospray source using a syringe pump with a flow rate 100 μ L/hr. The spray shield and capillary inlet were biased at 3900 and 4400 V, respectively, and the capillary exit was maintained at 300 V. A deflector plate at 256 V directed ions perpendicular to the capillary axis through two sets of ion funnels. [⁶³Cu(Ura-H)(Ura)]⁺ complexes at *m/z* 286 (depending on the isotopomer), were mass selected in the quadrupole mass filter and stored in the accumulation/collision cell for 2 s prior to the transfer to the ICR cell. The source pressure was on the order of 10⁻⁶ mbar and the ICR pressure was maintained at 10⁻¹⁰ mbar.

CID experiments, external to the ICR cell were conducted by accelerating the ions between the quadrupole and the collision cell filled to \sim 10⁻² mbar with Ar at collision energies from 5-20 eV, lab frame or 0.6-2.5 eV in the centre of mass (c.o.m.) frame of reference. Sustained off-resonance irradiation collision-induced dissociation (SORI/CID)

was done inside the ICR cell following a pulse of Ar to a pressure of 10^{-8} mbar. SORI powers ranged from about 3.2 eV - 11.4 eV lab frame, or 0.39-1.4 eV in the centre of mass frame. In all cases SORI was done for 250 ms followed by a 2 s delay to allow the collision gas to be pumped from the ICR cell prior to detection. Various stages of SORI-CID were used to identify the primary, secondary, and tertiary fragmentation pathways. IRMPD was also used to perform softer fragmentation using a continuous 25 W CO₂ laser (10.6 μ m wavelength) operating at 80% of maximum power. The IR pulse lengths were between 0.1-0.4 s.

2.2.2 Computational

All calculations were performed using Gaussian 09.²⁹ Initially, all the structures were optimized and vibrational frequencies calculated using B3LYP/6-31+G(d,p) level of theory. Single point calculations were done on all optimized geometries using B3LYP/6-311+G(2df,2p) on C,N,O, and H and 6-311+G on Cu to obtain more reliable thermochemical values, which are hereon called B3LYP/6-311+G(2df,2p)//B3LYP/6-31+G(d,p). It should be noted though that the basis set for the single point calculations is 6-311+G. All reported thermochemical data are 298 K values. All thermochemistries derived from the vibrational frequencies were used without scaling and are abbreviated as B3LYP. Transition states were identified by the imaginary frequency in the correct reaction coordinate and by intrinsic reaction coordinate (IRC) calculations. All solvent model calculations were done with the same level of theory and basis sets, initially optimizing the structures within the polarizable continuum model (PCM) with water as the dielectric and submitting these geometries to single point calculations, also within the

PCM, with the larger basis set.

2.3. Result and Discussion

2.3.1 Positive Ion Electrospray Spectra of Copper (II)/ Nucleobase Solutions

A positive-ion electrospray spectrum of an aqueous mixture of copper chloride with uracil is presented in Figure 2.1. Species containing one or more copper atoms can be readily identified based on their isotopic distributions due to the ^{63}Cu and ^{65}Cu isotopes, see Appendix 1. The most abundant complexes observed are $[\text{Cu}(\text{Ura-H})(\text{Ura})]^+$ at m/z 286 and 288. In addition, the set of peaks with a maximum at m/z 322.0 is identified as $[\text{Cu}(\text{Ura})_2\text{Cl}]^+$ based on the masses and intensities of the isotopic peaks. Another set of peaks detected at m/z 398.0 is identified as a $[\text{Cu}(\text{Ura-H})(\text{Ura})_2]^+$ ion composed of three uracils. The masses and intensities of the isotopic peaks help to identify the set of peaks at m/z 461.0 to the $[(\text{Ura})_2\text{Cu}_2(\text{Ura-H})]^+$ ion. The m/z 247 peak is the sodium ion bound dimer, $[(\text{Ura})_2\text{Na}]^+$. While many different concentrations of base were used, as well as solvent combinations-pure or aqueous methanol or acetonitrile solutions-no monomer ion, $[\text{Cu}(\text{Ura-H})]^+$, such as that studied in previous work,¹ was observed. A possible reason for not observing $[\text{Cu}(\text{Ura-H})]^+$ is that our source might be softer, resulting in a undetectable source decomposition of the $[\text{Cu}(\text{Ura-H})(\text{Ura})]^+$ ions.

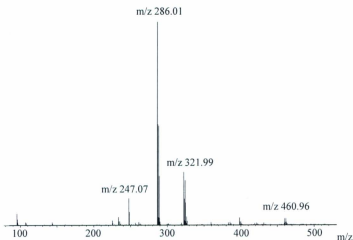


Figure 2.1: Positive-ion electrospray mass spectrum of an aqueous solution of CuCl_2 and uracil.

In an attempt to spectroscopically determine the structure of $[\text{Cu}(\text{Ura-H})(\text{Ura})]^+$, we tried to do wavelength-dependent IRMPD (IR spectroscopy) with an OPO laser²⁵ but the complex proved to be too strongly bound to dissociate with this low powered laser in contrast to other metal cationized uracil complexes^{24,25} including $[\text{Pb}(\text{Ura-H})(\text{Ura})]^+$.²³ In further attempts to spectroscopically characterize $[\text{Cu}(\text{Ura-H})(\text{Ura})]^+$ we unsuccessfully tried to hydrate the ion in the hexapole ion trap of our instrument.³⁰ We believe that the inability to hydrate $[\text{Cu}(\text{Ura-H})(\text{Ura})]^+$ could be due to the charge being delocalized over the entire complex, unlike in $\text{Li}^+(\text{Ura})_2$ ²⁴ and $\text{M}^+(\text{Ade})_2$ complexes ($\text{M} = \text{Li}, \text{Na}, \text{K}, \text{Cs}$)³¹ whose hydrated complexes have been studied previously by the same method. We decided to probe the structure of $[\text{Cu}(\text{Ura-H})(\text{Ura})]^+$ through fragmentation and

computational studies. The remainder of this chapter is focused on the exploration of the structure of $[\text{Cu}(\text{Ura-H})(\text{Ura})]^+$ through fragmentation methods (CID/SORI/IRMPD) and electronic structure calculations.

2.3.2 Results of Fragmentation Experiments on $[\text{Cu}(\text{Ura-H})(\text{Ura})]^+$

Surprisingly, all experiments aimed at fragmentation of $[\text{Cu}(\text{Ura-H})(\text{Ura})]^+$ in the ICR cell or externally resulted primarily in the loss of HNCO rather than of uracil, as was the case for source collisions in the previous experiments.¹ MS/MS spectra of the $[\text{Cu}(\text{Ura-H})(\text{Ura})]^+$ complex were recorded at a number of different SORI collision energies, seen in Figure 2.2A, following isolation of m/z 286 inside the ICR cell. The main fragmentation products for $[\text{Cu}(\text{Ura-H})(\text{Ura})]^+$ are loss of 43 Da and at 70 Da, corresponding to the loss of HNCO and HNCO/HCN, respectively, as seen in Figure 2.2A. Minor products are observed at m/z 242, 202, 188, 160 and 104. At higher collision energies m/z 174 and 175, corresponding to losses equal to the mass of uracil and uracil-H, respectively, are observed to grow and at even higher SORI-CID energies more extensive fragmentation is observed, as expected, with peaks at m/z 131 and 132, corresponding to losses of HNCO and NCO radical from m/z 174.¹

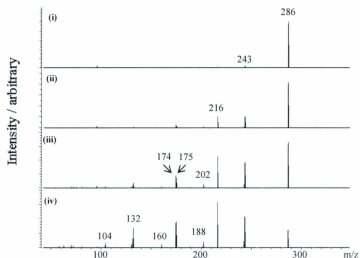


Figure 2.2A: MS/MS spectra of $[\text{Cu}(\text{Ura})(\text{Ura-H})]^+$ complex were recorded at different SORI collision energies; a) 0.39 b) 0.66 c) 0.99 , and d) 1.39 eV (c.o.m.) by using SORI method in fragmentation.

2.3.2.1 MS^n Experiments on $[\text{Cu}(\text{Ura-H})(\text{Ura})]^+$

To better ascertain a complete map of the fragmentation pathways, MS^3 experiments were conducted and the main results are displayed in Figure 2.2B for the normal isotopomer. Isolation and SORI-CID of m/z 243 produced by SORI-CID of m/z 286 (Figure 2.2Bii) resulted in a virtually identical fragmentation pattern as that produced by SORI-CID of m/z 286 (Figure 2Bi). This means that m/z 286 dissociates to form m/z 243 as the primary decomposition pathway and that all other ions are grand-daughter ions born from m/z 243. The presence of m/z 242 in the SORI-CID spectrum of

m/z 243 indicates that m/z 242 results from loss of H from m/z 243, rather than loss of H_2NCO from 286. SORI-CID of m/z 216 results in a spectrum which contains m/z 188, 160 and 104 as prominent product ions along with ions at m/z 174, 131, and 132, but is devoid of m/z 202 and almost completely bereft of m/z 175. The ions at m/z 202, and 175, then, come mainly from m/z 243 losing 41, and 68 Da, respectively. Isolation and SORI-CID of m/z 174 resulted in a mass spectrum with no ions at m/z 160 or 104, so these ions are certainly born from m/z 216. $[Cu(Ura-H)]^+$ was previously seen to lose NCO and HNC0 producing ions at m/z 132 and 131, respectively, and a minor loss of CO producing m/z 146.¹ The present results are completely congruent with these last observations. These SORI-CID experiments were reproduced following isolation of $[^{65}Cu(Ura-H)(Ura)]^+$ (see Appendix 2). The results, with the ^{65}Cu isotopomer, confirmed that all ionic fragments observed retain the metal Cu.

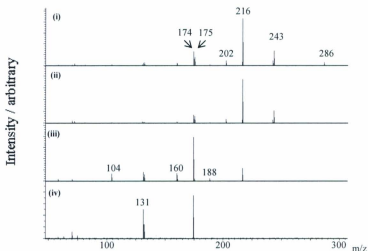


Figure 2.2B: SORI MS/MS of the main fragment ions (i) m/z 286 (ii) m/z 243 (iii) m/z 216, and (iv) 174.

2.3.2.2 MSⁿ Experiments with 2-¹³C Labeled Uracil

The SORI-CID experiments just described were repeated with uracil, which was isotopically labeled with ¹³C at C2. The results are shown in Figure 2.2C. The parent ion is now at m/z 288 as $[\text{Cu}(\text{Ura-H})(\text{Ura})]^+$ is doubly labeled (C2 of each uracil). Losses of 44 and 71 Da, corresponding to HN^{13}CO and $\text{HN}^{13}\text{CO}/\text{HCN}$, respectively, produce ions at m/z 244 and 217, each with loss of one of the labels. When m/z 244 is isolated and submitted to SORI-CID, the main loss of HCN at m/z 217 is observed. Minor losses of H to produce m/z 243, HCCO radical (41 Da) to produce m/z 203, and $\text{H}_2\text{C}_3\text{NO}$ (68 Da) to produce m/z 176 are also observed. These results are all consistent with the ions keeping the second 2-¹³C label and the suggestion that m/z 176, $[\text{Cu}(\text{Ura})]^+$, probably

contains an intact uracil. As in the non-labeled experiments for m/z 216, when m/z 217 is isolated and submitted to SORI-CID it does not produce the ions at m/z 203, or 176 so that these ions are produced solely from m/z 244. The m/z 217 ion loses 42 Da to produce m/z 175, which is consistent with the major loss from m/z 216 in the non-labeled experiments being the loss of C_2H_2O -likely ketene-leaving $[Cu(Ura-H)]^+$. It also loses 28 Da to produce m/z 189 and 57 Da to form m/z 160. The two minor fragmentation routes, m/z 217 \rightarrow 189 and m/z 217 \rightarrow 160 are also observed as m/z 216 \rightarrow 188 and m/z 216 \rightarrow 160 in the non-labeled experiments. These results show that loss of 28 Da from m/z 216 does not include the label and, if it is CO loss, it must be exclusively from the C4 position. Furthermore loss of 56 Da from m/z 216, and loss of 57 Da from m/z 216 in the C2 labeling experiments, show that this loss must contain C2 and could have the following possible molecular formulae $(CO)_2$, CON_2 , C_2H_2ON , or C_3H_4O based on the mass of the neutral loss.

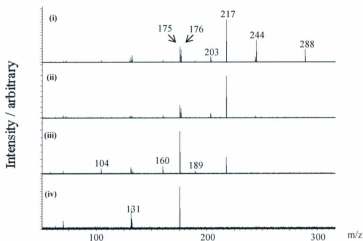


Figure 2.2C: SORI MS/MS of the main fragment ions of $[\text{Cu}(\text{Ura-2-}^{13}\text{C})_2\text{-H}]^+$ (i) m/z 288 (ii) m/z 244 (iii) m/z 217, and (iv) 175.

2.3.2.3 MS^n Experiments with $3\text{-}^{15}\text{N}$ and $1,3\text{-}^{15}\text{N}$ Labeled Uracil

The SORI-CID experiments were repeated with $3\text{-}^{15}\text{N}$ labeled uracil, where both uracils in $[\text{Cu}(\text{Ura-H})(\text{Ura})]^+$ are labeled (Figure 2.2D). The results of these experiments show that the primary HNCN loss from $[\text{Cu}(\text{Ura-H})(\text{Ura})]^+$ also includes N3 as was seen in the HNCN loss from $[\text{Cu}(\text{Ura-H})]^+$.¹ Similarly, HCN loss from m/z 244 (or m/z 243 in the non-labeled experiments) does not include a label. These experiments also show that the m/z 217 fragment ion forms m/z 189 and m/z 160. In experiments with $1,3\text{-}^{15}\text{N}$ labeled uracil (see Appendix 3), m/z 218 loses 28 Da to form m/z 190 and 57 Da to form m/z 161. Clearly, the 28 Da loss from m/z 218 route does not contain nitrogen. Although we cannot completely rule out that this neutral loss from m/z 218 is not C_2H_4 at this

point, its most likely identity is CO stemming from the C4 position, based on the 2-¹³C experiments. The loss involving 57 Da from m/z 217 and m/z 218 in the 3-¹⁵N and 1,3-¹⁵N experiments is interesting as it shows that this fragment contains only N3. Along with the results of the 2-¹³C experiments, showing that this fragment contains C2, the only possible molecular formula would be CONCH₂, making the plausible assumption that O2 is lost with C2.

The ion at m/z 104 shows up in all the isotopic labeling experiments so far discussed (and the normal isotope experiment), and therefore does not include nitrogen or C2. It's most likely identity is Cu(HCCO)⁺ and it is probably produced by loss of an intact uracil molecule from m/z 216. The fact that no m/z 105 is observed in any labeling experiments so far means that loss of deprotonated uracil is not competitive with loss of a ketene molecule from m/z 216 which presumably forms m/z 174.

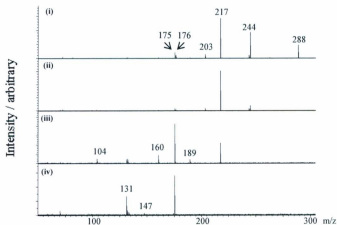


Figure 2.2D: SORI MS/MS of the main fragment ions of [Cu(Ura-3-¹⁵N)₂-H]⁺ (i) m/z 288 (ii) m/z 244 (iii) m/z 217, and (iv) 175.

2.3.2.4 MSⁿ Experiments with 5-d and 6-d- Labeled Uracil

In Figures 2.2E and 2.2F are the results of MSⁿ experiments on 5-d-labeled [Cu(Ura-H)(Ura)]⁺ and 6-d-labeled [Cu(Ura-H)(Ura)]⁺, respectively. Results of both experiments produce m/z 245, retaining their respective labels, which is consistent with HNCO loss where H is originally from N3. Interestingly, there is a minor amount of m/z 244 in the 5-d experiments, but in the 6-d experiments there is no 244, but only 243 which means that the minor secondary loss of hydrogen atom from the product of primary HNCO loss is solely from the C6 position.

In the 5-d experiments, m/z 218 results from loss of HCN from m/z 245 whereas in the 6-d experiments the m/z 217 product ion results from loss of DCN from m/z 245. This suggests that loss of HCN includes the HC moiety from the C6 position. The m/z 245 ion also loses DCCO in the 5-d experiments to form m/z 203. In the 6-d experiments, m/z 245 loses a HCCO radical to form m/z 204. These latter results are consistent with a HCCO radical loss where the HC stems from the C5 position. In both cases m/z 176 is formed from m/z 245 consistent with the complete loss of Ura-H forming [Cu(Ura)]⁺.

In the 5-d and 6-d experiments, the main product from SORI-CID of both m/z 218 and m/z 217 is m/z 175, which would be formed by loss of OCCHD and OCCH₂, ketene, respectively. The m/z 218 ion in the 5-d experiments and the m/z 217 ion in the 6-d experiments both lose uracil (5-d- or 6-d-uracil, respectively) forming m/z 105 and m/z 104, respectively, a ketylenyl-Cu complex ion, retaining a label in the 5-d experiments. The 5-d labeling experiments confirm that the loss of 28 Da from the m/z 216 ion in the

non-labeled experiments is CO, as 28 Da is also lost from m/z 218 in the 5-d and there are not enough hydrogens in the complex for m/z 28 to be the unlikely loss of C_2H_4 . Finally, both the m/z 218 and 217 ions, in the 5-d and 6-d experiments, produce an ion at m/z 161, meaning that OCNCHD is lost in the 5-d experiment and OCNCH₂ in the 6-d experiments.

2.3.2.5 IRMPD Experiments

IRMPD tends to be a softer process than CID, meaning that the incremental energy deposition of $\sim 10 \text{ kJ mol}^{-1}$ per absorbed photon is lower than the $\sim 30 - 130 \text{ kJ mol}^{-1}$ (maximum in these experiments) that can be deposited per collision in SORI-CID. The drawback for IRMPD is that the fragments themselves can absorb photons and dissociate. In SORI only the ion of interest is excited (off resonantly), so the only way product ions can be internally excited is by leaving the initial fragmentation process with internal energy. In Appendix 4, the mass spectra following IRMPD dissociation of m/z 286, 243, 216 and 174 are presented. These results confirm that the major primary dissociation routes for each of the ions is m/z 286 \rightarrow 243 \rightarrow 216 \rightarrow 174 \rightarrow 131. The dissociation of m/z 216, to produce m/z 174, however, is in competition with the losses of 28 Da and 56 Da to produce m/z 188 and m/z 160 and to a much lesser extent the route forming m/z 104.

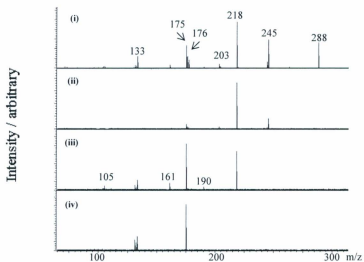


Figure 2.2E: SORI MS/MS of the main fragment ions of $[\text{Cu}(\text{Ura-d}5)_2\text{-H}]^+$ (i) m/z 288 (ii) m/z 244 (iii) m/z 217, and (iv) 175.

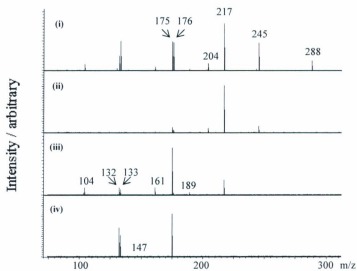


Figure 2.2F: SORI MS/MS of the main fragment ions of $[\text{Cu}(\text{Ura-d}6)_2\text{-H}]^+$ (i) m/z 288 (ii) m/z 244 (iii) m/z 217, and (iv) 175.

2.3.3 Discussion

2.3.3.1 [Cu(Ura-H)(Ura)]⁺ Structures.

There are many possible isomeric structures for the [Cu(Ura-H)(Ura)]⁺ ion. Prior to discussing the mechanism for the observed [Cu(Ura-H)(Ura)]⁺ fragmentation, it is necessary to digress slightly to explore the possible structures for this ion. To get a better understanding of the [Cu(Ura-H)(Ura)]⁺ structure it is instructive to first know the structure of the [Cu(Ura-H)]⁺ core and to then build upon this core a second uracil. Fortunately, Lamsabhi *et al.*¹ have studied the structures of the [Cu(Ura-H)]⁺ complex, both experimentally using MS/MS and computationally using B3LYP/6-311+G(2df,2p). It was determined that [Cu(Ura-H)]⁺ exists in various geometries but that the most stable isomer is the one where Cu is bound to deprotonated N1 and O2 as seen in Figure 2.3. They also found that the copper atom can bridge between N3 and O4 but this structure is more than 30 kJ mol⁻¹ higher in enthalpy than the minimum-energy geometry. A third isomer, where Cu is bound to deprotonated N3 and O2, is 45 kJ mol⁻¹ higher in enthalpy relative to the lowest energy structure and a π -complex was found to be 177 kJ mol⁻¹ higher than the lowest energy isomer. Several experiments and theoretical studies have shown the acidity at positions N1 and N3 are similar in aqueous solution in contrast to the gas phase, where N1 is the most acidic site with N3 deprotonation being higher in energy by some 60 kJ mol⁻¹.³²⁻³⁵ Solvent model calculations were performed on the [Cu(Ura-H)]⁺ complexes which reveal that the N1O2 and N3O4 structures are virtually isoenergetic. Furthermore, the N3O2 structure is only about 10 kJ mol⁻¹ higher in enthalpy, and the π -bound complex remains a high energy isomer being 190 kJ mol⁻¹

higher in enthalpy than the N1O2 structure as seen in Figure 2.3.

Using electronic structure calculations, Lamsabhi *et al.*¹ showed that the mechanism for loss of HNCO from $[\text{Cu}(\text{Ura-H})]^+$ occurred from the minimum energy N1O2 structure, but to explain NCO radical loss, they assumed that the π -bound structure, 176 kJ mol⁻¹ higher in energy, was the precursor. Due to the relatively high energy of the π -bound structure it is unlikely, in our opinion that any exists in an observable quantity, even in the high-energy environment of the source region. Certainly this high energy isomer does not exist in enough abundance to account for the almost equal intensity of the HNCO and NCO radical loss routes in the CID mass spectrum of $[\text{Cu}(\text{Ura-H})]^+$. However, a path from the N3O4 structure to loss of NCO that includes the π -N3C5 structure as an intermediate (Appendix 5) was revealed. This pathway does not require the existence of the high energy π -N3C5 structure in the source, but only the existence of the N3O4 structure which was predicted by solvent model calculations to be isoenergetic with the N1O2 structure in the aqueous solution from which $[\text{Cu}(\text{Ura-H})]^+$ was electrosprayed. These computational results also account for the almost equal intensity of the NCO and HNCO loss routes from $[\text{Cu}(\text{Ura-H})]^+$ in the Lamsabhi *et al.*¹ work since both the N1O2 and N3O4 structures are predicted to be isoenergetic in solution. What this means for the work herein is that, in our calculations of $[\text{Cu}(\text{Ura-H})(\text{Ura})]^+$ structures, we are only really able to disregard the very high energy π -bound structures, but must consider all structures with N1O2, N3O4 and N3O2 type cores, to which we add neutral uracil to formulate possible structures for $[\text{Cu}(\text{Ura-H})(\text{Ura})]^+$.

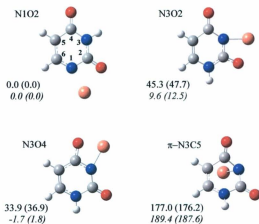


Figure 2.3: Isomers of $[\text{Cu}(\text{Ura-H})]^+$ as determined by theoretical methods as well as B3LYP/6-311+G(2df,2p) calculated Gibbs free energies, the relative enthalpies in parentheses. The Gibbs free energies and the enthalpies in parentheses in italic are for the solvent-phase calculations.

In Figure 2.4 a subset of the twenty-seven computed structures for the $[\text{Cu}(\text{Ura-H})(\text{Ura})]^+$ complex are presented. All twenty-seven structures and their relative enthalpies and Gibbs free energies are provided in Appendix 6. To name the structures, the binding of Cu to the deprotonated uracil (always on the left of the structure in Figures 2.4 and Appendix 6) is given first. N3O4 means that Cu is bound to N3 and O4 of the deprotonated uracil whereas N1 means that Cu is only bound to N1. The second term (following “ π ”) indicates the binding of Cu to the non-deprotonated uracil. The term in parentheses indicates the tautomerization of the non-deprotonated uracil and whether or not there is an intramolecular hydrogen bond between the two uracil moieties. (O4-O2)

means that the non-deprotonated uracil has a hydrogen on O4 and that this O-H is hydrogen bonded to O2 of the deprotonated uracil. (O2Hc) for example, means that the hydrogen is on O2 of the non-deprotonated uracil and that the O-H bond is directed toward the other uracil (c) as opposed to being directed away from the other uracil (t). The twenty-seven isomers presented in Appendix 6 is not a comprehensive catalogue of all possible $[\text{Cu}(\text{Ura-H})(\text{Ura})]^+$ structures since the very high energy double imide tautomers are ignored.

The three lowest energy structures all have four-coordinate Cu and an intramolecular hydrogen bond. N3O4/N3O2(O4-O2), N3O4/N3O4(O2-O2), and N3O2/N3O2(O4-O4) are all very similar in energy (Figure 2.4). Attempts to optimize of an N3O2/N3O4(O2-O4) structure ended up in a proton transfer resulting in the N3O4/N3O2(O4-O2) isomer. Comparison of these three lowest energy structures reveals that there is only a slight preference for the structure binding N3O4 on the deprotonated uracil over N3O2. Considerably higher in energy are those structures with three-coordinate Cu and structures where there is no hydrogen bond. For example, N3O2/N3O2(O4H) is 77.3 kJ mol^{-1} higher in enthalpy than the lowest energy structure and 70.0 kJ mol^{-1} higher in energy than a very close isomer N3O2/N3O2(O4-O4), only differing by a rotation of the uracil moiety. This shows the importance that the intramolecular hydrogen bond can have in stabilizing these complexes. The structures with uracil deprotonated at N3 are typically lower in energy than those deprotonated at N1 as is seen in Appendix 6.

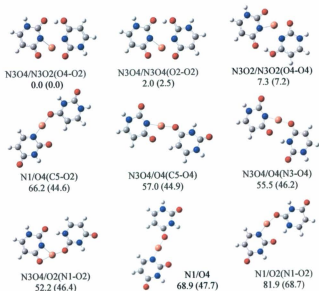


Figure 2.4: Nine of the lowest energy $[\text{Cu}(\text{Ura-H})(\text{Ura})]^+$ structures, of the twenty-seven computed structures (see Appendix 6 for all structures). Enthalpies and Gibbs energies (parentheses) are computed at the MP2/6-311+G(2df,2p)//B3LYP/6-31+G(d,p) level of theory and are in kJ mol^{-1} relative to the lowest energy structure.

2.3.3.2 Mechanistic Aspects of $[\text{Cu}(\text{Ura-H})(\text{Ura})]^+$ CID

Experiments showed that the primary dissociation pathway is loss of HNCO from $[\text{Cu}(\text{Ura-H})(\text{Ura})]^+$ and that the loss includes one of the C2 carbon and one of the N3 nitrogens. However, simple cleavage of HNCO directly from the lowest energy structure, (N3O4/N3O2(O4-O2)), without extensive isomerization would include loss of N1 since the N3's are strongly bound to copper. Prior to fragmentation, it is therefore necessary to isomerize to a structure where neutral HNCO (including C2 and N3) can be lost and the remaining binding to Cu would stay intact. This latter criterion is due to the observation that fragmentation of the uracil ring is preferential over fission of the Cu-uracil bonds, meaning that the Cu-uracil bonding is quite strong. Some of the N1-deprotonated isomers provide for facile loss of HNCO (including C2 and N3) while not interfering with the Cu-binding sites.

Isomerization from the lowest energy structures to an N1-deprotonated structure would require extensive isomerization, involving proton (or hydrogen) transfer isomerization reactions and the barriers to these reactions would need to be lower in energy than cleavage of uracil from the complex, as well as the observed primary fragmentation of the complex, loss of HNCO. A potential energy surface connecting the lowest energy structure, N3O4/N3O2(O4-O2), to an N1/O2 complex, specifically N1/O2(N1-O2) can be seen in Figure 2.5. This potential energy surface shows that the largest Gibbs energy barrier to isomerization is 211.2 kJ mol⁻¹. The lowest-energy dissociation pathway of $[\text{Cu}(\text{Ura-H})(\text{Ura})]^+$ to neutral uracil and $[\text{Cu}(\text{Ura-H})]^+$ (N1O2) is calculated to be slightly higher in Gibbs energy, 218.3 kJ mol⁻¹. Therefore, isomerization

is in fact preferred over loss of neutral uracil, according to these calculations.

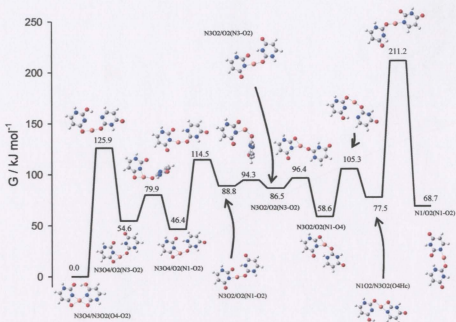


Figure 2.5: Potential energy surface corresponding to manipulating the lowest energy possible structure to the complex N1/O2 (N1-O2).

At this point mechanistic schemes for the observed fragmentations from $[\text{Cu}(\text{Ura-H})(\text{Ura})]^+$ can be suggested. We begin with the N1/O2(N1-O2) structure. The proposed fragmentation pathways are presented in Figure 2.6 along with the suggested neutral fragments and a Gibbs free energy level diagram is shown in Figure 2.7. The same fragmentation schemes as shown in Figure 2.6 are provided in Appendices 7-11, showing the position of the isotopic labels. The presented fragmentation schemes must account

for the loss or retention of isotopic labels, which this scheme does.

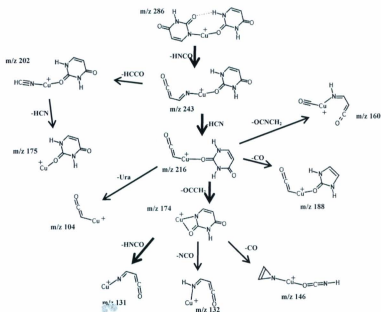


Figure 2.6: Proposed fragmentation pathways for the observed fragments from $[\text{Cu}(\text{Ura-H})(\text{Ura})]^+$.

The parent ion, m/z 286, loses HCNCO to form m/z 243. It can be concluded from the isotopic labelling studies that this primary fragmentation includes C2 (and therefore O2) and N3. This loss is similar to the loss seen from $[\text{Cu}(\text{Ura-H})]^+$ and it seems reasonable to suggest that the present HCNCO loss from $[\text{Cu}(\text{Ura-H})(\text{Ura})]^+$ is from the Ura-H moiety rather than Ura. While both are possible, loss of HCNCO from Ura is

energetically less favorable ($202.6 \text{ kJ mol}^{-1}$) than from Ura-H ($173.2 \text{ kJ mol}^{-1}$, Figure 2.7). Also, the secondary and latter fragmentation routes, discussed below, suggest that HNCO loss is from (Ura-H). Figure 2.7 also shows that the loss of HNCO is significantly lower in energy (44.8 kJ mol^{-1}) than loss of a uracil molecule,

The thermodynamic differences, though, cannot account for the reason why HNCO is observed to be the main fragmentation route rather than loss uracil from $[\text{Cu}(\text{Ura-H})(\text{Ura})]^+$. Simple cleavage of uracil is likely a barrierless process, but is endothermic by about 284 kJmol^{-1} . We identified a complex between m/z 243 and HNCO which is bound by 57 kJmol^{-1} compared to complete loss of HNCO (see Figure 2.7). Lamsabhi et al. also determined the enthalpy barrier for loss of HNCO from $[\text{Cu}(\text{Ura-H})]^+$ to 235 kJmol^{-1} from the lowest energy structure, which is below the endothermicity of HNCO loss computed for $[\text{Cu}(\text{Ura-H})(\text{Ura})]^+$. While we provided hand-wavy evidence to suggest that the overall energy requirement for HNCO loss is lower than the energy requirement for uracil loss form $[\text{Cu}(\text{Ura-H})(\text{Ura})]^+$, this must be the case since HNCO is experimentally observed to be the main product from SORI-CID and IRMPD activation.

The ion at m/z 175 is undoubtedly Cu bound to an intact uracil formed by loss of the rest of the (Ura-H) moiety ($\text{OC}_3\text{H}_2\text{N}$) that was left after loss of HNCO from the parent ion. This $\text{OC}_3\text{H}_2\text{N}$ group fragments in two other ways as well, by the loss of HCCO radical and loss of HCN. The major secondary fragmentation was observed for m/z 243 through loss of HCN forming m/z 216. HNCO loss followed by HCN loss was also seen for $[\text{Cu}(\text{Ura-H})]^+$.¹ Isotopic labeling confirms that the loss of HCN route includes H from C6 which strongly suggests that C6 and N1 also comprise neutral HCN

loss. The HCN loss is from the remnants of the (Ura-H) moiety following HNCO loss which leaves the $[\text{Cu}(\text{HCCO})(\text{Ura})]^+$ structure. The loss of HCCO radical from m/z 243 forms m/z 202 which is most likely $[\text{Cu}(\text{NCH})(\text{Ura})]^+$. The Gibbs free energy diagram of Figure 2.7 shows that HCN loss is 32.5 kJ mol^{-1} lower in energy than loss of HCCO which is consistent with HCN loss being the major fragmentation route for m/z 243. At this point it is not possible to tell whether m/z 175 is formed by a sequential loss of HCCO radical and then HCN from m/z 243 or in one step, losing $\text{OC}_3\text{H}_2\text{N}$ from m/z 243. Due to the small amount of m/z 202 it was not possible to isolate and obtain a signal following SORI-CID. It was seen experimentally, though, that m/z 216 produces only a very small amount of m/z 175 at best (Figure 2.2B) but not enough to account for the amount seen in the SORI-CID of m/z 243. Calculations show that loss of $\text{OC}_3\text{H}_2\text{N}$ from m/z 243 is more than 100 kJ mol^{-1} higher in Gibbs energy than loss of HCCO radical [$368.5 \text{ kJ mol}^{-1}$ with respect to $\text{N}_3\text{O}_4/\text{N}_3\text{O}_2(\text{O}_4-\text{O}_2)$]. This is far too high in energy to be competitive with the HCN and HCCO routes for low energy CID. It is therefore concluded that m/z 175 is a product of fragmentation (loss of HCN) from m/z 202 as seen in Figures 2.6 and 2.7.

The m/z 216 ion undergoes four competing fragmentations. The main decomposition route is loss of H_2CCO , ketene. Isotopic studies show that one of the hydrogens comes from C5, and therefore C5 itself as well as C4 and O4. The other hydrogen must come from one of the nitrogens of m/z 216. It is proposed that a hydrogen from N1 of the intact uracil is transferred to HCCO to eliminate ketene forming m/z 174. Experimentally we cannot confirm whether it is hydrogen from N1 or N3 that is

transferred, but thermodynamically transfer of hydrogen from N1 is preferred in the gas phase (see Figure 2.3). Simple loss of intact uracil from m/z 216 leaves m/z 104, $[\text{Cu}(\text{HCCO})]^+$ and this fragmentation is calculated to be about 32 kJ mol^{-1} higher in Gibbs free energy than loss of ketene. The m/z 216 ion is also seen to undergo two other fragmentation processes, loss of CO and OCNCH_2 , leaving product ions at m/z 188 and 160, respectively. The isotopic labeling studies conclusively show that CO loss is exclusively from C4. Experimentally we cannot determine whether CO comes from the HCCO moiety or from the uracil ligand since both contain C4. However, loss of CO produces an ion which is 250 kJ mol^{-1} on the Gibbs free energy level diagram while loss of CO from HCCO, leaving a CH ligand, is 233 kJ mol^{-1} more costly in terms of Gibbs energy. The last fragmentation process to be discussed is that which forms m/z 160 from m/z 216. It is assumed that m/z 216 is Cu bound to a uracil and ketenyl ligand. The ^{13}C experiments show OCNCH_2 includes C2 (and therefore O2) from the uracil moiety which excludes a sequential loss of CO from m/z 216 followed by NCH_2 from m/z 188. As well, ^{15}N experiments show that N3 is lost from the uracil ligand. The deuterium isotope experiments show that the neutral fragment contains a deuterium when 5-d uracil is used; therefore C5 and H5 are included in the OCNCH_2 loss. It is proposed that this fragmentation involves an overall process by which the CH group from the HCCO ligand is somehow transferred to the OCNH group (O2, C2, and N3) of the uracil ligand resulting in loss of OCNCH_2 neutral and the m/z 160 ion depicted in Figures 2.6 and 2.7. Thermochemically, the processes leading to m/z 160 and m/z 188 are significantly lower on the Gibbs free energy diagram, 327.6 and $250.2 \text{ kJ mol}^{-1}$ compared to $374.6 \text{ kJ mol}^{-1}$

for the major loss, forming ketene. In order for the m/z 160 and m/z 188 fragmentation processes to be competitive with the other two, there must be significant energy barriers between them and the parent ion, m/z 216. This is reasonable since to form both suggested products from m/z 216 significant reorganization of the structure is required.

The processes by which the m/z 174 ion fragment-by losing HNCO, NCO or CO- has been discussed in detail previously.¹

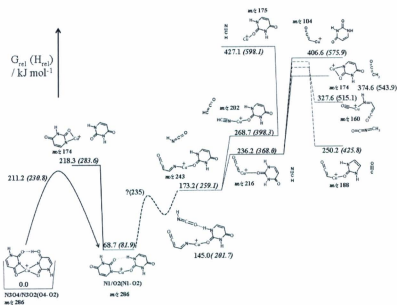


Figure 2.7: The proposed neutral fragments with origin in a lowest energy structure $[Cu(Ura-H)(Ura)]^+$. Relative Gibbs energy level diagram with respect to the lowest energy structure are in kJ/mol

2.4. Conclusions

Electrospray FTICR mass spectrometry of Cu^{2+} /uracil solutions show that the major ion observed is $[\text{Cu}(\text{Ura-H})(\text{Ura})]^+$. Unexpectedly, under SORI-CID and CO_2 laser-IRMPD conditions, these ions did not lose neutral uracil, but HNCO, as the primary fragmentation route. SORI-CID experiments conducted with 2- ^{13}C , 3- ^{15}N , 1,3- ^{15}N , 5-d, and 6-d, isotopically labeled uracil revealed that HNCO loss involves the nitrogen and carbon from the 3- and 2- position, respectively, and coupled with MS^n experiments this allowed for a detailed fragmentation scheme to be suggested. Computational chemistry results on the structures and energies of the ionic and neutral fragments were used as an aid to develop the fragmentation scheme. The experimental and theoretical results are shown to be consistent with the proposed mechanisms for dissociation and it is shown that loss of HNCO is simply more facile than simple loss of uracil from $[\text{Cu}(\text{Ura-H})(\text{Ura})]^+$. Twenty-seven different isomeric $[\text{Cu}(\text{Ura-H})(\text{Ura})]^+$ structures were found and are presented. The proposed fragmentation scheme involves extensive isomerization of the lowest-energy $[\text{Cu}(\text{Ura-H})(\text{Ura})]^+$ structure.

2.5 Acknowledgments

The authors wish to thank C.D. Poulter for generously sharing samples of 1, 3- ^{15}N -Uracil and 3- ^{15}N -Uracil which were used in this work. NSERC is graciously acknowledged for funding this work and the Atlantic Computational Excellence Network (ACENet) is thanked for the seemingly endless computational resources.

2.6 References

- (1) Lamsabhi, A.; Alcamí, M.; Otilia, M.; Yanez, M.; Tortajada, J.; Salpin, J.-Y. *ChemPhysChem*. **2007**, *8*, 181.
- (2) Deng, H.; Kebarle, P. *J. Am. Chem. Soc.* **1998**, *120*, 2925.
- (3) Chaparro, A. L.; Vachet, R. W. *J. Mass. Spectrom.* **2003**, *38*, 333.
- (4) Mourik, T. V.; Benoit, D. M.; Price, S. L.; Clary, D. C. *Phys. Chem. Phys. Chem.* **2000**, *2*, 1281.
- (5) Gu, J.; Leszczynski, J. *J. Phys. Chem. A*. **2001**, *105*, 10366.
- (6) Cerda, B. A.; Wesdemiotis, C. *J. Am. Chem. Soc.* **1996**, *118*, 11884.
- (7) Russo, N.; Toscano, M.; Grand, A. *J. Phys. Chem. B*. **2001**, *105*, 4735.
- (8) Russo, N.; Toscano, M.; Grand, A. *J. Am. Chem. Soc.* **2001**, *123*, 10272.
- (9) Yang, Z.; Rodgers, M. T. *Int. J. Mass Spectrom.* **2005**, *241*, 225.
- (10) Reddy, A. S.; Sastry, G. N. *J. Phys. Chem. A*. **2005**, *109*, 8893.
- (11) Tsierkezos, N. G.; Schroder, D.; Schwarz, H. *Int. J. Mass Spectrom.* **2004**, *235*, 33.
- (12) Nicholas, I.; Castro, M. *J. Phys. Chem. A*. **2006**, *110*, 4564.
- (13) Chandra, A. K.; Nguyen, M. T.; Uchimaru, T.; Zeegers-Huyskens, T. *J. Phys. Chem. A*. **1999**, *103*, 8853.
- (14) Eichhorn, G. C. *Nature*. **1962**, *194*, 474.
- (15) Foster, W.; Bauer, E.; Schutz, H.; Berg, H.; Akimenko, M.; Minchenkova, L.-E.; Evdkimov, Y. M.; Vershavsky, Y. M. *Biopolymer*. **1972**, *18*, 625.
- (16) Burkitt, M. *J. Meth Enzymol.* **1994**, *234*, 66.
- (17) Bal, W.; Kaprzak, K. S. *Toxicol letter*. **2002**, *127*, 55.

- (18) Halliwell, B.; Gutteridge, J. M. C. *Arch Biochem Biophys Acta*. **1986**, *1271*, 501.
- (19) Guillaumont, S.; Tortajada, J.; Salpin, J.-Y.; Lamsabhi, A. M. *Int.J.Mass Spectrom.* **2005**, *243*, 279.
- (20) Gutle, C.; Salpin, J.-Y.; Cartailier, T.; Tortajada, J.; Gaigeot, M.-P. *J.Phys.Chem.A*. **2006**, *110*, 11684.
- (21) Kabelac, M.; Hobza, P. *J.Phys.Chem.B*. **2006**, *110*, 14515.
- (22) Salpin, J.-Y.; Guillaumont, S.; Tortajada, J.; Lamsabhi, A. *J.Am.Soc.Mass Spectrom.* **2009**, *20*, 359.
- (23) Ali, O. Y.; Fridgen, T. D. *Int. J. Mass Spectrom.* **2011**, doi:10.1016/j.ijms.2011.4.3
- (24) Gillis, E. A. L.; Rajabi, K.; Fridgen, T. D. *J. Phys. Chem. A*. **2009**, *113*, 824.
- (25) Gillis, E. A. L.; Fridgen, T. D. *Int. J. Mass Spectrom.* **2010**, *297*, 2.
- (26) Elizabeth, R.; Manuel, Y.; Alejandro, T.-L.; Otilia, M. *Phy.Chem.Chem.Phys.* **2007**, *9*, 2531.
- (27) Lamsabhi, A.; Alcamí, M.; Otilia, M.; Yanez, M.; Tortajada, J. *J.Phys.Chem.A*. **2006**, *110*, 1943.
- (28) Rajabi, K.; Theel, K.; Gillis, E. A. L.; Beran, G.; Fridgen, T. D. *J. Phys. Chem. A*. **2009**, *113*, 8099.
- (29) Frisch, M. J. T., G. W.; Schlegel, H. B.; Scuseria, G. E.; Robb, M. A.; Cheeseman, J. R.; Montgomery, J. A., Jr.; Vreven, T.; Kudin, K. N.; Burant, J. C.; Millam, J. M.; Iyengar, S. S.; Tomasi, J.; Barone, V.; Mennucci, B.; Cossi, M.; Scalmani, G.; Rega, N.; Petersson, G. A.; Nakatsuji, H.; Hada, M.; Ehara, M.; Toyota, K.; Fukuda, R.; Hasegawa, J.; Ishida, M.; Nakajima, T.; Honda, Y.; Kitao, O.; Nakai, H.; Klene, M.; Li, X.; Knox, J.

E.; Hratchian, H. P.; Cross, J. B.; Adamo, C.; Jaramillo, J.; Gomperts, R.; Stratmann, R. E.; Yazyev, O.; Austin, A. J.; Cammi, R.; Pomelli, C.; Ochterski, J. W.; Ayala, P. Y.; Morokuma, K.; Voth, G. A.; Salvador, P.; Dannenberg, J. J.; Zakrzewski, V. G.; Dapprich, S.; Daniels, A. D.; Strain, M. C.; Farkas, O.; Malick, D. K.; Rabuck, A. D.; Raghavachari, K.; Foresman, J. B.; Ortiz, J. V.; Cui, Q.; Baboul, A. G.; Clifford, S.; Cioslowski, J.; Stefanov, B. B.; Liu, G.; Liashenko, A.; Piskorz, P.; Komaromi, I.; Martin, R. L.; Fox, D. J.; Keith, T.; Al-Laham, M. A.; Peng, C. Y.; Nanayakkara, A.; Challacombe, M.; Gill, P. M. W.; Johnson, B.; Chen, W.; Wong, M. W.; Gonzalez, C.; Pople, J. A. Gaussian 09 ed.; Gaussian, Inc.: Wallingford, 2008.

(30) Rajabi, K.; Easterling, M. L.; Fridgen, T. D. *J. Am. Soc. Mass Spectrom.* **2009**, *20*, 411.

(31) Rajabi, K.; Gillis, E. A. L.; Fridgen, T. D. *J. Phys. Chem. A* **2010**, *114*, 3449.

(32) Kurinovich, M. A.; Lee, J. K. *J. Am. Chem. Soc.* **2000**, *122*, 6258.

(33) Bensaude, O.; Aubard, J.; Dreyfus, M.; Dodin, G.; Dubois, J. E. *J. Am. Chem. Soc.* **1978**, *100*, 2823.

(34) Chang, K. C.; Grundwald, E. *J. Am. Chem. Soc.* **1976**, *98*, 3737.

(35) Lippert, B. *J. Raman Spectrosc.* **1979**, *8*, 274.

Chapter 3

Fragmentation Pathways of Gas Phase

$[M(\text{Uracil-H})(\text{Uracil})]^+$ Complexes (M= Zn, Cu, Ni, Co, Fe, Mn, Cd, Pd, Mg, Ca, Sr, Ba, and Pb)

3.1. Introduction

Since the discovery of the double helix structure (DNA),¹ many scientific studies have been performed on DNA to explore in more detail its structure and biochemistry.^{2,3} Metal ions, especially divalent metal ions, play an essential role in the process of RNA folding, structure stabilization, and their biochemical activity.⁴⁻⁶ Furthermore, metal ions contribute to the formation and stabilization of DNA molecules by interacting with phosphate groups to neutralize their negative charges. Different divalent transition metal ions have different effects on the structure of DNA. Consequently, the presence of metal ions with a subsequent nucleobase can affect the formation of their tautomers, which are involved in many biological processes.⁷

The gas phase reactions between divalent metal ions and nucleobases have been studied previously by using mass spectrometry and theoretical calculations. Many of those studies illustrate that the behavior of transition metal ions with DNA nucleobases is quite different than the behavior noted when using the divalent alkali earth metal ions. This dissimilarity in behavior may represent transition metals increased affinities toward

nucleobases.⁸ In particular, many studies have focused on the interactions of nucleobases, specifically uracil, thymine, and their derivatives, with different metal ions.⁹⁻¹³ Rincon et al.¹⁴ have determined computationally the effect of Ni^{2+} , Cu^{2+} , and Zn^{2+} on the diketo/keto-enol tautomerization of thymine. Findings from their study indicate that metal dications lead to stabilization of the keto-enol tautomer.

Uracil and thymine present many different tautomeric forms with hydrogen being attached to either the nitrogen or oxygen atoms.¹⁵⁻¹⁷ The gas phase reactivity of lead (II) ions with uracil and thymine has been studied using theoretical calculations, which focus on the structure of the $[\text{Pb}(\text{nucleobase})\text{-H}]^+$ ion.¹⁸ The most stable tautomer of $[\text{Pb}(\text{nucleobase})\text{-H}]^+$ ion in the gas phase is (2,4-dioxo), while the 2-hydroxy-4-oxo and 2-oxo-4-hydroxy tautomeric conformers are higher in energy than the 2,4-dioxo conformer.¹⁸ However, the energy differences between the structures are small, within 50 kJ mol^{-1} , which may favor a formation of a mixture of structures in the gas phase as opposed to one definite structure. The most stable tautomeric forms correspond to bicoordinated species, which involve the canonical form (2,4-dioxo) of uracil and thymine. Consequently, the global minimum structure is characterized by the interaction between the metal ion and both N3 and O4 atoms. In addition, the structures of complexes which involved a $[\text{Pb}(\text{Ura})\text{-H}]^+$ core have been studied by infrared multiple photon dissociation (IRMPD) spectroscopy in the gas phase.¹⁹ The finding results showed that all the complexes are deprotonated at N3 site where the lead bound to N3 and O4 and/or to N3 and O2 atoms. The results suggested the formation of a tautomeric form in which the lead interacts with N1 and O2 is not a significant to the electrosprayed

complexes.

The structures and relative stabilities of complexes of uracil and the interactions of uracil derivatives with different dications have been investigated.²⁰⁻²² It has been found that dications such as Cu^{2+} , Ni^{2+} , and Pb^{2+} complex with a nucleobase, B, to form a monocation $[\text{M}(\text{B}-\text{H})]^+$ in the gas phase.^{18,23,24} In this case, the doubly charged metal ions can oxidize the base and assist in its deprotonation.^{25,26} Interactions involving alkali-earth metal dications such as Ca^{2+} with uracil and its thio-derivatives have also been studied using density functional theory (DFT) calculations.²⁷ For uracil and 2,4-dithiouracil, Ca^{2+} attaches at position 4. However, Ca^{2+} prefers to attach to the oxygen atom rather than sulfur in 2-thiouracil and 4-thiouracil. This observable preference of attachment can be explained by the presence of electron delocalization that occurs when the metal binds to position 4 and to the oxygen rather than sulfur.

Many theoretical studies have been carried out focusing on the interaction between nucleobases and metal ions, but experimental studies are scarce. An example of these is the manganese ion affinities which are studied with different nucleobases by using DFT. Pyrimidine bases contain many different binding sites which include mono-coordination on oxygen and nitrogen, and bi-coordination on N and O or N and N atoms. Mn^{2+} ideally forms bi-coordination complexes with uracil and thymine and it binds between N3 and O4 to form the global minimum-energy structure.²⁸ Zinc is one of the most abundant transition metals which is found in cytoplasm, and has a role in regulating genes.^{29,30} Marino et al.³¹ studied the interaction between zinc ion with purine and pyrimidine bases in the gas phase also using DFT calculations. In the thymine and uracil cases, the lowest

energy complexes are bi-coordination, rather than mono-coordination, in which Zn^{2+} is ligated by N3 and the adjacent oxygen atom O4.

This work focuses on determining the primary fragmentation patterns of $[M(Ura-H)(Ura)]^+$ ions using SORI-CID and infrared multiple photon dissociation (IRMPD) as the sources of excitation. Our previous work revealed that fragmentation of $[Cu(Ura-H)(Ura)]^+$ complexes under similar conditions did not result in the direct loss of uracil. The purpose of the present study is to explore the differences in the primary fragmentation of $[M(Ura-H)(Ura)]^+$ for other +2 metal ions. The explanation of the experimental results are aided by computationally examining the structures and energetics of the $[M(Ura-H)(Ura)]^+$ complexes.

3.2. Method

3.2.1. Experimental

All experiments were recorded on a Bruker ApexQe hybrid quadrupole-Fourier transform ion cyclotron resonance (FT-ICR) mass spectrometer. All the chemicals were used without any further purification. Uracil was purchased from Sigma-Aldrich Company. The following inorganic salts were used: zinc chloride (99% Fluka), copper(II) chloride (99% Aldrich), nickel(II) chloride (>98% Sigma-Aldrich), cobalt(II) nitrate (>98% Sigma-Aldrich), iron(II) chloride (>98%,Fluka), Manganese(II) chloride (>99% Aldrich), cadmium(II) nitrate(98% Aldrich), palladium(II) chloride(99% Aldrich), magnesium sulfate (>98% Sigma-Aldrich), calcium chloride(99% Sigma-Aldrich), Strontium Chloride (99% Sigma-Aldrich), barium chloride(99% Sigma-Aldrich), lead(II) nitrate(>99% Fluka-Chemika).

Samples for the experiments were prepared by adding a few drops of 1 mM of an inorganic salt solution to 10 mL of 1mM uracil in 18 M Ω water (Millipore). All the samples were sprayed at 100 μ L/hr into an Apollo II ion source coupled to a Bruker ApexQe 7 tesla (FTICR) mass spectrometer. The desired [M(Ura-H)(Ura)]⁺ precursor ions were mass selected in the quadrupole mass filter and then allowed to accumulate for 2-3 s before being transferred to the ICR cell. Collision induced dissociation (CID) experiments were conducted by first isolating the isotopomer of [M(Ura-H)(Ura)]⁺ with the highest intensity and accelerating those ions into argon gas (pressure $\sim 10^{-8}$ torr) under sustained off-resonance irradiation (SORI) conditions.³² SORI-CID experiments were performed by applying maximum laboratory-frame collisional kinetic energies between 3.2-11.4 eV corresponding to ($V_{p,p}$ 1.82-3.44 V) or center-of-mass kinetic energies of 0.39-1.4 eV. In all experiments, SORI was conducted during 250 ms pulse then followed by a 2 s delay to pump neutral argon from the ICR cell prior to detection. In addition, softer activation of the parent ions was done using IRMPD. IRMPD was performed using 25 W continuous CO₂ laser (10.6 μ m wavelength) operating at 80% of maximum power. Short IR pulse lengths, typically, 0.1-0.4 s were applied.

3.2.2. Computational

The Gaussian 09 program was used for all the calculations.³³ All geometry optimizations were carried out using the B3LYP density functional method and 6-31+G(d,p) basis set on C, H, N, O atoms and all the metals except Cd, Pd, Sr, Ba, and Pb. For more accurate energies single point calculations were performed on the B3LYP/6-31+G(d,p) geometries using B3LYP/6-311++G(2df,2p) on C, H, N, and O and 6-311+G

on Zn, Cu, Ni, Fe, Mg, and Ca, were used. This procedure is denoted as B3LYP/6-311+G(2df,2p)//B3LYP/6-31+G(d,p). Also, calculations on all species were carried out using the same basis set for C, H, N, and O but for all the divalent metal ions, the LANL2DZ basis set was used.

To gain further insight into these structures $[M(\text{Ura-H})(\text{Ura})]^+$, the binding energies were examined. For this purpose, the binding energies between neutral uracil and $[M(\text{Ura-H})]^+$, $M = \text{Zn, Cu, Ni, Fe, Cd, Pd, Mg, Ca, Sr Ba, and Pb}$ were determined.

3.3. Results and Discussions

Our previous studies³⁴ showed that copper (II) ions react with uracil to form complexes of the Cu(II), deprotonated uracil and uracil, a singly charged species. $[\text{Cu}(\text{Ura-H})(\text{Ura})]^+$ was the most abundant species formed by the interaction between the Cu^{2+} ion and uracil. These distinct complexes have been investigated by using MS/MS experiments in combination with theoretical calculations to determine the mechanism for the extensive fragmentation that was observed. The MS/MS spectra of $[\text{Cu}(\text{Ura-H})(\text{Ura})]^+$ complex ($m/z = 286$) showed that the main ion dissociates by elimination of 43 Da followed by 27 Da which correspond to the loss of HNCO, and HCN, respectively, and not the direct loss of uracil. Extensive labelling experiments were also found to be quite useful in determining the details of the fragmentation reactions.

In this present chapter the fragmentation reactions of $[M(\text{Ura-H})(\text{Ura})]^+$ complexes were investigated using various divalent metals. Results obtained indicated that all of the mass spectra of M^{2+} /uracil samples reveal positive ions due to the presence of complexes of $[M(\text{Ura-H})(\text{Ura})]^+$, specifically at $m/z = 287, 286, 281, 282, 279, 278, 337, 329, 247,$

263, 311, 361 and 431 which correspond to $[M(\text{Ura-H})(\text{Ura})]^+$ complexes containing Zn, Cu, Ni, Co, Fe, Mn, Cd, Pd, Mg, Ca, Sr, Ba and Pb, respectively. In all cases, the isotopic signature of the different complexes was used to confirm the identity of these complexes as $[M(\text{Ura-H})(\text{Ura})]^+$.

3.3.1 SORI/CID spectra of $[M(\text{Ura-H})(\text{Ura})]^+$

Under SORI conditions, various fragmentation patterns were observed for the $[M(\text{Ura})(\text{Ura-H})]^+$ ions. Examination of Figure 3.1(A, B, and C) shows that $[M(\text{Ura-H})(\text{Ura})]^+$ exhibits a specific dissociation pattern. The primary fragmentation pathway for $[M(\text{Ura})(\text{Ura-H})]^+$ ions ($M = \text{Zn, Cu, Ni, Co, Fe, Mn, Cd, Pd, and Mg}$) is loss of 43 Da corresponding to loss of HNC. This fragment has been shown to result from the cleavage C2 and N3 atoms which is confirmed by using isotopic labeling of uracils in $[\text{Cu}(\text{Ura-H})(\text{Ura})]^+$.³⁴ These results also suggest a similar fragmentation pattern as the $[\text{Cu}(\text{Ura-H})(\text{Ura})]^+$ complex system which has been discussed previously. They also indicate that the divalent metals are strongly associated with uracil and are capable of forming a strongly-bound cluster such that cleavage of the uracil ring is preferable over scission of the metal-uracil bonds.

MS/MS spectra of the $[M(\text{Ura-H})(\text{Ura})]^+$ ions ($M = \text{Ca, Sr, Ba, and Pb}$) yield quite different results under the same experimental conditions, as seen in Figure 3.1C. These complexes dissociate losing 112 Da which most likely involves the elimination of the intact uracil.

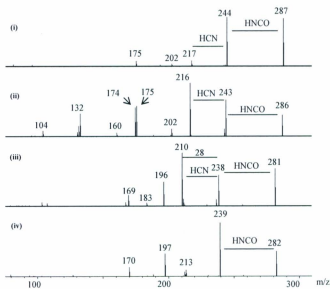


Figure 3.1 A: SORI/CID spectra of the $[M(\text{Ura-H})(\text{Ura})]^+$ complex obtained with (i) $[\text{Zn}(\text{Ura-H})(\text{Ura})]^+$, (ii) $[\text{Cu}(\text{Ura-H})(\text{Ura})]^+$, (iii) $[\text{Ni}(\text{Ura-H})(\text{Ura})]^+$ and (iv) $[\text{Co}(\text{Ura-H})(\text{Ura})]^+$ recorded with a SORI power 0.656 eV

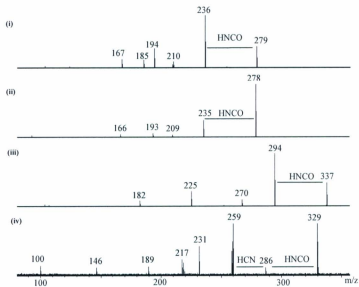


Figure 3.1 B: SORI/CID spectra of the $[M(\text{Ura-H})(\text{Ura})]^+$ complex obtained with (i) $[\text{Fe}(\text{Ura-H})(\text{Ura})]^+$, (ii) $[\text{Mn}(\text{Ura-H})(\text{Ura})]^+$, (iii) $[\text{Cd}(\text{Ura-H})(\text{Ura})]^+$ and (iv) $[\text{Pd}(\text{Ura-H})(\text{Ura})]^+$ recorded with a SORI power 0.656 eV.

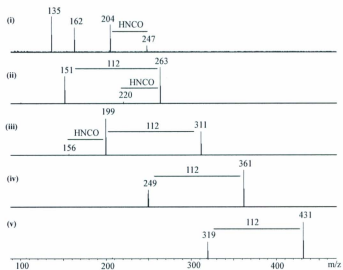


Figure 3.1 C: SORI/CID spectra of the $[M(\text{Ura-H})(\text{Ura})]^+$ complex obtained with (i) $[\text{Mg}(\text{Ura-H})(\text{Ura})]^+$, (ii) $[\text{Ca}(\text{Ura-H})(\text{Ura})]^+$, (iii) $[\text{Sr}(\text{Ura-H})(\text{Ura})]^+$, (iv) $[\text{Ba}(\text{Ura-H})(\text{Ura})]^+$, (v) $[\text{Pb}(\text{Ura-H})(\text{Ura})]^+$ recorded with a SORI power 0.656 eV.

3.3.2 IRMPD dissociation of $[M(\text{Ura-H})(\text{Ura})]^+$

IRMPD can also be useful for characterization of uracil-metal complexes. In IRMPD the excitation process can be softer, however, fragments can themselves absorb photons from the laser and dissociate. The IRMPD spectra revealed similar results as those obtained when using the SORI-CID. The main fragmentation observed was due to a loss of 43 Da corresponding to HNCO loss in the complexes $[M(\text{Ura-H})(\text{Ura})]^+$ ($M = \text{Zn}, \text{Cu}, \text{Ni}, \text{Co}, \text{Fe}, \text{Mn}, \text{Cd}, \text{Mg}, \text{Ca}$) while in the complexes $[M(\text{Ura-H})(\text{Ura})]^+$ ($M = \text{Sr}, \text{Ba}, \text{and Pb}$) the intact uracil was observed as a primary fragment, as seen in Appendices (12-14). The most noteworthy difference between the IRMPD experiments and the CID experiments was observed with $[\text{Ca}(\text{Ura-H})(\text{Ura})]^+$, as seen in Figure 3.2. When using the softer IRMPD excitation, $[\text{Ca}(\text{Ura-H})(\text{Ura})]^+$ loses HNCO, however, under SORI-CID conditions uracil loss was observed. This means that HNCO loss and uracil loss are competitive as the primary fragmentation route for $[\text{Ca}(\text{Ura-H})(\text{Ura})]^+$. This competition is interesting and will be discussed further.

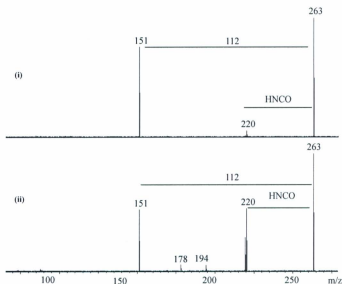


Figure 3.2: (i) SORI/CID spectrum of the $[\text{Ca}(\text{Ura-H})(\text{Ura})]^+$ complex obtained with a SORI power 0.656 eV, (ii) IRMPD spectrum of the $[\text{Ca}(\text{Ura-H})(\text{Ura})]^+$ complex.

Loss of HNCO occurs through a tight transition state whereas loss of uracil occurs through a loose transition state, in fact there is unlikely to be a barrier for loss of uracil besides the bond dissociation energy. Considering a situation such as that depicted in Figure 3.3, HNCO loss as a lower activation energy, but due to the tightness of the transition state, it has a small pre-exponential factor. On the other hand, simple loss of uracil is characterized by a higher activation energy and due the looseness of the reaction, a large pre-exponential factor. In the SORI-CID experiments a maximum of 50 kJ mol^{-1} of energy is deposited into the complex per collision whereas in IRMPD, the energy per photon is approximately 10 kJ mol^{-1} ($\sim 1000 \text{ cm}^{-1}$ for the CO_2 laser). In SORI-CID, then,

significantly more energy can be deposited per collision and the internal energy of the ion rapidly exceeds the threshold for both uracil and HNCO loss, but where the rate constant for uracil loss is greater than that for HNCO loss. In the IRMPD experiments, the excitation process is slower and the average internal energy of the ions observed dissociating must be in the range where the rate constant for uracil loss is significantly less than the rate constant for HNCO loss.

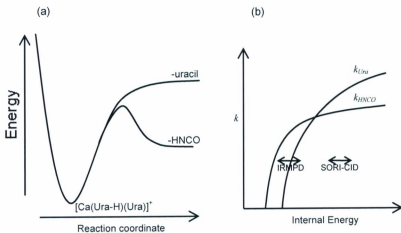
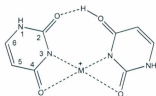


Figure 3.3: (a) Proposed energy profile for loss of HNCO and uracil from $[\text{Ca}(\text{Ura-H})(\text{Ura})]^+$ and (b) a rate constant vs internal energy scheme corresponding to the proposed energy profile in (a).

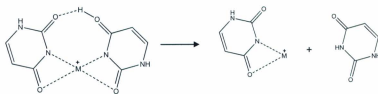
3.4. Computational study

In order to rationalize the experimental findings, we have used theoretical calculations to explore the effect of the metal binding energy and describe the attachment of the metal to the most stable dimer complexes $[M(\text{Ura-H})(\text{Ura})]^+$ ($M = \text{Zn, Cu, Ni, Fe, Cd, Pd, Mg, Ca, Sr, Ba, and Pb}$). The lowest energy $[M(\text{Ura-H})(\text{Ura})]^+$ structures all adopt a geometry represented by Scheme 3.1. The metal ion is ligated by N3 and O4 of the deprotonated uracil and to N3 and O2 of the intact uracil in its O4 tautomer. These complexes are also characterized by a hydrogen bond between O4H on of the intact uracil and O2 on the deprotonated uracil. The attachment of M^{2+} to the two oxygen atoms and the N atoms of uracils lead to the most stable isomer which forms tetra coordinated complexes. These isomers coincide with previous theoretical calculations carried out at the B3LYP level for copper complexes.³⁴ The lowest energy structures for most of the $[M(\text{Ura-H})(\text{Ura})]^+$ complexes are characterized by a metal ion which lies in the same plane as the uracils (square planar). When M is Ba or Pb the geometry around the metal ion was found to be square pyramidal. The Ni and Fe complexes are interesting as two different geometries might be expected depending on the electronic states, singlet or triplet. The results obtained indicate that for Fe, the singlet, tetrahedral geometry is more favorable by between 20-50 kJ mol^{-1} (depending on the level of theory, Table 3.1) than the square planar. For Ni, on the other hand, the triplet, square planar geometry is more favorable by 50-60 kJ mol^{-1} .



Scheme 3.1: The lowest energy possible structures for the $[M(\text{Ura})(\text{Ura-H})]^+$; $M = \text{Mg}, \text{Ca}, \text{Ba}, \text{Pb}, \text{Fe}, \text{Ni}, \text{Cu}, \text{Zn}, \text{and Cd}$.

The computed binding energies between neutral uracil and $[M(\text{Ura-H})]^+$ ($M = \text{Zn}, \text{Cu}, \text{Ni}, \text{Fe}, \text{Cd}, \text{Pd}, \text{Mg}, \text{Ca}, \text{Sr}, \text{Ba}, \text{and Pb}$ (Scheme 3.2) have been calculated and are presented in Table 3.1. The binding energies have been calculated by using two different basis sets because the size of Cd, Pd, Sr, Ba and Pb metals makes it impractical and impossible to use the all electron 6-31+G basis set for these metals. The LANL2DZ basis set is used to compare the binding energies of all the metals. While there are expectedly minor differences in the binding enthalpies computed using the two methods, they are in general agreement in the energy ordering. For example, the four complexes with the highest binding enthalpies rank in the order $\text{Ni} > \text{Fe} > \text{Mg} > \text{Zn}$ using the all-electron basis sets, the order changes to $\text{Ni} > \text{Mg} > \text{Fe} > \text{Zn}$. The differences between the Fe and Mg binding enthalpies are only slightly more than 10 kJ mol^{-1} using both calculation methods. A flip-flop in ordering also seen between Cu and Ca but in this case the computed differences in binding enthalpies are less than 10 kJ mol^{-1} by both methods.



Scheme 3.2: The computed binding energy between neutral uracil and $[M(\text{Ura-H})]^+$
 $M = \text{Mg, Ca, Ba, Pb, Fe, Ni, Cu, Zn, and Cd}$.

To determine the geometry of transition metal complexes, the degree of splitting of the d orbitals is important and determines how orbitals are filled. Metals, such as Mn and Co, are capable of filling their orbitals in a number of ways and this makes it difficult to attempt to calculate all their possible electronic geometries. Therefore, in this paper the geometries of Mn and Co were not calculated.

As seen above, the SORI-CID decomposition of the Ca^{2+} , Sr^{2+} , Ba^{2+} and Pb^{2+} complexes with uracil show a quite different primary fragmentation when compared with the other systems. For these four complexes the SORI-CID process leads to the loss of neutral uracil. In contrast, the primary fragmentation of all other complexes involves the loss of HNCO, fragmentation of the (Ura-H) ligand. Our previous calculations show that the loss of HNCO from the lowest energy complex of $[\text{Cu}(\text{Ura-H})(\text{Ura})]^+$ ³⁴ requires approximately 259 kJ mol^{-1} whereas loss of uracil requires 284 kJ mol^{-1} . We were unable to locate a transition state for HNCO loss from $[\text{Cu}(\text{Ura-H})(\text{Ura})]^+$ despite valiant efforts. An enthalpy barrier for HNCO loss from $[\text{Cu}(\text{Ura-H})]^+$ was found³⁵ to be about 235 kJ mol^{-1} which is lower in energy than complete loss of HNCO (259 kJ mol^{-1}). It is

suggested that there is a similar energy barrier to loss of HNCO from $[\text{Cu}(\text{Ura-H})(\text{Ura})]^+$ which perhaps connects to an intermediate hydrogen-bound complex which was determined to have a relative enthalpy of 202 kJ mol^{-1} , as seen in Figure 2.7.

The difference in behavior between $[\text{M}(\text{Ura-H})(\text{Ura})]^+$ complexes when ($\text{M} = \text{Zn}, \text{Cu}, \text{Ni}, \text{Fe}, \text{Cd}, \text{Pd}, \text{Mg}, \text{and Ca}$) and when $\text{M} = \text{Sr}, \text{Ba}, \text{and Pb}$) can be explained, in part, in terms of the differences between the uracil binding energies. The computed enthalpies for loss of uracil from $[\text{M}(\text{Ura-H})(\text{Ura})]^+$, when $\text{M} = \text{Sr}, \text{Ba}, \text{and Pb}$, are $237.9, 214.9$ and 175 kJ mol^{-1} respectively. In contrast, the computed uracil binding enthalpies for all other metals are greater than or equal to 286 kJ mol^{-1} . For comparison, the enthalpy requirement for HNCO loss from $[\text{Cu}(\text{Ura-H})(\text{Ura})]^+$ is 259 kJ mol^{-1} . While the energy requirement for loss of HNCO will differ for each complex, this work provides an explanation for why HNCO loss occurs predominantly for the $[\text{M}(\text{Ura-H})(\text{Ura})]^+$ complexes except for Sr, Ba, and Pb.

The uracil binding energy for $[\text{Ca}(\text{Ura-H})(\text{Ura})]^+$ is calculated to be slightly higher than for $[\text{Cu}(\text{Ura-H})(\text{Ura})]^+$. In this case, that IRMPD excitation promotes HNCO loss we have established that this fragmentation route has a lower energy requirement than loss of uracil but the energy requirements for the two fragmentation pathways are similar. While $[\text{Ca}(\text{Ura-H})(\text{Ura})]^+$ is an interesting example, it is still consistent with having a higher uracil binding energy than the energy required to lose HNCO.

Metal	B3LYP/6-31+G(d,p)// B3LYP/6-311+G(2df,2p)		B3LYP/6-31+G(d,p)// B3LYP/6-311+G(2df,2p) (LANL2DZ on all M)	
	ΔH	ΔG (kJ/mol)	ΔH	ΔG
Ni (sq)	368.3	304.2	356.8	294.5
Ni (tet)	298.8	240.6	296.3	238.4
Mg	341.6	285.1	342.9	286.8
Fe (tet)	351.1	289.7	329.0	271.8
Fe (sq)	309.3	247.8	307.1	246.1
Zn	323.3	268.5	314.4	260.4
Pd (sq)	--	--	312.3	254.1
Ca	275.4	220.8	294.9	240.3
Cu	283.6	218.3	290.4	227.9
Cd	--	--	286.0	229.9
Sr	--	--	237.9	190.3
Ba	--	--	214.9	155.1
Pb	--	--	175.1	120.9

Sq: square planar; tet: tetrahedral.

Table 3.1: The computed binding enthalpies and Gibbs energies (kJ mol^{-1}) between uracil and $[\text{M}(\text{Ura-H})]^+$ complexes (see Scheme 3.2) as determined by electronic structure calculations.

The uracil binding energies should correlate with the size of the metal ion for an ion-dipole complex; the smaller the metal ion, the stronger the ion-dipole complex or, specifically the $[M(\text{Ura-H})]^+-\text{Ura}$ complex. Figure 3.4 is a plot of the computed uracil binding energies vs. the effective ionic radius of the M^{2+} ion.³⁶ The correlation is not perfect, which is expected since there may also be some degree of covalent bonding, but the trend is generally as expected. What is even more interesting is that the ions with the three largest radii (and lowest uracil binding energy) are the three ions which predominantly lose uracil on SORI and IRMPD activation. The ions with the smallest ionic radii lose HNCO. Ca^{2+} has an intermediate effective ionic radii, 100 pm, and it is the ion which is shown experimentally to switch depending on the activation process. The predominant oxidation state for mercury is also +2, however, after many attempts we were unable to electrospray a sufficient intensity of $[\text{Hg}(\text{Ura-H})(\text{Ura})]^+$ -no $[\text{Hg}(\text{Ura-H})]^+$ either-to perform IRMPD or SORI activation experiments. The effective ionic radius of Hg^{2+} is slightly larger than Ca^{2+} at 102 pm. Based on the results presented here, it is expected that $[\text{Hg}(\text{Ura-H})(\text{Ura})]^+$ would lose uracil at least under IRMPD conditions.

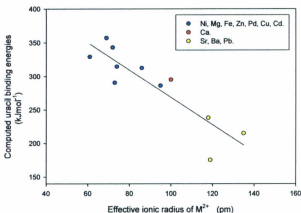


Figure 3.4: A plot between the computed uracil binding energies vs. the effective ionic radius of the M^{2+} ion

3.5. Conclusions

Mass spectrometry reveals that electrospray of aqueous solutions containing uracil and divalent metal ions readily produce $[M(\text{Ura-H})(\text{Ura})]^+$ complexes. In this study, we have investigated the fragmentation reactions of these $[M(\text{Ura-H})(\text{Ura})]^+$ complexes composed of various metals, M. Both SORI/CID and IRMPD activation when $M = \text{Zn}, \text{Cu}, \text{Ni}, \text{Co}, \text{Fe}, \text{Mn}, \text{Cd}, \text{Pd}, \text{Mg}$, results predominantly in loss of HNCO as the major primary fragmentation route. In contrast, when $M = \text{Sr}, \text{Ba}$, and Pb the sole fragmentation pathway corresponded to loss of uracil for both SORI and IRMPD activation. These differences in fragmentation products are explained by looking at the characteristics of the binding energies of the complexes and/or the effective ionic radius of the metal dication. The computed binding energies between uracil and $[M(\text{Ura-H})]^+$ were computed

and the uracil binding energies generally correlate inversely to the ionic radii of the metal ions. The computed uracil binding energies for $[M(\text{Ura-H})(\text{Ura})]^+$ when M^{2+} is a large dication (Sr, Ba, and Pb,) are substantially lower than the binding energies of all other $[M(\text{Ura-H})(\text{Ura})]^+$ complexes and lose uracil as their sole decomposition pathway. When M^{2+} is a small dication the uracil binding energies are much larger and the major decomposition pathway is loss of HNCO. That the binding energy between uracil and $[M(\text{Ura-H})]^+$ correlates with the size of the metal dication suggests that binding in the $[M(\text{Ura-H})(\text{Ura})]^+$ complex is predominantly an ion-dipole complex between $[M(\text{Ura-H})]^+$ and uracil.

Interestingly the uracil binding energy of $[\text{Ca}(\text{Ura-H})]^+$ lies between the two extremes, the size of Ca^{2+} is intermediate, and $[\text{Ca}(\text{Ura-H})(\text{Ura})]^+$ is observed to decompose by loss of uracil under SORI activation conditions but loses HNCO under the softer IRMPD activation conditions. Qualitatively, it is assumed that the switch of fragmentation pathways is due to SORI being able to access higher internal energies of the complex where decomposition of uracil, characterized by a high activation energy and large pre-exponential factor, is faster. For IRMPD, characterized by smaller energy jumps accesses the fragmentation pathway which has the lowest activation energy, loss of HNCO.

3.6 References

- (1) Watson, J. D.; Crick, F. H. *Nature* **1953**, *171*, 737.
- (2) Franklin, R. E.; Gosling, R. G. *Nature*. **1953**, *171*, 740.
- (3) Wilkins, M. H. F.; Stokes, A. R.; Wilson, H. r. *Nature*. **1953**, *171*, 738.
- (4) Pyle, A. M. *Science*. **1993**, *261*, 709.
- (5) Misra, V. k.; Draper, D. E. *Biopolymers*. **1998**, *48*, 113.
- (6) Madore, E.; Florentz, C.; Giege, R.; Lapointe, J. *J. Nucleic Acids Res.* **1999**, *27*, 3583.
- (7) Burda, J. V.; Sponer, J.; Leszczynski, J.; Hobza, P. *J. Phys. Chem. B*. **1997**, *101*, 9670.
- (8) Sabat, M.; Lippert, B. *Metal Ions in Biological Systems*. **1996**, *33*, 143.
- (9) Zhu, W. L.; Luo, X. M.; Puah, C. M.; Tan, X. J.; Shen, J. H.; Gu, J. D.; Chen, K. X.; Jiang, H. L. *J. Phys. Chem. A*. **2004**, *108*, 4008.
- (10) Kufelnicki, A.; Kupinska, I.; Jezierska, J.; Ochocki, J. *Pol. J. Chem.* **2002**, *76*, 1559.
- (11) Kabelac, M.; Hobza, P. *J. Phys. Chem. B*. **2006**, *110*, 14515.
- (12) Nir, E.; Janzen, C.; Imhof, P.; Kleinermanns, K.; de Vries, M. S. *J. Chem. Phys.* **2001**, *115*, 4604.
- (13) Blas, J. R.; Luque, F. J.; Orozco, M. *J. Am. Chem. Soc.* **2004**, *126*, 154.
- (14) Rincon, E.; Yanez, M.; Toro-Labbe, A.; Mo, O. *Phys. Chem. Chem. Phys.* **2007**, *9*, 2531.
- (15) Piacenza, M.; Grimme, S. *J. Comput. Chem.* **2004**, *25*, 83.

- (16) Wolken, J. K.; Turecek, F. *J. Am. Soc. Mass Spectrom.* **2000**, *11*, 1065.
- (17) Kryachko, E. S.; Nguyen, M. T.; Zeegers-Huyskens, T. *J. Phys. Chem. A.* **2001**, *105*, 1288.
- (18) Guillaumont, S.; Tortajada, J.; Salpin, J.-Y.; Lamsabhi, M. *Int. J. Mass spectrom.* **2005**, *243*, 279.
- (19) Ali, O. Y.; Fridgen, T. D. *Int. J. Mass Spectrom.* doi:10.1016/j.ijms.2011.04.3.
- (20) Russo, N.; Toscano, M.; Grand, A. *J. Phys. Chem. A.* **2003**, *107*, 11533.
- (21) Reddy, A. S.; Sastry, G. N. *J. Phys. Chem. A.* **2005**, *109*, 8893.
- (22) Nicolas, I.; Castro, M. *J. Phys. Chem. A.* **2006**, *110*, 4564.
- (23) Lamsabhi, A. M.; Alcamí, M.; Mo, O.; Yanez, M.; Tortajada, J.; Salpin, J. Y. *ChemPhysChem.* **2007**, *8*, 181.
- (24) Tsierkezos, N. G.; Schroder, D.; Schwarz, H. *Int. J. Mass spectrom.* **2004**, *235*, 33.
- (25) Lamsabhi, A. M.; Mo, O.; Yanez, M.; Alcamí, M.; Tortajada, J. *ChemPhysChem.* **2004**, *5*, 1871.
- (26) Lamsabhi, A. M.; Alcamí, M.; Mo, O.; Yanez, M.; Tortajada, J. *J. Phys. Chem. A.* **2006**, *110*, 1943.
- (27) Trujillo, C.; Lamsabhi, A. M.; Mo, O.; Yanez, M.; Salpin, J. Y. *Org. Biomol. Chem.* **2008**, *6*, 3695.
- (28) Russo, N.; Toscano, M.; Grand, A. *Int. j. Quant chem.* **2002**, *90*, 903.
- (29) Berg, J. M.; Shi, Y. *Science.* **1996**, *271*, 1081.
- (30) Schwabe, J. W. R.; Klug, A. *Nat. Struct. Mol. Biol.* **1994**, *1*, 345.
- (31) Marino, T.; Mazzuca, D.; Toscano, M.; Russo, N.; Grand, A. *Int. j. Quant chem.*

2007, 107, 311.

(32) Gauthier, J. W.; Trautman, T. R.; Jacobson, D. B. *Anal Chim. Acta* **1991**, 246, 211.

(33) Frisch, M. J. T., G. W.; Schlegel, H. B.; Scuseria, G. E.; Robb, M. A.; Cheeseman, J. R.; Montgomery, J. A., Jr.; Vreven, T.; Kudin, K. N.; Burant, J. C.; Millam, J. M.; Iyengar, S. S.; Tomasi, J.; Barone, V.; Mennucci, B.; Cossi, M.; Scalmani, G.; Rega, N.; Petersson, G. A.; Nakatsuji, H.; Hada, M.; Ehara, M.; Toyota, K.; Fukuda, R.; Hasegawa, J.; Ishida, M.; Nakajima, T.; Honda, Y.; Kitao, O.; Nakai, H.; Klene, M.; Li, X.; Knox, J. E.; Hratchian, H. P.; Cross, J. B.; Adamo, C.; Jaramillo, J.; Gomperts, R.; Stratmann, R. E.; Yazyev, O.; Austin, A. J.; Cammi, R.; Pomelli, C.; Ochterski, J. W.; Ayala, P. Y.; Morokuma, K.; Voth, G. A.; Salvador, P.; Dannenberg, J. J.; Zakrzewski, V. G.; Dapprich, S.; Daniels, A. D.; Strain, M. C.; Farkas, O.; Malick, D. K.; Rabuck, A. D.; Raghavachari, K.; Foresman, J. B.; Ortiz, J. V.; Cui, Q.; Baboul, A. G.; Clifford, S.; Cioslowski, J.; Stefanov, B. B.; Liu, G.; Liashenko, A.; Piskorz, P.; Komaromi, I.; Martin, R. L.; Fox, D. J.; Keith, T.; Al-Laham, M. A.; Peng, C. Y.; Nanayakkara, A.; Challacombe, M.; Gill, P. M. W.; Johnson, B.; Chen, W.; Wong, M. W.; Gonzalez, C.; Pople, J. A. Gaussian 03, Gaussian, Inc.; Wallingford, CT, 2004.

(34) Ali, O. Y.; Fridgen, T. D. *Chem. Phys. Chem.* **2011**, *cphc.20110661*.

(35) Lamsabhi, A.; Alcamí, M.; Otilia, M.; Yanez, M.; Tortajada, J.; Salpin, J.-Y. *ChemPhysChem.* **2007**, 8, 181.

(36) http://en.wikipedia.org/wiki/Ionic_radius.

Chapter 4

Structures of Electrosprayed [Pb(Uracil-H)]⁺

Complexes by Infrared Multiple Photon

Dissociation Spectroscopy

4.1. Introduction *

The DNA molecule is responsible for a number of crucial roles in biology including the storage and transfer of genetic information. Noncovalent interactions play a fundamental role in many scientific fields and these interactions allow metal ions to influence essential biological processes such as those involving DNA.¹ Like many biological molecules, the structure and regular function of DNA can be impacted, positively or negatively, by the presence of other molecules and ions. A significant amount of research has been devoted to studying the impact that metal ions have on biological systems such as RNA folding, stabilization, and activity²⁻⁵ and have also shown the influential impact that metal ions have on biological molecules including their role in the nature and function of proteins, nucleic acids, and peptide hormones. Various

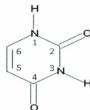
* This Chapter has been accepted to be published as O.Y.Ali and T.D.Fridgen, *Int. J. Mass Spectrom* 2011, 308, 167.

metal ions interact with DNA and consequently can manipulate its structure.⁶⁻¹¹ The affect that these ions have on DNA depends largely on their binding location¹² and can lead to, for example, stabilization or competition for hydrogen bonding. When metal ions bind with nucleic acid bases they interfere with hydrogen bond interactions between base pairs and provoke a subsequent disruption in the double helix.¹²⁻¹⁴ Depending on their nature, structural changes in DNA induced by the metal ion can have profound effects on the transfer of genetic information.

Lead is a common metal ion known to invoke a damaging effect on biological homeostasis.¹⁵ Therefore much literature has focused on its toxic effects on human health.^{15,16} These harmful effects impact many major organs including the liver, heart and kidneys.

Sigel and co-workers have published many interesting papers focusing on the interactions of Pb^{2+} ions in aqueous solution with phosphate, phosphonates,¹⁷ and nucleotides.^{18,19} On the other hand, other papers deal with the reactivity of Pb^{2+} with nucleobases in the gas phase.^{20,21} The reactivity of lead (II) ions with uracil and thymine has been investigated by mass spectrometry in the gas phase.²⁰ Positive-ion electrospray spectra showed that the doubly charged complexes dissociate to give a singly charged $[Pb(\text{nucleobase-H})]^+$ when the nucleobase was uracil or thymine. This singly charged ion is the most abundant complex observed in the electrospray mass spectra and was studied by MS/MS. $[Pb(\text{Ura-H})]^+$ and $[Pb(\text{Thy-H})]^+$ both dissociate by elimination of isocyanic acid (HNCO), and the formation of the $[PbNCO]^+$ ion. Salpin *et al.*²¹ have also studied the interactions between lead (II) and thiouracil derivatives (2-thiouracil, 4-thiouracil, and

2,4-dithiouracil) which also form $[\text{Pb}(\text{nucleobase}-\text{H})]^+$ ions (for numbering scheme for uracil see Scheme 4.1). MS/MS spectra were recorded at different collision energies revealing that the fragmentation of 2-thiouracil is different than 4-thiouracil. The 2-thiouracil complex loses predominantly PbS while both 4-thiouracil and 2,4-dithiouracil lose completely reduced Pb as the primary fragmentation route. The 2-thiouracil complex also loses HNCS while the 4-thiouracil complex loses HNCO. Even though the lowest energy structure in both has lead bound in a bidentate fashion to S and deprotonated N, a major fragmentation path, like in $[\text{Pb}(\text{Ura}-\text{H})]^+$ and $[\text{Pb}(\text{Thy}-\text{H})]^+$, involves breaking the N1-C2 bond and the N3-C4 bond.



Scheme 4.1: Numbering scheme for uracil.

It is important to determine ion structures in the gas phase without the complications from bulk solvent. One of the most common techniques to study structures of gaseous ions is infrared multiple photon dissociation (IRMPD) spectroscopy which has been revealing a number of surprises.²²⁻²⁴ For instance, Atkins *et al.*²⁵ have studied the interactions of lead (II) ions with glycine in the gas phase by using IRMPD spectroscopy in the N-H/O-H stretching region. Their results showed that the amino acid deprotonates at the amino group rather than the expected carboxylic acid group and that lead

coordinates to the deprotonated amino group and the carbonyl oxygen. The present work has been conducted to determine the structure of gaseous complexes composed of a $[\text{Pb}(\text{Ura-H})]^+$ core. It was not possible to investigate directly the $[\text{Pb}(\text{Ura-H})]^+$ core due to a combination of its high dissociation energy and the low power of the laser used in these experiments. Three complexes involving the $[\text{Pb}(\text{Ura-H})]^+$ core were investigated, $[\text{Pb}(\text{Ura-H})(\text{Ura})]^+$ composed of two uracils as well as the singly and doubly hydrated $[\text{Pb}(\text{Ura-H})]^+$ complexes, $[\text{Pb}(\text{Ura-H})(\text{H}_2\text{O})]^+$ and $[\text{Pb}(\text{Ura-H})(\text{H}_2\text{O})_2]^+$.

4.2. Methods

4.2.1 Experimental

An ApexQe 70 Bruker Fourier transform ion cyclotron resonance (FT-ICR) coupled to a 10Hz Nd:YAG pumped OPO (KTP, Euroscan) was used for this study. Details of the coupling of these two instruments will be presented in a forthcoming article. Uracil and lead nitrate were purchased from Sigma Aldrich and used without any purification. Solutions of 1mM uracil and 1mM lead nitrate were prepared in 18 M Ω Millipore water. The solutions were introduced in the source using a syringe pump at a flow rate of 100 $\mu\text{L}/\text{h}$. Electrosprayed ions were stored in the hexapole accumulation cell for 1-2 s prior to being transferred to the ICR cell. To solvate ions,²⁶ the Ar flow to the hexapole cell was stopped and water vapour was allowed to flow into the hexapole cell. The ions were expected to have an ambient internal energy since they were stored in the hexapole for accumulation and/or solvation at $\sim 10^{-2}$ mbar.

Ions were irradiated by using the tunable infrared laser for 1-4 s. The more weakly-bound and faster dissociating ions, ie. the doubly hydrated, were irradiated for the

shortest time, 1 s. Typically, the laser was scanned at 2 cm^{-1} intervals to produce the IRMPD spectra. The IRMPD efficiency is defined as the negative of the natural logarithm of the parent ion intensity divided by the sum of the fragment and parent ion signals.

4.2.2 Computational

Calculations were carried out by using the Gaussian 09 suite of programs.²⁷ Structures were optimized and infrared spectra were calculated with the 6-31+G(d,p) basis set for C, H, N, and O atoms while the LANL2DZ basis set and relativistic core potential were used for the Pb atom. Single point MP2 calculations were performed on all the optimized structures using the same basis set and core potential for Pb and the 6-311++G(2d,p) basis sets on C, H, N, and O. This method is abbreviated MP2/6-311++G(2d,p)//B3LYP/6-31+G(d,p) in the rest of this chapter and these calculations are used to compare the 298 K enthalpies and Gibbs energies of the isomeric species. The vibrational frequencies used to compute the zero-point energies and thermochemistries were unscaled. The infrared spectra were all scaled by a factor of 0.967 to compare with the experimental spectra. The predicted IR absorption bands are further convoluted by a Lorentzian function with a width (FWHM) of 10 cm^{-1} to compare with the experimental spectra.

4.3. Results and Discussion

4.3.1. Comparison of IRMPD Spectra of $[\text{Pb}(\text{Ura-H})(\text{Ura})]^+$, $[\text{Pb}(\text{Ura-H})(\text{H}_2\text{O})]^+$, and $[\text{Pb}(\text{Ura-H})(\text{H}_2\text{O})_2]^+$

The IRMPD dissociation pathways observed for the ions under study were as

follows:



In the case of the latter, doubly hydrated $[\text{Pb}(\text{Ura-H})]^+$, a second loss of water was also observed due to the absorption of the laser by the primary fragment ion. The experimental IR spectra for $[\text{Pb}(\text{Ura-H})(\text{Ura})]^+$, $[\text{Pb}(\text{Ura-H})(\text{H}_2\text{O})]^+$, and $[\text{Pb}(\text{Ura-H})(\text{H}_2\text{O})_2]^+$ in the 3200-3900 cm^{-1} region are presented in Figure 4.1. The spectrum of $[\text{Pb}(\text{Ura-H})(\text{Ura})]^+$ shows only a single sharp feature centered at 3485 cm^{-1} which can be assigned to N-H stretching vibrations. As there are expected to be at most three N-H bonds, such a simple spectrum might be indicative of a somewhat "symmetric" structure for this complex containing lead, uracil and a deprotonated uracil.

The spectrum for $[\text{Pb}(\text{Ura-H})(\text{H}_2\text{O})]^+$ is composed of only two sharp bands. One is centred at 3484 cm^{-1} , very similar to the band observed in the $[\text{Pb}(\text{Ura-H})(\text{Ura})]^+$ spectrum. The second band at 3701 cm^{-1} is most likely due to the water. Since there is only one absorption for the water molecule, it is quite likely that this is a free O-H stretch and the other O-H bond is involved in hydrogen bonding with the deprotonated uracil. The spectrum for $[\text{Pb}(\text{Ura-H})(\text{H}_2\text{O})_2]^+$ has the same two features as those observed for $[\text{Pb}(\text{Ura-H})(\text{H}_2\text{O})]^+$, centred at 3491 and 3718 cm^{-1} . A third sharp feature appears centred at 3637 cm^{-1} . A fourth, less prominent, but broad absorption is observed to occur at slightly higher energy, to the blue of the 3718 cm^{-1} feature.

The C-H stretching vibrations are predicted to be weak and out of the range of the present experiment ($<3200 \text{ cm}^{-1}$). Each of these species and their structures are discussed

in turn, in the following sections.

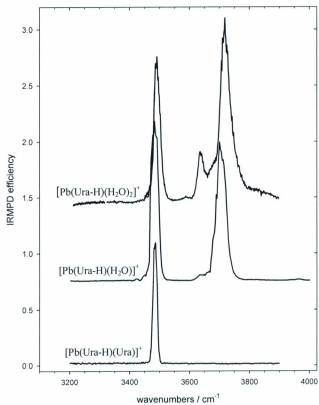


Figure 4.1: Comparison of the IRMPD spectra of [Pb(Ura-H)(Ura)]⁺, [Pb(Ura-H)(H₂O)]⁺, and [Pb(Ura-H)(H₂O)₂]⁺.

4.3.2. [Pb(Ura-H)(Ura)]⁺

In Figure 4.2, eight of the lowest energy structures for [Pb(Ura-H)(Ura)]⁺ are presented. The first four structures are similar in that lead is four-coordinate between two carbonyl oxygens and two deprotonated nitrogens. These first four lowest energy structures are all deprotonated at the most acidic nitrogen, N3,²⁸⁻³³ of the left uracil. The right uracil of N3O4/N3O2 has seen a shift of the hydrogen from the N3 to O4 and there is a hydrogen bond between O4H of the right uracil and O2 of the left. Also, lead in N3O4/N3O2 is bound to deprotonated N3 and O4 of the left uracil and deprotonated N3 and O2 on the right ring. N3O4/N3O4 is almost identical except the hydrogen from N3 of the right uracil has been transferred to O2 which results in a hydrogen bond to O2 of the left ring and lead is, again, bound to deprotonated N3 and O4 of both uracils. N3O4/N3O2 is lower in Gibbs energy than the N3O4/N3O4 isomer, but only by 3.2 kJ mol⁻¹ making them virtually isoenergetic. The next two structures, N3O2/N3O2 and N3O2/N3O4, are 7.7 and 8.0 kJ mol⁻¹ higher in Gibbs energy, respectively, than the lowest energy structure. The right uracil in N3O2/N3O2 has seen the hydrogen from N3 shifted to O4, and a hydrogen bond between O4H of the right uracil and O4 of the left. In N3O2/N3O4, hydrogen has been shifted from N3 to O2 of the right hydrogen and the resulting O2H is hydrogen bound to O4 of the left uracil. Lead is bound to N3 and O2 of the right uracil in N3O2/N3O2 and to N3 and O4 of the right uracil in N3O2/N3O4.

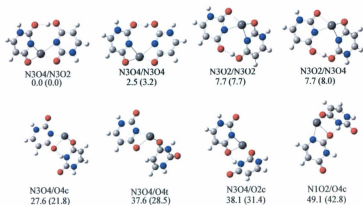


Figure 4.2: Eight of the lowest-energy structures of $[\text{Pb}(\text{Ura-H})(\text{Ura})]^+$. The 298 K relative enthalpies and Gibbs free energies (in parentheses) reported in kJ mol^{-1} were calculated at the MP2/6-311++G(2d,p)//B3LYP/6-31+G(d,p) level of theory. All species have a single positive charge.

As can be seen in Figure 4.3, the predicted spectra for the two lowest energy structures are almost identical in the $3200\text{--}3900\text{ cm}^{-1}$ region and both are in agreement with the experimental IRMPD spectrum. The observed and predicted bands are actually composed of two N-H stretching vibrations, but they are predicted to be only $\sim 8\text{ cm}^{-1}$ separated from one another, accounting for the observation and prediction of only one feature. The predicted spectra for N3O2/N3O2 and N3O2/N3O4 are identical to one another and thus the latter has been left out of Figure 4.3 for clarity. The two N-H stretching vibrations for structure N3O2/N3O2 are predicted to be $\sim 16\text{ cm}^{-1}$ apart, resulting in two slightly resolved bands. It is really uncertain whether our laser could resolve these two bands, but we do note that the observed feature is quite sharp. For all

three structures, the hydrogen bond is strong resulting in shifts of the O-H stretch to below 2800 cm^{-1} in all cases, below the limit of the available laser. Spectroscopically the two lowest energy structures cannot be differentiated, and perhaps N3O2/N3O2 and N3O2/N3O4 cannot be differentiated either. However, N3O2/N3O2 and N3O2/N3O4 are unlikely candidates as major contributors to the IRMPD spectrum based on their higher relative energies—they are predicted to be present in less than 1 part in 20 each compared to the lowest energy isomer.

The N3O4/O4c, N3O4/O4t and N3O4/O2c isomers (c and t refer to cis and trans—depending on whether uracil has an N-H bond or a C-H bond, respectively, pointing toward the $[\text{Pb}(\text{Ura-H})]^+$ core), in Figure 4.2, see lead binding in a three-coordinate fashion. In each, lead binds to the N3 deprotonated nitrogen and O4 of the deprotonated uracil, and to one of the carbonyl oxygens on the second uracil. They are all higher in Gibbs energy by between 22 and 31 kJ mol^{-1} compared to the lowest energy structure which, on thermodynamic grounds, make them unlikely contributors to the observed spectrum. Isomers N3O4/O4c and N3O4/O4t have lead bound to O4 of the second uracil, while in N3O4/O2c, it is bound to O2. Structures N3O4/O4c and N3O4/O2c have intramolecular hydrogen bonds between the two uracils. As seen in Figure 4.3, these weak intramolecular hydrogen bonds result in a red-shift of the N-H stretch that is not observed experimentally. Similarly, the calculations predict different positions for the N-H stretches for N3O4/O4t and N3O4/O2c, but that is not observed experimentally. The lowest energy structure where uracil has been deprotonated at N1, N1O2/O4c is 42.8 kJ mol^{-1} higher in Gibbs energy than N3O4/N3O2. Based on energy it is unlikely to be a

contributor to the spectrum, and it can be ruled out spectroscopically as well since the hydrogen bonded N-H stretch is not observed, nor are the multiple N-H stretches which are predicted by the calculations. There are many other structures as seen in Appendix 15. All of them can be ruled out spectroscopically, and due to their thermochemistry relative to the lowest energy isomer.

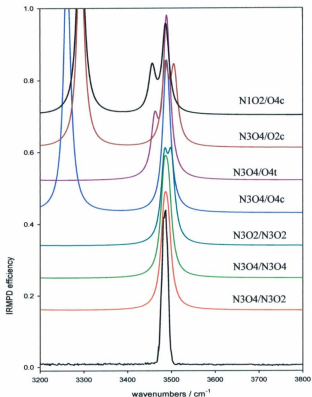


Figure 4.3: Experimental IRMPD spectra of $[\text{Pb}(\text{Ura-H})(\text{Ura})]^+$ compared with B3LYP/6-31+G(d,p) spectra for $[\text{Pb}(\text{Ura})(\text{Ura-H})]^+$ structures shown in Figure 4.2.

4.3.3. [Pb(Ura-H)(H₂O)]⁺

Based on the experimental IRMPD spectrum containing a feature in the N-H stretch region (3484 cm⁻¹) and one in the O-H stretch region (3701 cm⁻¹), the structure of [Pb(Ura-H)(H₂O)]⁺ is most likely one in which we have the same lowest-energy [Pb(Ura-H)]⁺ core as for [Pb(Ura-H)(Ura)]⁺, discussed in the previous section, where uracil is deprotonated at the most acidic site²⁸⁻³³, N3, so that the band at 3484 cm⁻¹ is the N1-H stretch. Also, the position of the O-H stretch, 3701 cm⁻¹, is intermediate between where the free water symmetric and antisymmetric stretching vibrations (3657 and 3756 cm⁻¹, respectively)³⁴ might occur. The water is most likely participating in a hydrogen bond acting as a hydrogen bond donor. In Figure 4.4, N3O4/wbO2 (wb means water is "bridged", or hydrogen bonded, in this case to O2) has lead bound to N3 and O4 and water bound to lead and acting as a hydrogen bond donor to O2. Slightly higher in energy, N3O2/wbO4 differs only in that lead is bound to O2 and water is hydrogen bonded to O4.

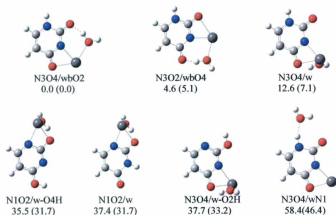


Figure 4.4: Seven computed structures for $[\text{Pb}(\text{Ura-H})(\text{H}_2\text{O})]^+$. The 298 K MP2/6-311+G(2d,p)//B3LYP/6-31++G(d,p) relative enthalpies, and Gibbs energies (in parentheses) in kJ mol^{-1} are provided for each structure. All species have a single positive charge.

As can be seen in Figure 4.5, the computed IR spectra for the lowest energy for both of these structures agree well with the experimental spectrum and it is impossible to distinguish between the two spectroscopically in the $3200\text{--}4000\text{ cm}^{-1}$ region. The band at 3701 is assigned to the free O-H stretch of water. Based on the relative thermochemistry, it is not expected that N3O2/wbO4 contributes to the experimental spectrum by more than 10% compared to N3O2/wbO2. The main difference which would allow spectroscopic differentiation might be the hydrogen bonded O-H stretch which is predicted to occur at 2825 and 2330 cm^{-1} for N3O2/wbO2 and N3O2/wbO4, respectively. The huge difference is due to the hydrogen bond for structure N3O2/wbO4 being stronger since O4 is more basic than O2. The water bend is predicted to occur at 1572 and 1622

cm^{-1} for N3O2/wbO2 and N3O2/wbO4 , respectively, and the out of phase C=O stretch is expected at 1534 and 1464 cm^{-1} , respectively, which could also be used to aid in distinguishing these two isomers (see Appendix 16).

N3O4/w is 7.1 kJ mol^{-1} higher in Gibbs energy than N3O4/wbO2 and also has a water bound to lead but it is not participating in any hydrogen bonding. It is obvious from Figure 4.5 that the predicted spectrum for this structure is not in agreement with the experimental IRMPD spectrum. Similarly, the tautomeric structures N1O2/w-O4H and N1O2/w , which are much higher in energy due to being deprotonated at N1, can be ruled out spectroscopically. N3O4/w-O2H is a tautomer of N3O4/w where hydrogen transferred from N1 to O2 and can be ruled out spectroscopically. Structure N3O4/wN1 is some 46 kJ mol^{-1} higher in Gibbs free energy is the only structure considered where a water is not bound to lead but is bound by a hydrogen bond to N1H. This results in the N1H stretch being red-shifted to 3115 cm^{-1} which is just beyond the useful output of our laser. The water symmetric and antisymmetric stretching vibrations, predicted to be at 3674 and 3791 cm^{-1} , respectively, are not observed. All but the two lowest energy isomers, N3O4/wbO2 and N3O2/wbO4 , can be ruled out on spectroscopic and thermochemical grounds from being present in any significant amount.

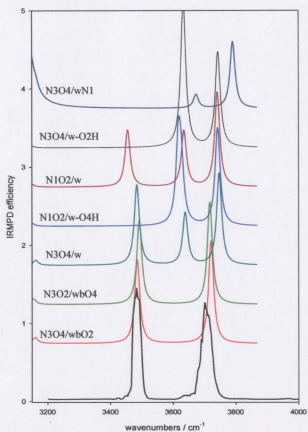


Figure 4.5: Comparison of the experimental IRMPD spectrum for $[\text{Pb}(\text{Ura-H})(\text{H}_2\text{O})]^+$ and the predicted IR spectra for the computed structures in Figure 4.4.

4.3.4. $[\text{Pb}(\text{Ura-H})(\text{H}_2\text{O})_2]^+$

Like $[\text{Pb}(\text{Ura-H})\text{H}_2\text{O}]^+$, the two lowest energy structures of $[\text{Pb}(\text{Ura-H})(\text{H}_2\text{O})_2]^+$ are based on lead bound either to deprotonated N3 and O4 or to deprotonated N3 and O2 refer to Figure 4.6. Furthermore, N3O4/wbO2/w and N3O2/wbO4/w can be considered to

be formed from a water molecule adding to N3O4/wbO2 and N3O2/wbO4 in Figure 4.4, respectively. The predicted infrared spectra of these two lowest energy complexes are identical in the 3200-3900 cm^{-1} region, and so cannot be differentiated spectroscopically in this region (see Figure 4.7).

Do the calculated infrared spectra compare favourably with the experimental IRMPD spectrum? The resolved bands in the experimental IRMPD spectrum of $[\text{Pb}(\text{Ura}-\text{H})(\text{H}_2\text{O})_2]^+$ at 3491 and 3718 cm^{-1} can be assigned to the N-H stretch and the free O-H stretch of the water molecule that is bound to lead and hydrogen bonded to either O4 or O2. These assignments are the same as those made for $[\text{Pb}(\text{Ura}-\text{H})(\text{H}_2\text{O})]^+$. The band at 3637 cm^{-1} agrees quite well with the symmetric stretch of the out of plane water bound to lead in both N3O4/wbO2/w and N3O2/wbO4/w. The 3637 cm^{-1} band is also in a similar position to the symmetric O-H stretch of water bound to $\text{Li}(\text{Ura})^+$ at 3635 cm^{-1} ,³⁵ to $\text{Li}(\text{Thy})(\text{Ade})^+$ at 3658 cm^{-1} ,³⁶ and to $\text{M}(\text{Ade})^+$, where M is Li, Na, K (all $\sim 3640 \text{ cm}^{-1}$).³⁷

In the IRMPD spectrum there is also a broad absorption that grows more intense proceeding to the red of 3900 cm^{-1} and which can also be seen to contribute to IRMPD intensity between the 3718 and 3637 cm^{-1} bands. It has been observed in the past that the antisymmetric O-H stretch of water bound to metal ions observed by consequence spectroscopy is broadened and not nearly as intense as would be expected by an absorption spectroscopy measurement.^{35,38,39} This phenomenon has been explained.³⁹ Briefly, consequence spectroscopies such as IRMPD spectroscopy rely on intramolecular vibrational-energy redistribution (IVR) following each photon absorption in order to be able to absorb multiple photons and cause dissociation. If there is not good IVR, then the

mode is not available to absorb further photons. Anharmonic calculations for $\text{Li}(\text{Ura})(\text{H}_2\text{O})^+$ and $\text{Li}(\text{Ura})(\text{H}_2\text{O})_2^+$ predicted cubic coupling constants for the antisymmetric stretch can be as much as 3-4 orders of magnitude smaller than those for their symmetric stretch.³⁵ It is our premise that the antisymmetric O-H stretch predicted to be at 3753 cm^{-1} is observed as IRMPD intensity between 3600 and 3900 cm^{-1} but is masked by the very intense free O-H stretch of the hydrogen bonded water. Furthermore, while we cannot rule out N3O2/wbO4/w spectroscopically, based on the calculated thermochemistry its presence is expected to be 8 % less than that of N3O4/wbO2/w at 298 K.

In N3O4/wbO2/ww and N3O4/wbO2/wN1, the second water is hydrogen bound as a hydrogen bond acceptor to either the first water or to N1H, respectively. These structures are considerably higher in energy than the two lower energy ones and are not expected to be present in any quantity measureable spectroscopy. N1O2/w/w is deprotonated at N1, lead is bound to N1 and O2, and both water molecules are bound to lead; it is a much higher energy structure. The computed infrared spectra for these three species are clearly not in agreement with the experimental IRMPD spectrum and can be ruled out as contributors.

A slight blue shift in the position of the free O-H stretch of the hydrogen bonded water molecule is observed between the singly and doubly solvated species, 3701 cm^{-1} $[\text{Pb}(\text{Ura-H})(\text{H}_2\text{O})]^+$ and 3718 for $[\text{Pb}(\text{Ura-H})(\text{H}_2\text{O})_2]^+$ and deserves discussion. This blue shift can be explained as the positive charge is shared not only by one water molecule as in $[\text{Pb}(\text{Ura-H})(\text{H}_2\text{O})]^+$, but by two water molecules in $[\text{Pb}(\text{Ura-H})(\text{H}_2\text{O})_2]^+$. The simple

Mulliken charge distribution shows that the water molecule in $[\text{Pb}(\text{Ura-H})(\text{H}_2\text{O})]^+$ has a charge of 0.126. Adding a second water molecule reduces the overall charge on the first to 0.071. This also results in a weaker and therefore elongated hydrogen bond, 1.597 Å vs 1.642 Å respectively, for the singly and doubly hydrated species. The extra electron density provided by the second water molecule in $[\text{Pb}(\text{Ura-H})(\text{H}_2\text{O})_2]^+$ results in a slightly stronger O-H bond of the first water molecule and a slight blue shift in the position of the vibrational mode.

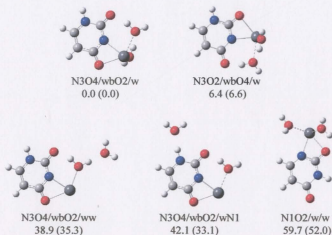


Figure 4.6: B3LYP/6-31+G(d,p) structures of five $[\text{Pb}(\text{Ura-H})(\text{H}_2\text{O})_2]^+$ structures. The 298 K MP2/6-311++G(2d,p)//B3LYP/6-31+G(d,p) relative enthalpies and Gibbs energies (in parentheses) in kJ mol^{-1} are provided. All species have a single positive charge.

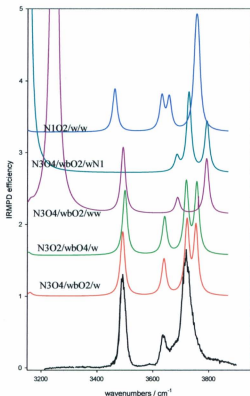


Figure 4.7: The IRMPD spectrum for $[\text{Pb}(\text{Ura-H})(\text{H}_2\text{O})_2]^+$ in the 3200-3900 cm^{-1} range compared to the computed spectra for the five complexes shown in Figure 4.6.

4.3.5 Structure of $[\text{Pb}(\text{Ura-H})]^+$

We were unable to obtain spectra for $[\text{Pb}(\text{Ura-H})]^+$, likely due to the high energies required for dissociation. This is a limitation of IRMPD spectroscopy, especially using a table-top OPO laser. However, our results, especially on $[\text{Pb}(\text{Ura-H})(\text{H}_2\text{O})]^+$ and $[\text{Pb}(\text{Ura-}$

$\text{H}(\text{H}_2\text{O})_2]^+$ clearly show that there is no spectroscopic evidence for structures of these ions which contain the N1 deprotonated isomer with lead attached to N1 and O2 like N1O2 in Figure 4.8. Remember that the hydrated ions are formed by storing electrosprayed $[\text{Pb}(\text{Ura-H})]^+$ in the hexapole accumulation cell with a high pressure ($\sim 10^{-2}$ mbar of water vapour), which should be a fairly soft association process with many thermalizing collisions to soak up the energy of association. The three lowest energy structures of $[\text{Pb}(\text{Ura-H})]^+$ are shown in Figure 4.8. Based on the thermodynamics it is clear that N3O4 is by far the lowest energy complex being 15.3 kJ mol^{-1} lower in Gibbs energy than N3O2 at the MP2/6-311++G(2d,p)//B3LYP/6-31+G(d,p). The relative thermochemistries for these structures agree well with the previously reported B3LYP/6-311+G(3df,2p) calculations.²⁰ It is true that association of water tends to equalize the energies of the N3O4 and N3O2 "cores" as seen by the relative energies of structures N3O4/wbO2 and N3O2/wbO4 as well as N3O4/wbO2/w and N3O2/wbO4/w in Figures 4.4 and 4.6, respectively. This is not true for the N1O2 core as seen by structures N1O2/w and N1O2/w/w in Figures 4.4 and 4.6, respectively. Our experiments especially, as well as our calculations, suggest that the structure of $[\text{Pb}(\text{Ura-H})]^+$ which is electrosprayed is that of N3O4.

Guillaumont *et al.*²⁰ studied the CID fragmentation of electrosprayed $[\text{Pb}(\text{Ura-H})]^+$. The major dissociation routes observed were loss of isocyanic acid and the formation of PbNCO^+ . Isotopic labeling studies also showed that isocyanic acid loss was exclusively loss of N3 and C2. The other major CID product ion, PbNCO^+ , also exclusively includes N3 and C2. In order to explain these major CID products, isomers N3O2 and N1O2

(Figure 4.8) were assumed to be present in the mixture of ions electrosprayed, even though their energies are substantially higher than N3O4.

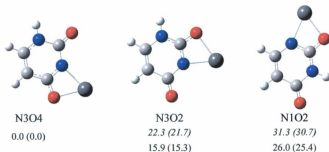


Figure 4.8: Three lowest energy B3LYP/6-31+G(d,p) structures for [Pb(Ura-H)]⁺. The 298 K MP2/6-311++G(2d,p)//B3LYP/6-31+G(d,p) relative enthalpies and Gibbs energies (in parentheses) as well as the B3LYP/6-31+G(d,p) energies (in italics top), all in kJ mol⁻¹ are provided. All species have a single positive charge.

Their calculations²⁰ of the potential energy surface showed that PbNCO⁺ can be easily explained as arising from N3O2. Although the N3O2 isomer is significantly higher in energy than N3O4 under CID conditions, it is quite plausible that N3O2 can be formed as an intermediate from N3O4 *en route* to PbNCO⁺. Isocyanic acid loss was only considered to be accessible through the N1O2 isomer which was said to be present in the mixture of electrosprayed ions. Our experiments do not support this conclusion in that we see no evidence for the N1O2 isomer, certainly not in enough abundance that the major dissociation route stems from it. It is not the intent of this work to explore the potential energy surface for [Pb(Ura-H)]⁺ dissociation, but we suggest that there is probably an

accessible route for N3O4 to lose HNCO under energetic CID conditions and would be consistent with the HNCO fragment coming from N3 and C2 of [Pb(Ura-H)]⁺.

4.4. Summary

The structures of [Pb(Ura-H)(Ura)]⁺, [Pb(Ura-H)(H₂O)]⁺, and [Pb(Ura-H)(H₂O)₂]⁺ have been explored using IRMPD spectroscopy in the N-H/O-H stretching region and by computational methods. In all cases, the computed spectra for the lowest energy structures agree very well with the experimental IRMPD spectrum. All these structures involved a [Pb(Ura-H)]⁺ core which is deprotonated at N3 and has lead bound to either N3 and O4 or N3 and O2. Our results suggest that the [Pb(Ura-H)]⁺ structure that is deprotonated at N1 and lead is bound to N1 and O2 is not an observable contributor to the electrosprayed complexes.

4.5. Acknowledgements

The authors acknowledge the financial contributions of the NSERC Discovery Grants program, the Canadian Foundation for Innovation, Memorial University, and Bruker Daltonics. We also would like to congratulate Professor Eyley on his retirement. The authors are also grateful for the very helpful reviewer's comments.

4.6 References

- (1) Ma- Jennifer, C.; Dougherty, D. A. *Chem. Rev.* **1997**, *97*, 1303.
- (2) Pyle, A. M. *J. Biol. Inorg. Chem* **2002**, *7*, 679.
- (3) Misra, V. K.; Draper, D. E. *Biopolymers* **1998**, *48*, 113.
- (4) Hanna, R.; Doundna, J. A. *Curr. Opin. Chem. Biol* **2000**, *4*, 166.
- (5) Madore, E.; Florentz, C.; Giege, R.; Lapointe, J. *Nucleic Acids Res* **1999**, *27*, 3583.
- (6) Shui, X.; Sines, C. C.; McFail-Isom, L.; VanDerveer, D.; Williams, L. D. *Biochem* **1998**, *37*, 16877.
- (7) Eichhorn, G. L. *Adv. Inorg. Biochem* **1981**, *3*, 1.
- (8) Dove, W. F.; Davidson, N. *J. Mol. Biol* **1962**, *5*, 467.
- (9) Eichhorn, G. L.; Shin, Y. A. *J. Am. Chem. Soc* **1968**, *90*, 7323.
- (10) Sponer, j.; Leszczynski, J.; Hobza, P. *J. Phys. Chem* **1996**, *100*, 1965.
- (11) Burda, J. V.; Sponer, j.; Leszczynski, J.; Hobza, P. *J. Phys. Chem. B* **1997**, *101*, 9670.
- (12) Saenger, W. *Principles of Nucleic Acid Structure*, Springer-Verlag, New York, 1984.
- (13) Cerda, B. A.; Wesdemiotis, C. *J. Am. Chem. Soc* **1996**, *118*, 11884.
- (14) McFail-Isom, L.; Sines, C. C.; Williams, L. D. *Curr. Opin. Struct. Bio* **1999**, *9*, 298.
- (15) Goyer, R. A.; Seiler, H. G.; Sigel, H.; Sigel, A. *Handbook on Toxicity of Inorganic Compounds*. Dekker, New York, 1988.
- (16) Martin, R. B.; Seiler, H. G.; Sigel, H.; Sigel, A. *Handbook on Toxicity of Inorganic Compounds*. Dekker, New York, 1988.

- (17) Da Costa, C. P.; Sigel, H. *J. Biol. Inorg. Chem* **1999**, *4*, 508514.
- (18) Da Costa, C. P.; Sigel, H. *Inorg. Chem* **2000**, *39*, 5985.
- (19) Sigel, H.; Da Costa, C. P.; Martin, R. B. *Coord. Chem. Rev* **2001**, *219*, 435.
- (20) Guillaumont, S.; Tortajada, J.; Salpin, J. Y.; Lamsabhi, A. M. *Int. J. Mass Spectrom* **2005**, *243*, 279.
- (21) Salpin, J. Y.; Guillaumont, S.; Tortajada, J.; Lamsabhi, A. M. Gas-Phase Interactions Between Lead(II) Ions and Thiouracil Nucleobases: A Combined Experimental and Theoretical Study. In *J. Am. Soc. Mass Spectrom*, 2009; Vol. 20; pp 359.
- (22) Eyler, J. R. *Mass Spectrom Rev* **2009**, *28*, 448.
- (23) Fridgen, T. D. *Mass Spectrom Rev* **2009**, *28*, 586.
- (24) Polfer, N. C.; Oomens, J. *Mass Spectrom Rev* **2009**, *28*, 468.
- (25) Atkins, C. G.; Banu, L.; Rowsell, M.; Blagojevic, V.; Bohme, D. K.; Fridgen, T. D. *J. Phys. Chem. B* **2009**, *113*, 14457.
- (26) Rajabi, K.; Easterling, M. L.; Fridgen, T. D. *J. Am. Soc. Mass Spectrom* **2009**, *20*, 411.
- (27) Frisch, M. J. T., G. W.; Schlegel, H. B.; Scuseria, G. E.; Robb, M. A.; Cheeseman, J. R.; Montgomery, J. A., Jr.; Vreven, T.; Kudin, K. N.; Burant, J. C.; Millam, J. M.; Iyengar, S. S.; Tomasi, J.; Barone, V.; Mennucci, B.; Cossi, M.; Scalmani, G.; Rega, N.; Petersson, G. A.; Nakatsuji, H.; Hada, M.; Ehara, M.; Toyota, K.; Fukuda, R.; Hasegawa, J.; Ishida, M.; Nakajima, T.; Honda, Y.; Kitao, O.; Nakai, H.; Klene, M.; Li, X.; Knox, J. E.; Hratchian, H. P.; Cross, J. B.; Adamo, C.; Jaramillo, J.; Gomperts, R.; Stratmann, R.

E.; Yazyev, O.; Austin, A. J.; Cammi, R.; Pomelli, C.; Ochterski, J. W.; Ayala, P. Y.; Morokuma, K.; Voth, G. A.; Salvador, P.; Dannenberg, J. J.; Zakrzewski, V. G.; Dapprich, S.; Daniels, A. D.; Strain, M. C.; Farkas, O.; Malick, D. K.; Rabuck, A. D.; Raghavachari, K.; Foresman, J. B.; Ortiz, J. V.; Cui, Q.; Baboul, A. G.; Clifford, S.; Cioslowski, J.; Stefanov, B. B.; Liu, G.; Liashenko, A.; Piskorz, P.; Komaromi, I.; Martin, R. L.; Fox, D. J.; Keith, T.; Al-Laham, M. A.; Peng, C. Y.; Nanayakkara, A.; Challacombe, M.; Gill, P. M. W.; Johnson, B.; Chen, W.; Wong, M. W.; Gonzalez, C.; Pople, J. A. Gaussian 09 ed.; Gaussian, Inc.: Wallingford, 2008.

- (28) Kurinovich, M. A.; Lee, J. K. *J. Am. Chem. Soc.* **2000**, *122*, 6258.
- (29) Nguyen, M. T.; Chandra, A. K.; Zeegers-Huyskens, T. *J. Chem. Soc. Faraday Trans* **1998**, *94*, 12771280.
- (30) Chandra, A. K.; Nguyen, M. T.; Uchimaru, T.; Zeegers-Huyskens, T. *J. Phys. Chem. A* **1999**, *103*, 8853.
- (31) Miller, T. M.; Arnold, S. T.; Viggiano, A. A.; Miller, A. E. S. *J. Phys. Chem. A* **2004**, *108*, 3439.
- (32) Huang, Y. Q.; Kenttamaa, H. *J. Phys. Chem. A* **2003**, *107*, 4893.
- (33) Kurinovich, M. A.; Lee, J. K. *J. Am. Soc. Mass Spectrom* **2002**, *13*, 985.
- (34) Shimanouchi, T. *Nat. Bur. Stand* **1972**, *1*, 1.
- (35) Gillis, E. A. L.; Rajabi, K.; Fridgen, T. D. *J. Phys. Chem. A* **2009**, *113*, 824.
- (36) Gillis, E. A. L.; Fridgen, T. D. *Int. J. Mass Spectrom* **2010**, *297*, 2.
- (37) Rajabi, K.; Gillis, E. A. L.; Fridgen, T. D. *J. Phys. Chem. A* **2010**, *114*, 3449.
- (38) Bush, M. F.; Saykally, R. J.; Williams, E. R. *Chem. Phys. Chem* **2007**, *8*, 2245.

- (39) Pankewitz, T.; Lagutschenkov, A.; Niedner-Schatteburg, G.; Xantheas, S. S.; Lee, Y.
T. J. Chem. Phys. **2007**, *126*, 74307.

Chapter 5

Infrared Characterization of Hydrogen-Bonded Propylene Oxide/Ethanol and Propylene Oxide/ 2-Fluoroethanol Complexes Isolated in Solid Neon Matrices

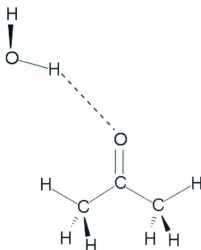
5.1. Introduction*

Hydrogen bonding is a vital component in many biochemical processes and it is prominent in many fields of chemistry and physics. Many fundamental studies have been done to examine hydrogen bonding interactions between species such as alcohols,¹⁻⁴ hydrogen halides,⁵⁻⁹ and water¹⁰⁻¹³ which have resulted in determining the structures of these complexes in both the gas phase and under matrix isolation conditions.

The study of hydrogen bonded complexes reveals important information on intermolecular interactions. For example Sang and Kim¹⁴ have published studies of the infrared spectra of the 1:1 dimethyl ether-methanol complex in solid argon matrices.

**This chapter has been submitted to be published as O. Y. Ali, E. Jewer and T. D. Fridgen, *Vibrational Spectroscopy*. 2011.*

Upon complexation, red shifts in the O-H stretching vibration for methanol and blue shifts in the CH₃ stretch for dimethyl ether were observed. Comparisons with calculations were taken as strong evidence that the most stable 1:1 dimethyl ether-methanol complex assumes a near linear structure about the hydrogen bond and that the symmetry planes for the monomers were nearly planar. Comparing the O-H shifts between similar hydrogen-bonded complexes (ie. water/dimethyl ether, acetone/methanol), a correlation was noted between the proton affinities (ie. basicities) of the hydrogen bond acceptor and the red shift of the O-H stretch. Zhang et al.¹⁵ studied the weakly bound complex between acetone and water in which water is hydrogen bonded to the carbonyl oxygen of acetone. They observed red-shifts for the carbonyl stretching mode of acetone and the hydroxyl group O-H stretching modes of water. They suggested a structure for the 1:1 acetone-water complex where water is hydrogen bonded to the carbonyl group of acetone (see Scheme 5.1). This structure was confirmed, in part, by comparing the experimental infrared spectra and ab initio calculated infrared spectra. Acetone-methanol complexes have also been studied in argon matrices at 9K.¹⁶ In this study acetone and methanol formed a 1:1 binary complex. From the observed new red shifts of the hydroxyl group in methanol and the carbonyl group in acetone, combined with ab initio calculations Kim and Sang suggested a hydrogen bonded structure very similar to the acetone-water complex (see Scheme 5.1). Many other 1:1 hydrogen bonded complexes such as formamide-water,¹⁷⁻¹⁹ formamide-methanol,^{18,19} and formamide-hydrogen fluoride complexes²⁰ have been studied. All formed structures similar to the acetone-water and acetone-methanol complexes.



Scheme 5.1: Structure of the acetone-water hydrogen bonded complex.

Propylene oxide-ethanol and propylene oxide-2-fluoroethanol complexes have been used to illustrate Fischer's lock-and-key principle.^{21,22} In these complexes, ethanol or 2-fluoroethanol acts as the proton donor in a primary O-H...O hydrogen (H) - bond and provides the shape of key. However, propylene oxide acts as the H-bond acceptor and can be viewed as a solid lock. The propylene oxide-ethanol complex has six possible hydrogen bonded conformations and the rotational constants of all of them were investigated. Theoretically, propylene oxide-2-fluoroethanol has fourteen conformers, however, experimentally only the rotational spectra of three conformers, two anti and one syn, have been observed.

To achieve the detailed structure by interaction of oxygen atom in propylene oxide and hydroxyl group, we have studied the infrared spectra of mixtures of propylene oxide and ethanol in cryogenic matrices. In addition, density functional and ab initio calculations have been used to interpret the observed spectra.

5.2. Methods

5.2.1. Experimental

The bulk of the matrix isolation apparatus at Memorial University was obtained from Drs. John Allison and George Leroi (then) from the Department of Chemistry at Michigan State University.²³⁻²⁶ Since many modifications have been made, a complete description is provided here.

A schematic of the matrix isolation apparatus is provided in Figure 5.1. The 8 inch diameter stainless steel vacuum chamber is pumped by an APD cryopump providing base pressures of 10^{-8} to 10^{-9} torr. The 1 inch KBr cold window is mounted in a copper window holder using indium metal gaskets to provide contact between the KBr and window holder. The window holder is mounted to the cold head of a Sumimoto Model SDRK205DW cryocooler system also using indium metal gaskets. The cold head is cooled to 4.2 K by a CKW-21 closed-cycle helium refrigeration system. The temperature is monitored with a Lakeshore Cryotronics 330 controller and a DT-470 Si-diode sensor. The temperature controller is also used to warm the sample window up for annealing experiments.

The radiation from a Nicolet 6700 Fourier transform infrared (FTIR) spectrometer is taken externally from the spectrometer, is reflected off mirror M1 (90° off axis

paraboloid, 15 cm focal length, 7.5 cm aperture) to a second mirror, M2 (90° off axis ellipsoid, 56 cm focal length, 3.2 cm aperture). M2 directs the radiation through a 2.5 cm KBr entrance window, the sample, and a 2.5 cm KBr exit window after which it is reflected off M3 (flat mirror) and M4 (90° off axis paraboloid, 10 cm focal length, 7.5 cm aperture) and through a biconvex ZnSe lens (2.5 cm diameter, 2.5 cm focal length) onto a Thermo mercury-cadmium-telluride (MCT-B) detector. All spectra reported here were recorded between 4000 and 500 cm^{-1} at 0.5 cm^{-1} resolution with 1000 scans averaged.

Propylene oxide (99% purity), ethanol (anhydrous ethanol), ethanol-d6 (Aldrich, 99.5% purity), and 2-fluoroethanol (Aldrich, 95% purity) were subjected to three freeze-pump-thawed cycles to expel dissolved gases and mixed in a stainless-steel reservoir as vapour. Gaseous solutions of ethanol/propylene oxide/neon or 2-fluoroethanol/propylene oxide/neon were mixed in ratios of approximately 1/1-15/3000. The mixtures were deposited at a rate of 1.6 cm^3/min . Spectra were recorded following a deposition period of about 14 h. The matrix was annealed at 10 and 14 K each for an hour, an IR spectrum recorded after each annealing step.

5.2.2. Computational

Ab initio calculations were performed using the GAUSSIAN 03 program.²⁷ The structures and vibrational frequencies of the isolated monomers, ethanol, propylene oxide, 2-fluoroethanol, the propylene oxide-ethanol complexes and propylene oxide-2-fluoroethanol complexes were optimized using B3LYP/6-311++G(2d,2p). Single-point calculations were done at the MP2 level of theory on all optimized geometries using the 6-311++G(2d,2p) basis set. Relative thermochemistries reported are composed of MP2/6-

311++G(2d,2p) electronic energies with thermal corrections from the B3LYP/6-311++G(2d,2p) frequency calculations, called MP2/6-311++G(2d,2p)//B3LYP/6-311++G(2d,2p) from here on.

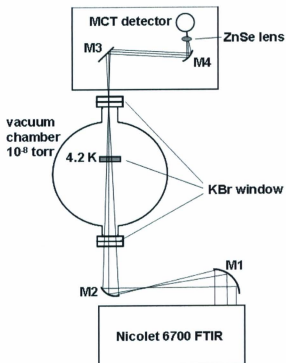


Figure 5.1: Schematic of matrix isolation instrumentation showing the optical configuration for FT-infrared spectroscopy.

5.3. Results and Discussion

5.3.1. Infrared Spectra of Ethanol, d6-Ethanol, and Propylene Oxide: A Scaling "Equation"

Infrared spectra are reported for ethanol and ethanol-d6 in neon matrices at 4.2 K in Tables 5.1 and 5.2. In all cases, the use of highly diluted samples (ethanol/neon = 1/3000 ratio) produced only the monomer of ethanol, no dimers were observed. At higher ethanol concentrations (ie. 1/2500) small amounts of ethanol dimer were observed. Since the intent of this work was to observe hydrogen-bonded ethanol-propylene oxide dimers it is advantageous to begin with an ethanol concentration just below that where dimers are observed. Both conformers of ethanol, differing in the orientation of the OH bond with respect to the CCO group were observed. Ethanol has been the topic of several spectroscopic studies using microwave,²⁸ infrared,²⁹⁻³² and Raman techniques.³³ The absorptions for ethanol observed in neon are essentially the same as those observed in argon³⁴ except for the symmetric CH₃ stretch and the O-H stretch which are both shifted to a higher wavenumber by about 17 and 20 cm⁻¹, respectively.

In Table 5.3, the 4.2 K neon matrix infrared spectrum of propylene oxide is summarized. Only monomeric propylene oxide was observed, even up to propylene oxide/neon ratios of 1/200. This is in contrast to the observations of ethanol aggregation due to the lack of strong intermolecular (hydrogen bonding) forces between propylene oxide molecules.

To our knowledge the neon matrix infrared spectra of neither ethanol nor propylene oxide have been reported. The purpose here is not to compare the neon spectra with those

taken in other media or phases although the previous argon spectra³⁴ and our neon spectra for ethanol are listed in Table 5.1 and the assigned matrix spectrum for propylene oxide is in Table 5.3. Rather, using the experimental and computed spectra for ethanol, d6-ethanol, and propylene oxide, our intent is to obtain a reliable scaling "equation" for the B3LYP/6-311++G(2d,2p) calculated spectra. It is anticipated that these scaled calculations will be better suited to assist us in identifying bands for the ethanol-propylene oxide complex. Scaling computed vibrational frequencies is required to correct for errors due to the approximations made in the electronic structure calculation and because the vibrational modes are assumed to be harmonic in the calculation of these values. It has been observed that high frequency vibrations (ie. O-H, N-H and C-H stretching) typically require more extensive scaling for higher frequency vibrations,³⁵⁻³⁹ than for low frequency vibrations.⁴⁰

The concept of a scaling equation has been used previously by Gornicka et al³⁶ and Palafox⁴¹ to compare theoretical and experimental spectra of cytosine and benzene, and similarly used for the proton-bound dimer of acetone.⁴² Since two parameters are typically required to get good fits for both higher and lower-frequency vibrations, we use a two-parameter "fit" of the computed data to the experimental data. The B3LYP/6311++G(2d,2p) calculated band positions were fit to the experimental band positions for ethanol, ethanol-d6, and propylene oxide. We have used a two parameter, first-order equation to fit the data. The fit obtained is

$$\tilde{\nu}_{NE} = 27.8(\pm 4.4) + 0.9565(\pm 0.0023)\tilde{\nu}_e \quad \text{Eq.5.1}$$

where the superscripts, SE and c, represent scaling equation and calculated, respectively. The computed and experimental data were also fit to a single parameter scaling factor for comparison. This scaling factor was determined to be 0.969. A plot of the computed frequencies vs experimental frequencies and equation 5.1 can be seen in Appendix 17.

In Tables 5.1, 5.2 and 5.3, the experimental band positions are compared to those calculated using the scaling equation (SE) and the scaling factor (SF). It is evident that the scaled values agree significantly better with the experimental data for all three species. In fact, the average absolute error (and absolute standard deviations) in the scaling factor corrected values are $17.3(\pm 11.9)$, $13.4(\pm 9.3)$, and $14.9(\pm 6.1)$ cm^{-1} for ethanol, d6-ethanol and propylene oxide, respectively. Using the scaling equation the average absolute error (and absolute standard deviation) are $9.2(\pm 9.3)$, $8.6(\pm 6.4)$, and $4.0(\pm 3.5)$ cm^{-1} , respectively, for ethanol, d6-ethanol and propylene oxide. Overall the average absolute errors were determined to be $7.1(\pm 7.0)$ cm^{-1} for the scaling equation and $15.0(\pm 9.2)$ cm^{-1} for the scaling factor. The better agreement between experiment and the computed values scaled by the linear equation was deemed to be significant and was used. The computed vibrations were also fitted with a three-parameter (quadratic) equation, but the average absolute error between the experimental and scaled vibrations was found to be similar to the linear fit, 7.2 cm^{-1} , and the absolute standard deviation was not that much better, ± 5.9 cm^{-1} , than the two parameter linear fit.

In Figure 5.2 the neon matrix infrared spectrum of propylene oxide is shown in the 700-1550 and 2900-3100 cm^{-1} regions and are compared with the spectrum calculated using B3LYP/6-311++G(2d,2p) and scaled using equation 5.1. Clearly there is excellent

agreement with experiment when the computed wavenumber positions are scaled with the scaling equation.

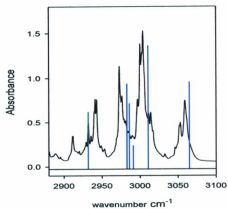
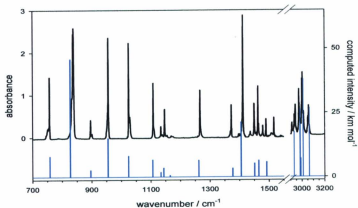


Figure 5.2: FTIR spectrum of neon matrix isolated propylene oxide in the 700 to 1550 cm^{-1} and 2900 to 3100 cm^{-1} range.

Approx description	Error SE ^e	SE ^d	Error SF ^e	SF(0.969)	calc ^c	Ne ^b	Ar ^{a,24}
$\nu(\text{OH})$	-28.1	3708.7	-48.4	3729.0	3848.3	3680.6	3660.8
$\nu_s(\text{CH}_3)$	-12.6	3003.8	-23.6	3014.8	3111.3	2991.2	2995.4
$\nu_a(\text{CH}_3)$	-12.4	2998.2	-23.4	3009.2	3105.5	2985.8	2984.6
$\nu_g(\text{CH}_3)$	17.9	2938.0	7.6	2948.3	3042.6	2955.9	2939.2
$\nu_s(\text{CH}_2)$	30.5	2911.8	20.6	2921.7	3015.2	2942.3	2917.4
$\nu_a(\text{CH}_2)$	8.2	2888.7	-1.4	2898.3	2991.0	2896.9	2899.6
$\delta(\text{CH}_2)$	1.6	1491.5	10.2	1482.9	1530.3	1493.1	1487.0
$\delta_s(\text{CH}_3)$	-3.0	1467.7	6.0	1458.7	1505.4	1464.7	1463.3
$\delta_a(\text{CH}_3)$	-1.8	1451.1	7.4	1441.9	1488.0	1449.3	1445.0
$\omega(\text{CH}_2)$	-1.4	1414.7	8.2	1405.1	1450.0	1413.3	1416.0
$\delta_s(\text{CH}_3)$	-2.7	1375.6	7.5	1365.4	1409.1	1372.9	1371.5
$\tau\omega(\text{CH}_2)$		1271.7		1260.2	1300.5		
$\delta(\text{OH})$	-2.2	1243.6	9.7	1231.7	1271.1	1241.4	1239.5
$\tau(\text{CH}_2) + \tau(\text{CH}_3)$	5.2	1154.7	18.3	1141.6	1178.1	1159.9	1161.0
$\nu(\text{COH}) + \tau(\text{CH}_3)$	14.8	1076.5	28.9	1062.4	1096.4	1091.3	1091.7
$\nu(\text{CCO}) + \tau(\text{CH}_3)$	15.5	1013.0	30.4	998.1	1030.0	1028.5	1025.0
$\nu(\text{CCO})$	8.4	883.5	25	866.9	894.6	891.9	889.4
$\tau(\text{CH}_2) + \tau(\text{CH}_3)$	0.5	814	18	796.5	822.0	814.5	811.8

a) reference for Ar matrix

b) this work

c) B3LYP/6-311++G(2d,2p)

d) scaling equation

e) $\text{obs}(\text{Ne}) - \text{scaled}$

Table 5.1: Observed and calculated (scaled) IR absorptions for the anti conformer of ethanol. All positions in cm^{-1}

Approx description	Error SE ^d	SE ^c	Error SF ^d	SF(0.96)	calc ^b	Obs Ne ^a
$\nu(\text{OD})$	7.9	2707.7	0.7	2714.9	2801.8	2715.6
$\nu_d(\text{CD}_3)$	11.4	2233.1	10.4	2234.1	2305.6	2244.5
$\nu_d(\text{CD}_1)$	12.5	2227.9	11.5	2228.9	2300.2	2240.4
$\nu_d(\text{CD}_2)$	12.3	2171.4	12.1	2171.6	2241.1	2183.7
$\nu_d(\text{CD}_3)$	4.8	2118.9	5.3	2118.4	2186.2	2123.7
$\nu_d(\text{CD}_2)$	-8.3	2104.8	-8.0	2104.2	2171.5	2096.2
$w(\text{CD}_2)$	16.9	1212.0	29.2	1199.7	1238.1	1228.9
$\delta(\text{CD}_2)$	18.3	1126.3	31.7	1112.9	1148.5	1144.6
$\delta_d(\text{CD}_1)$		1079.3		1065.2	1099.3	
$\delta_d(\text{CD}_3)$	-4.6	1062.8	9.6	1048.6	1082.1	1058.2
$\delta_d(\text{CD}_2)$	-1.5	1052.8	12.9	1038.4	1071.6	1051.3
$\delta(\text{OD})$	0	1018.1	14.9	1003.2	1035.3	1018.1
$\text{tw}(\text{CD}_2)$	1.9	982.8	17.3	967.4	998.4	984.7
$\nu(\text{CCO}) + \tau(\text{CD}_2)$	5.4	909.7	21.7	893.4	922.0	915.1
$\tau(\text{CD}_2) + \tau(\text{CD}_1)$	-15.7	906.3	0.6	890.0	918.5	890.6
$\nu(\text{CCO}) + \tau(\text{CD}_1)$	5.2	814.9	22.7	797.4	822.9	820.1
$\nu(\text{CCO})$	0.2	740.8	18.7	722.3	745.4	741.0
$\tau(\text{CD}_2) + \tau(\text{CD}_1)$	-19.5	600.4	0.9	580.0	598.6	580.9

- a) this work
b) B3LYP/6-311++G(2d,2p)
c) scaling equation
d) obs(Ne) – scaled

Table 5.2: Observed and calculated (scaled) absorption for the d_6 isotopomer of ethanol. All positions in cm^{-1} .

Approx description	Error SE ^c	SE	Error SF ^c	SF(0.969)	Calc ^b	Obs Ne ^a	Obs N ₂ ⁵⁰
$\nu_d(\text{CH}_2)$	-5.9	3064.9	-17.8	3076.8	3175.2	3059.0	3047
$\nu_d(\text{CH}_3) + \nu_d(\text{CH})$	-6.8	3010.7	-18.0	3021.9	3118.6	3003.9	2995
$\nu_d(\text{CH})$	-10.2	2991.2	-21.2	3002.2	3098.2	2981.0	2972
$\nu_d(\text{CH}_3)$	-9.7	2986.0	-20.5	2996.8	3092.7	2976.3	2970
$\nu_d(\text{CH}_2)$	-9.9	2982.8	-20.7	2993.6	3089.4	2972.9	2931
$\nu_d(\text{CH}_3)$	0	2931.9	-10.2	2942.1	3036.2	2941.0	2928
$\delta(\text{CH}_2)$	-2.3	1491.8	6.3	1483.2	1530.6	1489.5	1500
$\delta(\text{CH}_2) + \delta(\text{CH}_3)$	-2.7	1465.1	6.3	1456.1	1502.7	1462.4	1456
$\delta_d(\text{CH}_3)$	-1.7	1451.1	7.5	1441.9	1488.0	1449.4	1444
$\delta(\text{CH})$	5.9	1405.7	15.7	1395.9	1440.6	1411.6	1406
$\delta_d(\text{CH}_3)$	-4.9	1377.2	5.2	1367.1	1410.8	1372.3	1369
$\delta(\text{CH})$	4.2	1262.3	15.9	1250.6	1290.6	1266.5	1264
$\tau(\text{CH})$	10.3	1165.3	23.3	1152.3	1189.2	1175.6	1165
$\delta(\text{CCH}) + \omega(\text{CH}_2)$	3	1143.6	16.3	1130.3	1166.5	1146.6	1143
$\tau(\text{CH}_2)$	-0.1	1134.0	13.3	1120.6	1156.5	1133.9	1130
$\delta(\text{CCH}) + \delta(\text{CH}_2)$	1.7	1106.3	15.4	1092.6	1127.6	1108.0	1103
$\tau(\text{CH}_2)$	0.5	1024.4	15.3	1009.6	1041.9	1024.9	1022
$\tau(\text{CH}_3) + \nu_d(\text{CCO})$	0.8	954.9	16.4	939.3	969.3	955.7	951
$\tau(\text{CH}_2)$	-0.4	896.5	16.1	880.0	908.2	896.1	893
$\nu_d(\text{CCO})$	10.5	827.6	27.8	810.3	836.2	838.1	829
$\nu_d(\text{CCO})$	-1.6	758.6	16.7	740.3	764.0	757.0	748

a) this work

b) B3LYP/6-311++G(2d,2p)

c) obs(Ne) – scaled

Table 5.3: Observed and calculated (scaled) absorption for propylene oxide. All positions in cm^{-1}

5.3.2. The Ethanol-Propylene Oxide Hydrogen Bonded Complex.

There are six conformers of the ethanol-propylene oxide complex.²¹ In Figure 5.3, the six conformers are presented along with the MP2/6-311++G(2d,2p)//B3LYP/6-311++G(2d,2p) computed relative energies. Based on these predicted relative energies it is likely that all would be present. In fact, all were accounted for in the gas-phase by microwave spectroscopy.²¹ In the present experiments, the hydrogen-bound dimers are likely born in the gas phase just before or upon deposition of the matrix so it would be expected that all conformers would be present in these matrix isolation experiments as well.

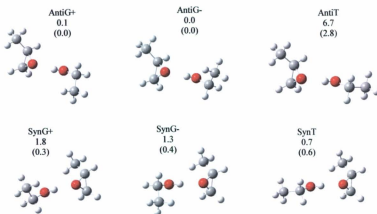


Figure 5.3: Six conformers of the ethanol-propylene oxide hydrogen bonded complex. The MP2/6-311++G(2d,2p)//B3LYP/6-311++G(2d,2p) relative free Gibbs energies and (enthalpies) in kJ mol⁻¹ are also provided.

In order to prepare the ethanol-propylene oxide hydrogen bonded complex, propylene oxide vapor was added to a 1:3000 ethanol:neon mixture. At this concentration of ethanol there were no ethanol homodimers observed, but at higher concentrations dimers were observed. Mixtures with various concentrations of propylene oxide were used. In Figure 5.4 (A) the experimental neon matrix infrared spectra, in the hydrogen-bonded O-H stretch region ($3350\text{-}3650\text{ cm}^{-1}$) are presented. The bottom trace (a) is the spectrum taken following deposition of the 1:3000 ethanol:neon mixture and trace b was recorded following deposition of a 1:200 (15:3000) propylene oxide:neon mixture. Traces c, d, e, and f are the spectra taken after deposition of the 1:3000 ethanol:neon with 2, 3, 3, 5 and 15 parts, respectively, of propylene oxide. A broad band centred at 3505.3 cm^{-1} is observed to grow in with increasing propylene oxide concentration and a shoulder to the red of this main band is observed at 3464.3 cm^{-1} . This main band is assigned to the O-H stretch which is significantly red-shifted from the ethanol monomer (3680.6 cm^{-1}) due to the hydrogen bonding interaction. The O-H stretch is predicted to absorb between 3532 and 3543 cm^{-1} for the six conformers which would not be expected to be resolved in these experiments. The observed position of the O-H stretch agrees quite well with these computed values (see Figure 5.4 B and Table 5.4). The resolved shoulder at 3464.3 cm^{-1} has no activity upon annealing for an hour at 12 K with respect to the main band. It is possible that this band is due to a trimer involving two propylene oxides or that it is due to a different matrix site which is stable even at 12 K.

All the new bands observed in these experiments are listed in Table 5.4 and all are tentatively assigned. The new bands in the $500\text{-}920\text{ cm}^{-1}$ region are displayed in Figure

5.5 compared with the predicted spectrum for the AntiG+ conformer.

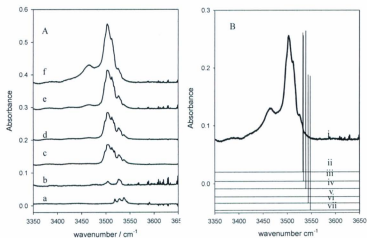


Figure 5.4: A) Infrared spectra in the 3350-3650 cm⁻¹ region of mixtures deposited at 4.2 K, (a) ethanol: neon 1:3000 (b) propylene oxide: neon 1:200, and at the ethanol: propylene oxide ratios in neon of (c) 1:2:3000 (d) 1:3.3:3000 (e) 1:5:3000, and (f) 1:15:3000. B) Infrared spectra in the the 3350-3650 cm⁻¹ region of mixture deposited at 4.2 k, (i) EtOH/PO/Ne 1:15:3000, (ii-vii) the predicted frequencies of OH mode in all possible geometries of EtOH/PO complexes.

Approximate description	Calculated	Observed / cm^{-1}
$\nu(\text{OH})$	3532 - 3543	3505.3 br
$\nu(\text{OH})$ site shift or trimer		3464.3 br
$\delta_s(\text{CH}_3)$	1377 - 1381	1380.8
COH bend	1303.8 (antiT)	1303.2
COH bend	1300.4 (synT)	1297.8
$\nu(\text{CCO}) + \tau(\text{CH}_3)$	1093 (antiT, synT)	1105.1 sh
$\nu(\text{COH}) + \tau(\text{CH}_3)$	1085 (antiG+, antiG-, synG+, syn G-)	1088.4 sh
$\nu(\text{CCO}) + \tau(\text{CH}_3)$	1042 (antiG+, antiG-, synG+, syn G-)	1059.4
$\nu(\text{COH}) + \tau(\text{CH}_3)$	1033 (antiT, synT)	1046.2
$\nu(\text{CCO})$	871 - 884	881.1
$\tau(\text{OH})$	622 - 627	566.6

Table 5.4: New bands observed after deposition of 1:15:3000 ethanol:propylene oxide:Ne, their tentative assignments, and comparison with the calculated and scaled (equation) infrared spectra.

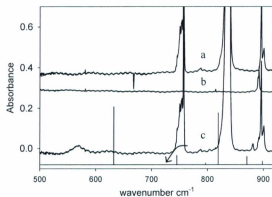


Figure 5.5: Neon matrix infrared spectra of a) 1 part in 200 propylene oxide, b) 1 part in 3000 ethanol and c) 1:15:3000 ethanol:propylene oxide:neon in the 500 to 920 cm^{-1} region.

In Figure 5.6, the 1020–1400 cm^{-1} region is displayed and compared with calculated spectra for all six conformers showing some tentative assignments. The magnitudes of the errors between the observed and predicted fundamentals are the same in sign and similar in magnitude to those seen for the monomers. For example, the primarily CCO stretching vibrations between 1040 and 1060 cm^{-1} in the complexes are predicted to be $\sim 15 \text{ cm}^{-1}$ to the red of the observed bands, similar to the difference between predicted and observed CCO band of ethanol. Few of the predicted infrared bands are actually observed because many of the fundamentals associated with the monomers shift only slightly upon complexation, thereby masking the bands associated with the hydrogen bonded complex. For example, the strong band predicted to occur at 820 cm^{-1} (see Figure. 5.5) is masked by the strong band associated with the CCO asymmetric stretch of propylene oxide at 838.1 cm^{-1} which is also predicted to occur at 824 cm^{-1} .

While it was not possible to differentiate between the six conformers of the ethanol-propylene oxide complex in the O-H stretch region, it was possible to somewhat distinguish them in the 1000 to 1400 region (Figure 5.6) where primarily CCO stretching, COH stretching and COH bending vibrations occur. For example, the absorptions at 1105.1 and 1046.2 cm^{-1} can be assigned to the primarily CCO stretch and COH stretch, respectively, of both the antiT and synT conformers whereas the two at 1088.5 and 1059.4 cm^{-1} are assigned to the COH and CCO stretching modes, respectively, of the other four conformers. Unfortunately they cannot be distinguished any further. The two barely resolved maxima at 1303.2 and 1297.8 cm^{-1} can be assigned to the COH bending vibrations of the antiT and synT conformer, respectively.

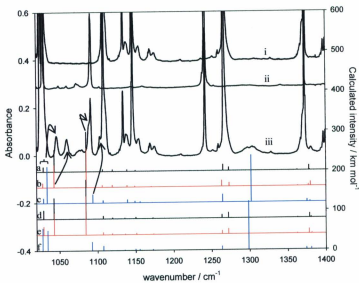


Figure 5.6: Neon matrix infrared spectra of i) 1 part in 200 propylene oxide, ii) 1 part in 3000 ethanol and iii) 1:15:3000 ethanol:propylene oxide:neon in the 1025 to 1400 cm^{-1} regions. Also shown are the computed spectra for the a) AntiG⁺, b) AntiG⁻, c) AntiT, d) SynG⁺, e) SynG⁻, and f) SynT structures.

When mixtures of ethanol-d6 and propylene oxide in neon at a ratio of 1:15:3000 were deposited on the cold KBr window at 4.2 K, new peaks were observed to appear (see Table 5.5 and Figures 5.7 and 5.8). The O-D stretch is observed at 2591.9, significantly red-shifted from the O-D stretch in isolated d6-ethanol (2715.4 cm^{-1}) indicating a hydrogen-bonded species. The H/D observed for the complex is shifted a factor of 1.352, quite similar to that computed for the hydrogen bonded complex, 1.363, and that observed between ethanol and ethanol-d6, 1.355. The only other mode observed for both the H and D isotopomer complexes was the COH/D bend with observed and computed isotopic shifts of 1.251 and 1.260, respectively. Like the fully ^1H experiments, only a few new bands were observed. These bands and their assignments are listed in Table 5.5.

Based on these matrix experiments and the associated calculations, we have observed and partially characterized, by infrared spectroscopy, the ethanol/propylene oxide hydrogen-bonded complex in a neon matrix.

approximate description	calculated	Observed / cm^{-1}
$\nu(\text{OD})$		2591.9 br
$\nu(\text{OD})$ site shift?	2585-2592	2564.7 br
$\nu(\text{CCO}) + \nu(\text{CD}_2)$	1166.6 (antiG+, antiG-, synG+, syn G-)	1183.7
$\delta(\text{CD}_2)$	1130.4 (antiT, synT)	1125.8
		1083.4
$\delta_s(\text{CD}_2)$	1082.1 (antiG+, antiG-, synG+, syn G-)	1070.5
COD bend	1034.5 (antiT, synT)	1041.4
$\nu(\text{CO})$	964.1 (antiG+, antiG-, synG+, syn G-)	973.4

Table 5.5: New bands observed after deposition of 1:15:3000 d_6 -ethanol: propylene oxide: Ne, their tentative assignments, and comparison with the calculated and scaled (equation) infrared spectra.

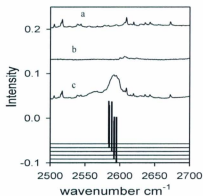


Figure 5.7: FTIR spectra in the 2500 to 2700 cm^{-1} region of a) 1 part in 200 propylene oxide, b) 1 part in 3000 d_6 -ethanol and c) 1:15:3000 d_6 -ethanol:propylene oxide:neon as well as the computed spectra for the six hydrogen bonded complexes.

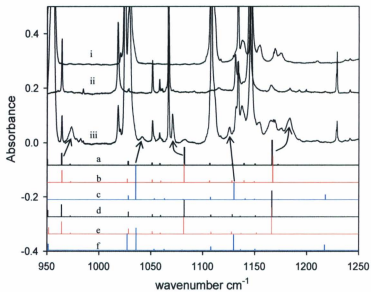


Figure 5.8: Neon matrix infrared spectra of i) 1 part in 200 propylene oxide, ii) 1 part in 3000 d6-ethanol and iii) 1:15:3000 d6-ethanol:propylene oxide:neon in the 1025 to 1400 cm^{-1} regions. Also shown are the computed spectra for the a) AntiG+, b) AntiG-, c) AntiT, d) SynG+, e) SynG-, and f) SynT structures.

5.3.3 The 2-Fluoroethanol-Propylene Oxide Hydrogen Bonded Complex

2-Fluoroethanol (FE) has two main conformers depending on the torsional angles $\tau_{\text{O-C-C-F}}$ and $\tau_{\text{H-O-C-C}}$, which are gauche and trans. Furthermore, the fluorine atom can enable weak intramolecular interactions with the hydroxyl hydrogen atom and the fluorine which comprises a third conformer. The IR spectrum of pure 2-fluoroethanol in a neon matrix shows a strong band at 3653.8 cm^{-1} and a weaker resolved shoulder at 3657.6 cm^{-1} assigned to the gauche and trans conformers, respectively.⁴³ There was no evidence for the intramolecularly hydrogen bonded conformer.

When samples of FE/PO/Ne gas were deposited on the KBr substrate at 4.2 K five new features were observed to grow that were not present in either of the pure 2-fluoroethanol or propylene oxide spectra (see Table 5.6). Among these new bands was the O-H stretch of FE which was observed to shift substantially, 191 cm^{-1} to 3462.9 cm^{-1} on complexing with propylene oxide (Figure 5.9).

The structures of 2-fluoroethanol complexes are divided into three groups: compact gauche, open gauche, and trans conformers (see Appendix 18). The compact gauche structures are calculated to be more stable than the open gauche and trans conformers, by about 8 kJ mol^{-1} (see Appendix 19). In fact, the only structures observed in the microwave spectroscopy experiments were the three compact structures anti G-g+, anti G+g-, and synG+g-. The experimental spectra in the $950\text{-}1150 \text{ cm}^{-1}$ range are compared to the computed spectra of all 14 isomers in Figure 5.10. From these spectra it is by no means possible to distinguish between the isomers, but the experimental spectra for the hydrogen bound complex are certainly consistent with the structures observed in the

microwave spectra.

Approximate description	Calculated	Observed / cm^{-1}
OH str	3481.6	3462.9
CO str	1094.7	1094.2
CCO str	1075.6	1082.4
C-F str	1016.4	1040.9
CCF bend/CCO bend	501.5	508.2

Table 5.6: New bands observed upon codeposition of 2-fluoroethanol and propylene oxide in solid Neon at 4.2 K.

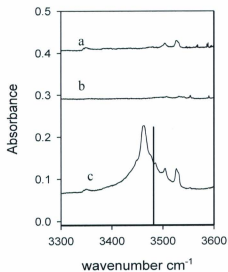


Figure 5.9: FTIR spectra in the 3300 to 3600 cm^{-1} region of a) 1 part in 200 propylene oxide, b) 1 part in 3000 2-fluoroethanol and c) 1:15:3000 2-fluoroethanol:propylene oxide:neon as well as the computed spectra for the six hydrogen bonded complexes.

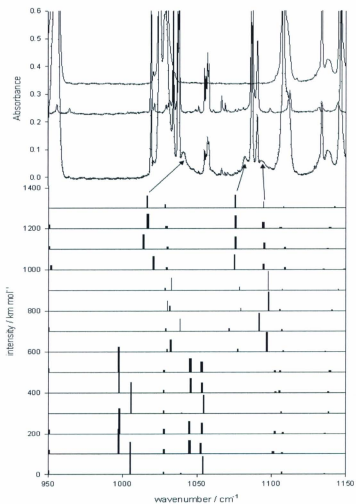
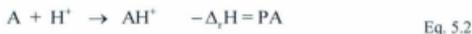


Figure 5.10: FTIR spectra in the 950-1150cm⁻¹ region of fluor ethanol:propylene oxide:neon complexes as well as the computed spectra for the fourteen hydrogen bonded complexes.

5.3.4. Towards a "Universal" Correlation of the Position of the Hydrogen Bonded O-H (X-H) Stretch in Hydrogen Bonded Complexes

It is useful to be able to predict the positions of hydrogen bonded O-H stretching vibrations from available properties of the monomers of which the hydrogen bonded complex is comprised; a sensible correlation can provide further insight into the cause and effect of the shift upon complexation. To this end numerous authors have correlated the positions of hydrogen bonded O-H stretching vibrations with the proton affinities (PA, Eq. 5.2) of various hydrogen bond acceptors.¹⁴



This is reasonable since the acceptor is a base and is partially accepting a hydrogen which has significant proton character. Upon complexation, the hydrogen bonded O-H stretch shifts to the red and it has been observed that as the proton affinity of the base increases, the red shift increases.¹⁴ However, this correlation is obviously only useful for one hydrogen bond donor and many acceptors.

Since the hydrogen bond donor is an acid it might be reasonable that for any one base there may be a correlation between the red-shift of the hydrogen bonded O-H stretch and the gas-phase acidity (GA) of the hydrogen bond donor,



In Figure 5.11 the reduced hydrogen bonded O-H frequency (μ_f) is plotted against the GA of various hydrogen bond donors for complexes where the hydrogen bond acceptor is either water or dimethyl ether. The reduced frequency is defined in Eq. 5.4

$$\mu_f = \frac{\tilde{\nu}_0 - \tilde{\nu}}{\tilde{\nu}_0}$$

Eq.5.4

where $\tilde{\nu}_0$ is the wavenumber position of the O-H stretch of the monomer and $\tilde{\nu}$ is the hydrogen bonded O-H stretch. The reduced frequency is used, rather than simply the position of absorption, since different monomers can have quite different O-H (or X-H) stretches. It is evident from Figure 5.11 that there is a relationship between the gas-phase acidity and the reduced frequency; as the hydrogen bond donor becomes more acidic—a smaller value for GA—the red shift in the complex hydrogen bonded O-H stretch increases.

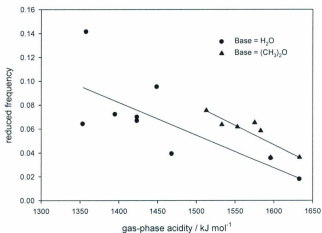


Figure 5.11: Plot of reduced frequency vs gas-phase acidity for various matrix isolated hydrogen-bound dimers with water or dimethyl ether as the hydrogen bond donor.

The goal here is to define a relationship for all combinations of hydrogen bond donors and acceptors over a broad range of hydrogen bond donor and acceptor strengths. The enthalpy of proton transfer ($\Delta_{pr}H$) between the hydrogen bond donor and acceptor is defined as the enthalpy change for the following reaction in the gas phase



This leads to the following expression for the enthalpy of proton transfer.

$$\Delta_{pr}H = GA - PA. \quad \text{Eq.5.6}$$

On the right hand side of Figure 5.12 (filled circles) the reduced frequencies for more than sixty different hydrogen bonded X-H stretches (X=O, N, halogen) are plotted against the enthalpy of proton transfer (see also appendix 20). Clearly as the proton transfer reaction becomes more favourable—less endothermic—the red shift of the hydrogen bonded X-H stretch (or the magnitude of the reduced frequency) increases. At higher proton transfer endothermicity (region I in Figure 5.12, $>600 \text{ kJ mol}^{-1}$) the relationship can be estimated as linear. Between the values of 400-600 kJ mol^{-1} (regions II and III), approximately, there are data points for seven hydrogen-bound dimers that do not fall into line with this linear trend observed for the more endothermic proton transfer reactions. Ault et al.⁴⁴ with a similar plot to Figure 5.12 (a “vibrational correlation diagram”) composed only of hydrogen-bound dimers where the hydrogen bond donors were hydrohalic acids, had first observed this maximum in reduced frequency (region II). The maximum represents an upper limit in the reduction of the position of the X-H stretch from its original non-hydrogen bonded position. It is followed by a reduction in the reduced frequency, so that as the enthalpy of proton transfer decreases (region III), the

position of the X-H stretch begins increasing again toward its non-hydrogen bonded value. Ault et al.⁴⁴ explained the observation of a maximum as the point where the hydrogen-bonded hydrogen becomes a completely shared proton.

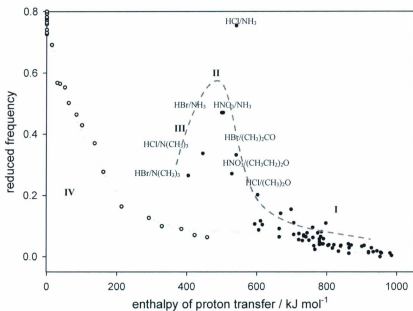


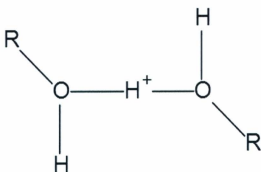
Figure 5.12: Plot of reduced frequencies vs the enthalpy of proton transfer for various matrix isolated hydrogen bonded complexes (filled circles) and gas-phase proton-bound dimers (open circles). The curves are to guide the eye and are discussed in the text.

As the endothermicity of proton transfer decreases, the proton has been transferred to the neutral base producing an ion pair bound through the proton. The vibrational mode which is being observed for these ion pairs is the hydrogen bonded X-H⁺ stretch where XH⁺ is hydrogen bonded to an anion. While the proton transfer from the acid to the base forming free ions is endothermic, the favourable energetics of forming an ion pair makes the transfer possible. We have computed structures for each of the complexes with an enthalpy of proton transfer in the range 400-600 cm⁻¹, (Appendix 21), as well as the HNO₃/N₂ and HCl/H₂O complexes, the latter two fall into region I of Figure 5.12. These calculations are in quite good qualitative agreement with the explanation of Ault et al⁴⁴. Pertaining to the observed maximum in reduced frequency. The HCl, HBr, and HNO₃ hydrogen bonded complexes with ammonia clearly share the hydrogen. A probably equally accurate description of the shared hydrogen is a shared proton. In the HCl and HBr complexes with trimethylamine the acids are indeed predicted to have transferred their protons to the base (region II). An interesting point is also seen in Appendix 22, which is a duplication of Figure 5.12 except with the predicted reduced frequencies for the X-H stretch, compared to the experimentally observed values. For the HNO₃/N₂, HBr/H₂O hydrogen bonded complexes (type I), with higher enthalpies of proton transfer experiment and theory agree very well. For HNO₃/N₂ the predicted and experimental positions for the X-H stretch are 3470 and 3488 cm⁻¹, respectively, and for HBr/H₂O the predicted and experimental values are 2298 and 2310 cm⁻¹, respectively. For the hydrogen bonded complexes in region II, where there is more extensive sharing, and the calculations do not do nearly as well. The predicted and experimentally observed

X-H stretches for the HCl/NH₃ complex are 2048 and 705 cm⁻¹, respectively, and for the HBr/NH₃ complex they are 1583 and 1390 cm⁻¹, respectively. Clearly for these complexes, where the potential for the X-H stretch is expected to be very anharmonic, there can be no confidence placed in these types of calculations based on the harmonic approximation. The poor agreement between calculation and experiment is even true for the complex of HCl and N(CH₃)₃ which resembles an ion pair, but for the HBr/N(CH₃)₃ complex where the proton is more fully transferred to the base, the observed mode much better resembles a "more" harmonic N-H⁺ stretch, the calculations do a more adequate job. The N-H⁺ stretch is observed at 1870 cm⁻¹ and is predicted to be at 1931 cm⁻¹.

There are no known neutral hydrogen bond donor and acceptor pairs that would have identical or even similar values for gas-phase acidities and proton affinities which would result in $\Delta_{PT}H=0$. Symmetric proton-bound dimers (Scheme 5.2) composed of a proton and two identical bases would have a zero enthalpy of proton transfer. The O-H⁺-O symmetric stretch of homogenous and heterogenous proton-bound dimers have been studied in the gas-phase by IRMPD spectroscopy^{42,45,46} and by Ar-tagging.⁴⁷ The effect of the difference in proton affinities on the O-H⁺-O symmetric stretch has also been studied computationally.^{48,49} The results of these studies conclude that for a heterogenous proton-bound dimer, as the difference in proton affinities increases, the asymmetric stretch approaches a value equal to an O-H stretch. The range of proton affinity differences studied is from 0 to -500 kJ mol⁻¹, the span not covered by neutral hydrogen bonds. In Figure 5.12, the position of the O-H⁺-O asymmetric stretching vibrations for all the proton-bound dimers previously studied are plotted (open circles, region IV). The data for

the proton-bound dimers and hydrogen bonded complexes fit together quite nicely if one ignores the complexes of regions II and III. It is also interesting to compare the proton-bound dimers on the leftmost side of the plot in Figure 5.12 with the hydrogen-bonded complexes in region II. In both, the hydrogen, or proton, are shared almost equally between the two complexes and in both sets the reduced frequency approaches a maximum of about 0.8, lending more evidence that the hydrogen-bonded complexes such as the one between HCl and NH₃, are equally sharing the proton.



Scheme 5.2: Symmetric proton-bound dimers composed of a proton and two identical bases.

5.4. Conclusions

Hydrogen bonded complexes between propylene oxide and ethanol, d₆-ethanol, or 2-fluoroethanol have been characterized by matrix isolation spectroscopy in neon matrices at 4.2 K. A two-parameter scaling equation-rather than a scaling factor-was

derived to relate the observed infrared absorptions of ethanol, propylene oxide, d6-ethanol and 2-fluoroethanol, to the calculated infrared absorptions. With this scaling equation we are better equipped to assign bands to the hydrogen bonded complexes based on the computed spectra.

The hydrogen bonded X-H stretching frequencies have been correlated to known physical properties of both the hydrogen bond donor and acceptor. The gas phase acidity and proton affinity, of the hydrogen bond donor and acceptor, respectively, have been used to obtain an enthalpy of proton transfer, which is shown to correlate well with the observed red shifts of the hydrogen bonded X-H stretches for more than 60 hydrogen bonded complexes. Hydrogen-bonded complexes with enthalpies of proton transfer between the acid and base which are endothermic by between 400 and 600 kJ mol⁻¹ are shown to "share" the hydrogen/proton in a manner very similar to homogeneous proton-bound dimers or proton-bound dimers composed of bases with similar proton affinities. More data on hydrogen-bound complexes of acids and bases with enthalpies of proton transfer less than 600 kJ mol⁻¹ would be worthwhile to develop a more predictive relationship between the thermochemical values and the position of the X-H stretch. Theoretical studies on these complexes would also be beneficial.

5.5. Acknowledgments

The Natural Sciences and Engineering Research Council (NSERC) of Canada is gratefully acknowledged for their generous funding. The authors also wish to thank ACE-Net for the computational resources. E Jewer is grateful for a summer NSERC USRA.

5.6 References.

- (1) Burneau, A.; Loutellier, A.; Schriver, L. *J. Mol. Struct.* **1980**, *61*, 397.
- (2) Luck, W. A. P.; Schrems, O. *Spectrosc. Lett.* **1980**, *13*, 719.
- (3) Schrems, O.; Oberhoffer, H. M.; Luck, W. A. P. *Mol. Struct.* **1982**, *80*, 129.
- (4) Schrems, O.; Oberhoffer, H. M.; Luck, W. A. P. *J. Phys. Chem.* **1984**, *88*, 4335.
- (5) Andrews, L.; Johnson, G. L.; Davis, S. R. *J. Phys. Chem.* **1985**, *89*, 1710.
- (6) Desbat, B.; Lassegues, J. C. *J. Chem. Phys.* **1979**, *70*, 1824.
- (7) Loutellier, A.; Schriver, L.; Burneau, A.; Perchard, J. P. *J. Mol. Struct.* **1982**, *95*, 37.
- (8) Loutellier, A.; Schriver, L.; Burneau, A.; Perchard, J. P. *J. Mol. Struct.* **1982**, *82*, 165.
- (9) Schriver, L.; Loutellier, A.; Burneau, A. *Chem. Phys. Lett.* **1979**, *60*, 471.
- (10) Astrand, P. O.; Karlström, G.; Engdahl, A.; Nelander, B. *J. Chem. Phys.* **1995**, *102*, 3534.
- (11) Barnes, A. J.; Beech, T. R. *Chem. Phys. Lett.* **1983**, *94*, 568.
- (12) Engdahl, A.; Nelander, B. *J. Chem. Soc., Faraday Trans.* **1992**, *88*, 177.
- (13) Tse, Y. C.; Newton, M. D.; Allen, L. C. *Chem. Phys. Lett.* **1980**, *75*, 350.
- (14) Sang, W. H.; Kim, K. *J. Mol. Struct.* **1999**, *475*, 43.
- (15) Zhang, K. X.; Lewars, E. G.; March, R. E.; Parnis, J. M. *J. Phys. Chem.* **1993**, *97*, 4320.
- (16) Kim, K.; Sang, W. H. *J. Phys. Chem.* **1996**, *100*, 17124.
- (17) Jasien, P. G.; Stevens, W. J. *J. Phys. Chem.* **1986**, *84*, 3271.
- (18) Lovas, F. J.; Suenram, R. D.; Fraser, G. T.; Gillies, C. W.; Zozom, J. *J. Chem. Phys.*

1988, 88, 722.

- (19) Nelander, B.; Engdahl, A. *J. Chem. Phys.* **1993**, *99*, 4894.
- (20) Bohn, R. B.; Andrews, L. *J. Phys. Chem.* **1989**, *93*, 5684.
- (21) Borho, N.; Xu, Y. *Angew. Chem.* **2007**, *46*, 2276.
- (22) Borho, N.; Xu, Y. *J. Am. Chem. Soc.* **2008**, *130*, 5916.
- (23) Sabo, M. S.; Allison, J.; Gilbert, J. R.; Leroi, G. E. *Applied Spectrosc.* **1991**, *45*, 535.
- (24) Halasinski, T. M.; Godbout, J. T.; Allison, J.; Leroi, G. E. *J. Phys. Chem.* **1996**, *100*, 14865.
- (25) Halasinski, T. M.; Godbout, J. T.; Allison, J.; Leroi, G. E. *J. Phys. Chem.* **1994**, *98*, 3930.
- (26) Godbout, J. T.; Halasinski, T. M.; Leroi, G. E.; Allison, J. *J. Phys. Chem.* **1996**, *100*, 2892.
- (27) Frisch, M. J.; Trucks, G. W.; Schlegel, H. B.; Scuseria, G. E.; Robb, M. A.; Cheeseman, J. R.; Montgomery, J. A., Jr.; Vreven, T.; Kudin, K. N.; Burant, J. C.; Millam, J. M.; Iyengar, S. S.; Tomasi, J.; Barone, V.; Mennucci, B.; Cossi, M.; Scalmani, G.; Rega, N.; Petersson, G. A.; Nakatsuji, H.; Hada, M.; Ehara, M.; Toyota, K.; Fukuda, R.; Hasegawa, J.; Ishida, M.; Nakajima, T.; Honda, Y.; Kitao, O.; Nakai, H.; Klene, M.; Li, X.; Knox, J. E.; Hratchian, H. P.; Cross, J. B.; Adamo, C.; Jaramillo, J.; Gomperts, R.; Stratmann, R. E.; Yazyev, O.; Austin, A. J.; Cammi, R.; Pomelli, C.; Ochterski, J. W.; Ayala, P. Y.; Morokuma, K.; Voth, G. A.; Salvador, P.; Dannenberg, J. J.; Zakrzewski, V. G.; Dapprich, S.; Daniels, A. D.; Strain, M. C.; Farkas, O.; Malick, D. K.; Rabuck, A. D.; Raghavachari, K.; Foresman, J. B.; Ortiz, J. V.; Cui, Q.; Baboul, A. G.; Clifford, S.;

- Cioslowski, J.; Stefanov, B. B.; Liu, G.; Liashenko, A.; Piskorz, P.; Komaromi, I.; Martin, R. L.; Fox, D. J.; Keith, T.; Al-Laham, M. A.; Peng, C. Y.; Nanayakkara, A.; Challacombe, M.; Gill, P. M. W.; Johnson, B.; Chen, W.; Wong, M. W.; Gonzalez, C.; Pople, J. A.; . Gaussian 03 ed.; Gaussian, Inc.: Wallingford, 2004.
- (28) Kakar, R. K.; Quade, C. R. *J. Chem. Phys.* **1980**, *72*, 4300.
- (29) Dothe, H.; Lowe, M. A.; Alper, J. S. *J. Phys. Chem.* **1989**, *93*, 6632.
- (30) Ehbrecht, M.; Huisken, F. *J. Phys. Chem. A* **1997**, *101*, 7768.
- (31) Shaw, R. A.; Wieser, H.; Dutler, R.; Rauk, A. *J. Am. Chem. Soc.* **1990**, *112*, 5401.
- (32) Van der Veken, B. J.; Coppens, P. *J. Mol. Struct.* **1986**, *142*, 359.
- (33) Schiel, D.; Richter, W. *J. Chem. Phys.* **1983**, *78*, 6559.
- (34) Coussan, S.; Bouteiller, Y.; Perchard, J. P.; Zheng, W. Q. *J. Phys. Chem. A* **1998**, *102*, 5789.
- (35) Scott, A. P.; Radom, L. *J. Phys. Chem.* **1996**, *100*, 16502.
- (36) Gornicka, E.; Rode, J. E.; Raczynska, E. D.; Dasiewicz, B.; Dobrowolski, J. C. *Vib Spectrosc.* **2004**, *36*, 105.
- (37) Anderson, M. P.; Uvdal, P. *J. Phys. Chem. A* **2005**, *109*, 2937.
- (38) Rajabi, K.; Fridgen, T. D. *J. Chem. Phys. A* **2008**, *112*, 23.
- (39) Atkins, C. G.; Rajabi, K.; Gillis, E. A. L.; Fridgen, T. D. *J. Phys. Chem. A* **2008**, *112*, 10220.
- (40) Halls, M. D.; Velkovski, J.; Schlegel, H. B. *Theor. Chem. Acc* **2001**, *105*, 413.
- (41) Palafox, M. A. *Int. J. Quant. Chem.* **2000**, *77*, 661.
- (42) Fridgen, T. D. *Mass Spectrom. Rev.* **2009**, *28*, 586.

- (43) Perttola, M.; Murto, J.; Kivenen, A.; Turunen, K. *Spectrochimica Acta. A: Mol Spectrosc.* **1978**, *34*, 9.
- (44) Ault, B. S.; Stelnback, E.; Pimentel, G. C. *J. Phys. Chem* **1975**, *79*, 615.
- (45) Elyer, J. R. *Mass Spectrom. Rev* **2009**, *28*, 448.
- (46) Fridgen, T. D.; Maitre, P.; MacAleese, L.; Boissel, P.; McMahon, T. B.; Lemaire, J. *Phys. Chem. Chem. Phys.* **2005**, *7*, 2747.
- (47) Roscioli, J. R.; McCunn, L. R.; Johnson, M. A. *Science*. **2007**, *316*, 249.
- (48) Fridgen, T. D. *J. Phys. Chem. A*. **2006**, *110*, 6122.
- (49) Burt, M. B.; Fridgen, T. D. *J. Phys. Chem. A*. **2007**, *111*, 10738.
- (50) Lowe, M. A.; Alper, J. S.; Kawiecki, R.; Stephns, P. J. *J. Phys. Chem.* **1986**, *90*, 41.
- (51) Schriver, A.; Silivi, B.; Millard, D.; Perchard, J. P. *J. phys. Chem.* **1977**, *81*, 2095.
- (52) Barnes, A. J.; Lasson, E.; Nielsen, C. J.; . *J. Mol. Struct.* **1994**, *322*, 165.
- (53) Goebel, J. R.; Antle, K. A.; Ault, B. S.; Del Bene, J. E. *J. Phys. Chem. A*. **2002**, *106*, 6406.
- (54) Mielke, Z.; Wierzejewska, M.; Olbert, A.; Krajewska, M.; Tokhadze, K. G. *J. Mol. struct.* **1997**, *436-437*, 339.
- (55) Olbert, M. A.; Mielke, Z.; Tokhadze, K. G. *Chem. Phys.* **2002**, *280*, 211.
- (56) George, L.; Sander, W. *Spectrochimica Act. A*. **2004**, *60*, 3225.
- (57) Heikkilae, A.; Pettersson, M.; Lundell, J.; Khriachtchev, L.; Raesaenen, M. *J. Phys. Chem A*. **1999**, *103*, 2945.
- (58) Couzi, M.; Le Calve, J.; Van Huong, P.; Lascombe, J. *J. Mol. Struct* **1970**, *5*, 363.
- (59) Goebel, J. R.; Ault, B. S.; Del Bene, J. E. *J. Phys. Chem. A*. **2001**, *105*, 11365.

- (60) Goebel, J. R.; Ault, B. S.; Del Bene, J. E. *J. Phys. Chem. A* **2000**, *104*, 2033.
- (61) Engdahl, A.; Nelander, B.; Karlstroem, G. *J. Phys. Chem. A* **2001**, *105*, 8393.
- (62) Lundell, J.; Jolkkonene, S.; Khriachtchev, L.; Pettersson, M.; Rasanen, M. *Chem. Eur. J.* **2001**, *7*, 1670.
- (63) Coussan, S.; Alikhani, M. E.; Perchard, J. P.; Zheng, W. Q. *J. Phys. Chem. A* **2000**, *104*, 5475.
- (64) Sundararajan, K.; Viswanathan, K. S. *J. Mol. Struct.* **2006**, *798*, 109.
- (65) Coussan, S.; Bouteiller, Y.; Perchard, J. P.; Zheng, W. Q.; Talbot, F. *Chem. Phys.* **1999**, *110*, 10046.
- (66) Barnes, A. J.; Hallam, H. E. *Trans. Faraday Soc.* **1970**, *66*, 1920.
- (67) Bakkas, N.; Bouteiller, Y.; Louteillier, A.; Perchard, J. P.; Racine, S. *J. Chem. Phys.* **1993**, *99*, 3335.
- (68) Ault, B. S.; Balboa, A.; Tevault, D.; Hurley, M. *J. Phys. Chem. A* **2004**, *108*, 10094.
- (69) Engdahl, A.; Nelander, B. *J. Chem. Phys.* **1989**, *91*, 6604.
- (70) Engdahl, A. *Chem. Phys.* **1993**, *178*, 305.
- (71) Nelander, B. *J. Chem. Phys.* **1980**, *72*, 77.
- (72) Barnes, A. J.; Bentwood, R. M.; Wright, M. *J. Mol. Struct.* **1984**, *118*, 97.
- (73) Rozenberg, M.; Loewenschuss, A. *J. Phys. Chem.* **2009**, *113*, 4963.
- (74) Engdahl, A.; Nelander, B. *J. Phys. Chem.* **1986**, *90*, 4982.
- (75) Schriver, A.; Schriver, L.; Perchard, J. P. *J. Mol. Spectrosc.* **1988**, *127*, 125.

(76) Dozova, N.; Krim, L.; Alikhani, E. M.; Lacombe, N. *J.Phys.Chem.A.* **2005**, *109*, 10273.

Chapter 6

Conclusions and Future work

Mass spectrometry and matrix isolation techniques are valuable methods that can be used to provide an in depth understanding of structure of complexes as well as yield proper identification and characterization of both the ionic and the neutral species. Theoretical calculations in conjunction with experimental results produce accurate structural representations of these species. Intermolecular interactions, particularly non-covalent, play a significant role in determining the conformations and stabilization of ions found in many biological processes. Therefore, classifying the structures and stabilities of ions produced through interactions between nucleobases and metal ions is central to understanding how these ions influence biological processes.

The interactions between the copper (II) cation and uracil in the gas phase have been studied by Fourier transform ion cyclotron resonance (FTICR) mass spectrometer. $[\text{Cu}(\text{Ura})(\text{Ura-H})]^+$ ions are the most abundant species resulting from the interaction between copper (II) and uracil. These complexes have been examined under different methods of fragmentation such as SORI/CID and IRMPD, to characterize their structures. To give a picture of the decomposition pathways within the different species, density functional theory calculations have been performed for all the structures at B3LYP/6-31+G(d,p) level of theory. Furthermore, Single point calculations were done on all optimized geometries using B3LYP/6-311+G(2df,2p) on C,N,O, and H and 6-311+G on Cu to obtain more accurate thermochemical data. The potential energy surfaces for the

fragmentations were calculated at the same levels of theory that were used for geometry optimizations. MS/MS experiments show that the lowest energy decomposition pathway for $[\text{Cu}(\text{Ura})(\text{Ura-H})]^+$ is not loss of uracil, but is loss of HNCO and followed by the loss of HCN. This loss has been confirmed by using isotopic labeling species which indicate that the N3, C2 and very likely O2 centers are expelled.

To investigate how the metal ion-uracil complexes depend on the metal identity, a series of different divalent metal ions were examined with uracil nucleobase. MS/MS experiments show that the primary decomposition pathway for all $[\text{M}(\text{Ura-H})(\text{Ura})]^+$ except where M= (Sr, Ba, and Pb) is not the loss of uracil, but is the loss of HNCO as a primary fragment. It was observed that under CID and the softer IRMPD conditions $[\text{Sr}(\text{Ura-H})(\text{Ura})]^+$, $[\text{Ba}(\text{Ura-H})(\text{Ura})]^+$ and $[\text{Pb}(\text{Ura-H})(\text{Ura})]^+$ behave quite differently and these complexes dissociate by losing uracil directly. Also, the decomposition pathway for $[\text{Ca}(\text{Ura-H})(\text{Ura})]^+$ under IRMPD conditions show a loss of HNCO, however, when using SORI-CID a loss of uracil is observed. The binding energies between neutral uracil and $[\text{M}(\text{Ura-H})]^+$, M= Zn, Cu, Ni, Fe, Cd, Pd, Mg, Ca, Sr, Ba, and Pb have also been calculated. The differences in the uracil binding energies are consistent with the experimentally-observed differences in fragmentation pathways.

The IRMPD spectroscopy technique is another technique which is used to determine the structure of gaseous ions. Other purposes include gaining insight into the structure of the interaction between uracil and lead (II) ions by using IRMPD spectroscopy in the gas phase in the 3200-3900 cm^{-1} region. The IRMPD spectroscopy experiments will greatly enable us to sort out various structures and to associate

structures to the structures probed in the experiments.

The structures of three ion molecule complexes of $[\text{Pb}(\text{Ura-H})]^+$ have been explored by IRMPD spectroscopy in the gas phase. A complex of $[\text{Pb}(\text{Ura-H})]^+$ with uracil, $[\text{Pb}(\text{Ura-H})(\text{Ura})]^+$, or the singly or doubly water solvated complexes, $[\text{Pb}(\text{Ura-H})(\text{H}_2\text{O})]^+$ and $[\text{Pb}(\text{Ura-H})(\text{H}_2\text{O})_2]^+$, have irradiated with tunable infrared radiation in the N-H/O-H stretching region ($3200\text{--}4000\text{ cm}^{-1}$) to produce IRMPD spectra which were compared with IR spectra computed using B3LYP/6-31+G(d,p) for various isomers. In all cases, the computed spectra for the lowest energy structures agree very well with the experimental IRMPD spectrum. All these structures involved a $[\text{Pb}(\text{Ura-H})]^+$ core which is deprotonated at N3 and has lead bound to either N3 and O4 or N3 and O2. Our results suggest that the $[\text{Pb}(\text{Ura-H})]^+$ structure that is deprotonated at N1 and lead is bound to N1 and O2 is not an observable contributor to the electrosprayed complexes. $[\text{Pb}(\text{Ura-H})(\text{Ura})]^+$ was found to have a tetradentate coordinated lead while the water molecules in $[\text{Pb}(\text{Ura-H})(\text{H}_2\text{O})]^+$ and $[\text{Pb}(\text{Ura-H})(\text{H}_2\text{O})_2]^+$ were determined to be directly coordinated to lead, the first also hydrogen bonded to one carbonyl oxygen.

Matrix isolation technique, like mass spectroscopy, is a valuable tool for investigating the types of molecular complexes. This technique in combination with spectroscopy is a convenient technique which can be used to study both weak and strong molecular complexes. In addition, combination of the experimental results with theoretical calculations allows elucidation of the nature of intermolecular mode and to determination of the vibrational assignments of the complexed molecules.

The hydrogen bonding between alcohols as proton donors and propylene oxide as a

proton acceptor were studied in neon matrices. The infrared absorption spectra of hydrogen-bonded complexes of propylene oxide with either ethanol or 2-fluoroethanol have been recorded in neon matrices. The results indicate that hydrogen-bonded complexes were formed with propylene oxide as the hydrogen bond acceptor and either ethanol or 2-fluoroethanol as the hydrogen bond donors. The features assigned to the O-H stretch were red-shifted by 175 and 193 cm^{-1} for the ethanol and 2-fluoroethanol containing complexes, respectively. The difference in red shifts can be accounted for due to the greater acidity of 2-fluoroethanol. Deuterium isotope experiments were conducted to help confirm the assignment of the O-H stretch for the complexes. As well, structures and IR spectra were calculated using B3LYP/6-311++G(2d,2p) calculations and were used to compare with the experimental spectra. The use of a "scaling equation" rather than a scaling factor was used and is shown to greatly increase the utility of the calculations when comparing with experimental spectra. An examination of the O-H stretching red shifts for many hydrogen-bound complexes reveals a relationship between the shift and the difference between the acidity of the hydrogen bond donor and the basicity of the hydrogen bond acceptor (the enthalpy of proton transfer). Both hydrogen-bonded complexes and proton-bound complexes appear to have a maximum in the reduced frequency value which corresponds to complexes where the hydrogen/proton is equally shared between the two bases.

Investigation of the interactions of metal ions with nucleotides and nucleosides provide important information for a variety of biological process, including the ability of the interactions between metals and nucleosides to influence the stabilization of the

double strand helix in DNA. Based upon work done in this thesis, future studies can focus on expanding the study of the fundamental interactions of metal ions. This can be done by selecting different nucleobases as well as different metals from those used in this thesis, such as thymine. Future work could focus on determining the metal ion attachment and binding site of various nucleotides and nucleosides. Furthermore, MS/MS studies can help identify the structures of the gas phase metal ion-nucleotide systems.

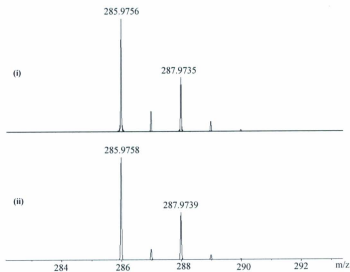
Results obtained from the interaction of lead and uracil in this work can be used in future IRMPD spectroscopic studies to identify isomers that are similar to the experimental results but are found within a different region. Other studies will focus on investigating the structure of the interaction between uracil and divalent cations such as Ba, Sr, and Ca by using IRMPD spectroscopy in the gas phase.

On the other hand, the intermolecular interactions between different proton donors and various proton acceptors will be studied in the solid matrices. Further work involving the scaling used in this thesis could provide a foundation to developing a universal model that could allow the prediction of IR spectra exclusively based on theory.

Appendices

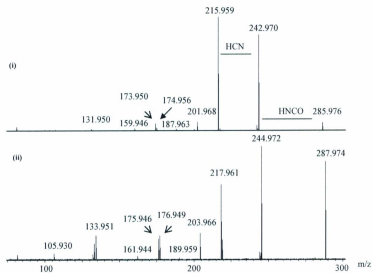
Appendix 1

(i) ESI FTICR mass spectrum showing the accurate mass and isotopic distribution for the $[\text{Cu}(\text{Ura-H})(\text{Ura})]^+$ complex (ii) the theoretical mass spectrum for the $[\text{Cu}(\text{Ura-H})(\text{Ura})]^+$ complex.



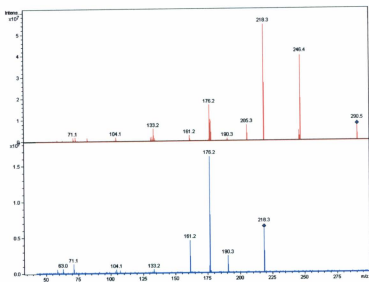
Appendix 2

SORI/CID spectrum of the $[\text{Cu}(\text{Ura-H})(\text{Ura})]^+$ complex obtained after isolating (i) $[\text{}^{63}\text{Cu}(\text{Ura-H})(\text{Ura})]^+$ and (ii) $[\text{}^{65}\text{Cu}(\text{Ura-H})(\text{Ura})]^+$



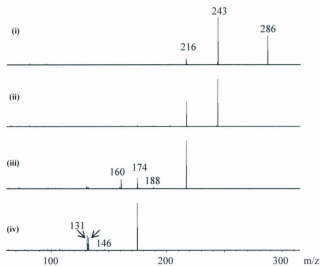
Appendix 3

MS/MS of the main fragment ions of $[\text{Cu}(1,3\text{-}^{15}\text{N-Ura-H})(1,3\text{-}^{15}\text{N-Ura})]^+$ (a) m/z 290.5
(b) m/z 218.3



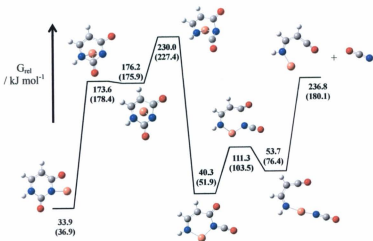
Appendix 4

IRMPD of the main fragment ions (a) m/z 286 (b) m/z 243 (c) m/z 216, and (d) 174



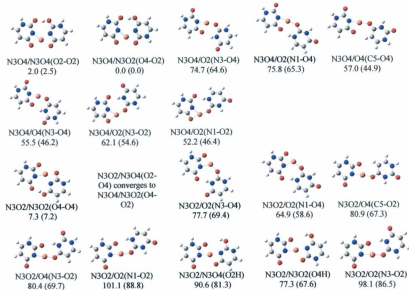
Appendix 5

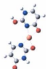
Potential energy surface corresponding to the loss of NCO with the origin in global minimum energy as determined by theoretical methods as well as B3LYP/6-311+G(2df,2p) calculated Gibbs free energies, the relative enthalpies in parentheses



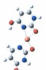
Appendix 6

Twenty-seven possible structures of $[\text{Cu}(\text{Ura-H})(\text{Ura})]^+$. Enthalpies and Gibbs free energies (parentheses) are computed at the MP2/6-311+G(2df,2p)//B3LYP/6-31+G(d,p) level of theory and are in kJ mol^{-1} relative to the lowest energy structure.





N1O2/N3O4(O2Ht)
119.9 (106.4)



N1O2/N3O2(O4Hc)
90.6 (77.5)



N1O2/N3O2(O4Ht)
92.9 (82.2)



N1/O2(N1-O2)
81.9 (68.7)



N1/O2(N3-O2)
77.1 (62.4)



N1O2/N3O4(O2Hc)
104.0 (90.6)



N1/O4(C5-O2)
66.2 (44.6)



N1/O4(N3-O2)
64.0 (50.2)



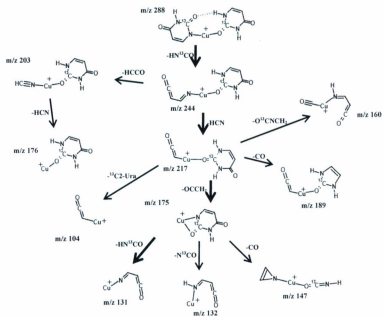
N1/N3O4/O2-O2
90.2 (80.2)



N1/O4
68.9 (47.7)

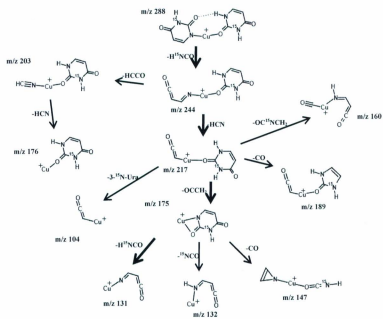
Appendix 7

Proposed fragmentation pathways for the observed fragments from $[\text{Cu}(\text{Ura}-2\text{-}^{13}\text{C}_2\text{H})]^+$ complex.



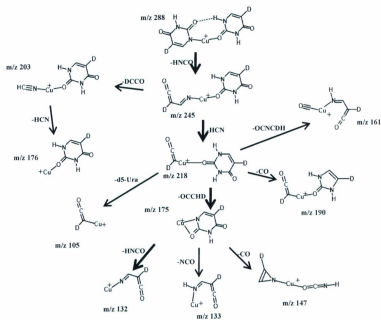
Appendix 8

Proposed fragmentation pathways for the observed fragments from $[\text{Cu}(\text{Ura}-3\text{-}^{15}\text{N})_2\text{-H}]^+$ complex.



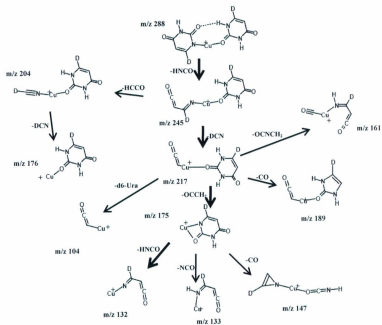
Appendix 10

Proposed fragmentation pathways for the observed fragments from $[\text{Cu}(\text{Ura-d5})_2\text{-H}]^+$ complex.



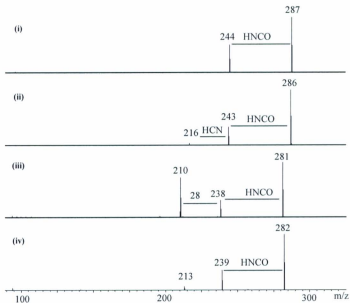
Appendix 11

Proposed fragmentation pathways for the observed fragments from $[\text{Cu}(\text{Ura-d6})_2\text{-H}]^+$ complex.



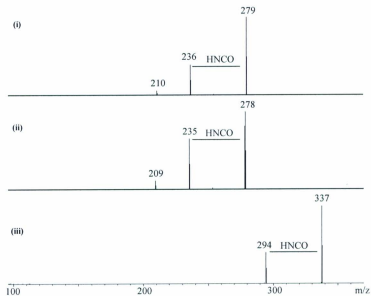
Appendix 12

IRMPD spectra of the $[M(\text{Ura-H})(\text{Ura})]^+$ complex obtained with (i) $[\text{Zn}(\text{Ura-H})(\text{Ura})]^+$,
(ii) $[\text{Cu}(\text{Ura-H})(\text{Ura})]^+$, (iii) $[\text{Ni}(\text{Ura-H})(\text{Ura})]^+$ and (iv) $[\text{Co}(\text{Ura-H})(\text{Ura})]^+$.



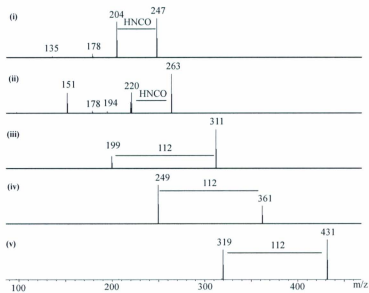
Appendix 13

IRMPD spectra of the $[M(\text{Ura-H})(\text{Ura})]^+$ complex obtained with (i) $[\text{Fe}(\text{Ura-H})(\text{Ura})]^+$,
(ii) $[\text{Mn}(\text{Ura-H})(\text{Ura})]^+$, and (iii) $[\text{Cd}(\text{Ura-H})(\text{Ura})]^+$.



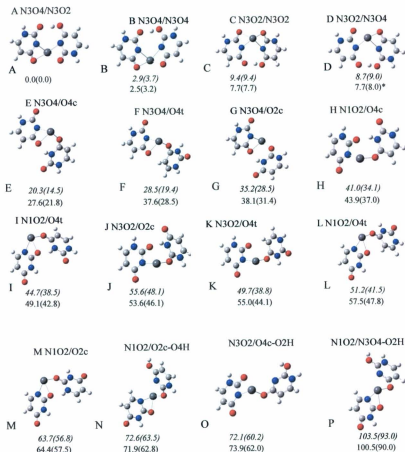
Appendix 14

IRMPD spectra of the $[M(\text{Ura-H})(\text{Ura})]^+$ complex obtained with (i) $[\text{Mg}(\text{Ura-H})(\text{Ura})]^+$, (ii) $[\text{Ca}(\text{Ura-H})(\text{Ura})]^+$, (iii) $[\text{Sr}(\text{Ura-H})(\text{Ura})]^+$, (iv) $[\text{Ba}(\text{Ura-H})(\text{Ura})]^+$, and (v) $[\text{Pb}(\text{Ura-H})(\text{Ura})]^+$



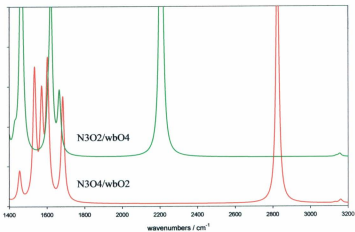
Appendix 15

Sixteen possible B3LYP/6-31+G(d,p) structures of $[\text{Pb}(\text{Ura})(\text{Ura-H})]^+$. Relative enthalpies and 298 K Gibbs energies (in parentheses) are provided in kJ mol^{-1} . The top values in italics are the B3LYP/6-31+G(d,p) thermochemistries and the bottom values are the MP2/6-311++G(2d,p)//B3LYP/6-31+G(d,p).



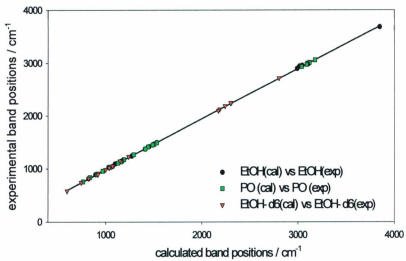
Appendix 16

Comparison of the B3LYP/6-31+G(d,p) predicted IR spectra for the two lowest energy computed $[\text{Pb}(\text{Ura-H})\text{H}_2\text{O}]^+$ structures in the $1400\text{--}3200\text{ cm}^{-1}$ region.



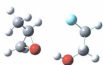
Appendix 17

Plot of experimental vs B3LYP/6-311++G(2d,2p) calculated band positions. The first-order fit is given by equation 5.1.



Appendix 18

Structures of 2-fluoroethanol-propylene oxide complexes. The relative enthalpies and free energies are tabulated in appendix 19.

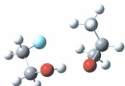


Compact antiG+g-

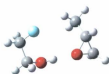


Compact

antiG-g+



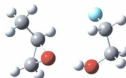
Compact synG+g-



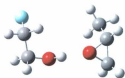
Compact synG-g+



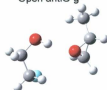
Open antiG+g+



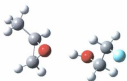
Open antiG-g-



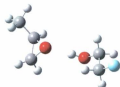
Open synG+g+



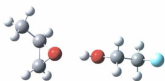
Open synG-g-



Trans antiTg-



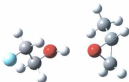
Trans antiTg+



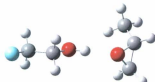
Trans antiTt



Trans synTg-



Trans synTg+



Trans synTt

Appendix 19

Thermochemistries of 2-fluoroethanol-propylene oxide complexes. The shaded rows are structures which have been observed and whose rotational constants have been obtained from microwave spectra.

Structure	G3MP2 Relative Enthalpy and (Relative Energy)/ kJ mol^{-1}	B3LYP/6-311++g(2d,2p) Relative Enthalpy and (Relative Free Energy at 298 °C) / kJ mol^{-1}
Compact antiG+g-	2.22(-2.62)	0.1 (1.59)
Compact antiG-g+	0.0 (0.0)	0.0 (0.0)
Compact synG+g-	0.09 (0.51)	0.66 (4.35)
Compact synG-g+	3.65 (-1.81)	2.41 (3.58)
Open antiG+g+	8.04 (8.17)	6.97 (8.31)
Open antiG-g-	8.04 (7.69)	7.1 (8.14)
Open synG+g+	9.13 (8.59)	7.91 (5.72)
Open synG-g-	8.34(8.77)	7.53 (9.69)
Trans antiTg+	7.45 (-1.35)	7.64(1.93)
Trans antiTg-	7.48 (-1.55)	7.66 (3.67)
Trans antiTt	6.78 (-4.44)	7.89 (3.77)
Trans synTg+	7.22 (-0.33)	8.12 (5.03)
Trans synTg-	6.96 (-0.04)	8.17 (5.98)
Trans synTt	6.44 (-1.51)	8.32 (2.97)

Shaded structures were observed in microwave spectroscopy experiments.

Appendix 20

Table of X-H stretching vibrations for monomers and hydrogen bound complexes, reduced frequencies, gas-phase acidities, proton affinities and the enthalpy of proton transfer for various species included in Figure 5.14.

H-bond Donor	H-bond Acceptor	Reference	X-H str Monomer	X-H str Complex	Reduced Frequency	Acidity (donor)	Proton Affinity (base)	$\Delta_r H$
HBr	H2O	[51]	2559.1	2395	0.064	1353.5	688.8	664.7
HBr	(CH3)3N	[44]**	2540	1870	0.264	1353.5	948.9	404.6
HBr	NH3	[44]**	2540	1390	0.469	1353.5	853.6	499.9
HBr	(CH3)CO	[44]**	2540	1700	0.331	1353.5	812	541.5
HBr	H2O	[44]**	2540	2310	0.091	1353.5	688.8	664.7
HNO3	NH3	[52]	3522	1870	0.469	1357.7	853.6	504.1
HNO3	DEE	[52]	3522	2570	0.27	1357.7	828.4	529.3
HNO3	HNO3	[52]	3522	3216	0.087	1357.7	751.4	606.3
HNO3	H2O	[52]	3522	3024	0.141	1357.7	688.8	668.9
HNO3	CO	[52]	3522	3399	0.035	1357.7	594	763.7
HNO3	NO2	[52]	3522	3441	0.023	1357.7	591	766.7
HNO3	N2	[52]	3522	3488	0.010	1357.7	493.8	863.9
HCl	(CH3)3N	[44]**	2854	1595	0.336	1395	948.9	446.1
HCl	NH3	[44]**	2854	705	0.753	1395	853.6	541.4
HCl	(CH3)2O	[44]**	2854	2280	0.201	1395	792	603
HCl	H2O	[51]	2870	2663	0.072	1395	688.8	706.2
HCl	H2O	[44]**	2854	2540	0.11	1395	688.8	706.2
HCl	H2O2	[53]	2870	2711	0.055	1395	674.5	720.5
t-HONO	DEE	[54]	3572.6	3194.1	0.106	1423.4	828.4	595
t-HONO	acetone	[54]	3572.6	3156.9	0.116	1423.4	812	611.4
c-HONO	H2O	[55]	3412.4	3184.5	0.067	1423.4	688.8	734.6
t-HONO	H2O	[55]	3572.6	3323	0.070	1423.4	688.8	734.6
formic acid	H2O	[56]	3550.4	3212.4	0.095	1449	688.8	760.2
HCN	H2O	[57]	3312	3182	0.039	1468.2	688.8	779.4
CF3CH2OH	DME	[4]	3639.5	3365	0.075	1513	792	721
CHF2CH2OH	DME	[4]	3636.5	3405	0.064	1533	792	741
CH2FCH2OH	PO	This work*	3654	3463	0.053	1553	803.3	749.7
CH2FCH2OH	DME	[3]	3644	3419	0.062	1553	792	761
HF	(iC3H7)2O	[58]***	3962	3350	0.154	1554	855.5	698.5
HF	CH3CN	[58]***	3962	3657	0.077	1554	779.2	774.8
HF	CH3CHO	[58]***	3962	3640	0.081	1554	768.5	785.5
HF	CH3OH	[58]***	3962	3530	0.109	1554	756	798
HF	CH3I	[58]***	3962	3800	0.041	1554	691.7	862.3
H2O2	P(CH3)3	[59]	3590	3215	0.104	1575.3	958.8	616.5
H2O2	Si(CH3)2	[59]	3590	3312	0.077	1575.3	830.9	744.4
H2O2	DME	[60]	3583	3349	0.065	1575.3	792	783.3
H2O2	PH3	[59]	3590	3444	0.041	1575.3	785	790.3
H2O2	H2S	[59]	3590	3456	0.037	1575.3	705	870.3
H2O2	H2O2	[61]	3588	3471.3	0.033	1575.3	674.5	900.8

H2O2	CO	[62]	3587.8	3547.7	0.011	1575.3	594	981.3
EtOH	PO	This work*	3680.6	3505.3	0.048	1583	803.3	779.7
EtOH	DME	[4]	3660	3446	0.058	1583	792	791
EtOH	EtOH	[63]	3660.8	3523.3	0.038	1583	776.4	806.6
C2H2	MeOH	[64]	3288.9	3231.4	0.017	1590	756	834
MeOH	Acetone	[16]	3666.6	3518	0.041	1596	812	784
MeOH	DME	[14]	3666.6	3534.1	0.036	1596	792	804
MeOH	CH3CN	[65]	3666.6	3568	0.027	1596	779.2	816.8
MeOH	MeOH	[66]	3666.6	3540.6	0.034	1596	756	840
MeOH	H2O	[67]	3666.6	3536.1	0.036	1596	688.8	907.2
MeOH	C2H2	[64]**	3663.5	3616.5	0.013	1596	641.4	954.6
H2O	DMMP	[68]	3639	3450	0.052	1633	902.1	731
H2O	NH3	[69]*	3664.8	3455.7	0.057	1633	853.6	779.4
H2O	Acetone	[70,15]	3638	3498	0.038	1633	812	821
H2O	DME	[12]	3638	3505.9	0.036	1633	792	841
H2O	CHO3CH		3638	3535	0.028	1633	768.5	864.5
H2O	H2CO	[71]	3638	3585.1	0.015	1633	712.9	920.1
H2O	HCN	[57]	3638	3594	0.012	1633	712.9	920.1
H2O	H2S	[72]	3638	3536	0.028	1633	705	928
H2O	H2SO4	[73]	3638	3581.9	0.015	1633	699.4	933.6
H2O	H2O	[73]	3638	3573.2	0.018	1633	688.8	944.2
H2O	C2H4	[74]	3638	3640	-0.001	1633	680	953
H2O	SO2	[75]	3638	3598	0.011	1633	676	957
H2O	CH3Cl	[76]	3638	3625.9	0.003	1633	647.3	985.7

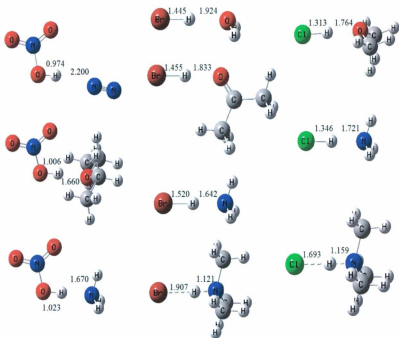
- [51] A. Schriver, B. Silivi, D. Millard, J.P. Perchard, J. phys. Chem, 81 (1977) 2095-2102.
- [52] A.J. Barnes, E. Lasso, C.J. Nielsen, J. Mol. Struct., 322 (1994) 165-174.
- [53] J.R. Goebel, K.A. Antle, B.S. Ault, J.E. Del Bene, J. Phys. Chem. A., 106 (2002) 6406-6414.
Z. Mielke, M. Wierzejewska, A. Olbert, M. Krajewska, K.G. Tokhadze, J. Mol. struct., 436-437 (1997) 339-347.
- [54] M.A. Olbert, Z. Mielke, K.G. Tokhadze, Chem. Phys., 280 (2002) 211-227.
- [56] L. George, W. Sander, Spectrochimica Act. A, 60 (2004) 3225-3232.
A. Heikkilae, M. Pettersson, J. Lundell, L. Khriachtchev, M. Raesaenen, J. Phys. Chem. A, 103 (1999) 2945-2951.
- [57] M. Couzi, J. Le Calve, P. Van Huong, J. Lascombe, J. Mol. Struct, 5 (1970) 363-373.
- [59] J.R. Goebel, B.S. Ault, J.E. Del Bene, J. Phys. Chem. A., 105 (2001) 11365-11370.
- [60] J.R. Goebel, B.S. Ault, J.E. Del Bene, J. Phys. Chem. A., 104 (2000) 2033-2037.
- [61] A. Engdahl, B. Nelander, G. Karlstroem, J. Phys. Chem. A., 105 (2001) 8393-8398.
J. Lundell, S. Jolkkonene, L. Khriachtchev, M. Pettersson, M. Rasanen, Chem. Eur. J., 7 (2001) 1670-1678.
- [62] S. Coussan, M.E. Alikhani, J.P. Perchard, W.Q. Zheng, J. Phys. Chem. A., 104 (2000) 5475-5483.
- [63] K. Sundararajan, K.S. Viswanathan, J. Mol. Struct., 798 (2006) 109-116.
- [64] S. Coussan, Y. Bouteiller, J.P. Perchard, W.Q. Zheng, F. Talbot, Chem. Phys., 110 (1999) 10046-10057.
- [65] A.J. Barnes, H.E. Hallam, Trans. Faraday Soc., 66 (1970) 1920-1931.
- [66] N. Bakkas, Y. Bouteiller, A. Louteillier, J.P. Perchard, S. Racine, J. Chem. Phys., 99 (1993) 3335-3342.
- [67] B.S. Ault, A. Balboa, D. Tevault, M. Hurley, J. Phys. Chem. A., 108 (2004) 10094-10098.
- [68] A. Engdahl, B. Nelander, J. Chem. Phys., 91 (1989) 6604-6612
- [69] A. Engdahl, Chem. phys., 178 (1993) 305-314.
- [70] B. Nelander, J. Chem. Phys., 72 (1980) 77-84.

- [72] A.J. Barnes, R.M. Bentwood, M. Wright, *J. Mol. Struct.*, 118 (1984) 97-102.
[73] M. Rozenberg, A. Loewenschuss, *J. Phys. Chem.*, 113 (2009) 4963-4971.
[74] A. Engdahl, B. Nelander, *J. Phys Chem.*, 90 (1986) 4982-4987.
[75] A. Schriver, L. Schriver, J.P. Perchard, *J. Mol. Spectrosc.*, 127 (1988) 125-142.
[76] N. Dozova, L. Krim, E.M. Alikhani, N. Lacombe, *J. Phys. Chem. A.*, 109 (2005) 10273-10279.

All these complexes are in argon matrices except, * in neon and ** in nitrogen and *** in the gas phase.

Appendix 21

The computed hydrogen bonded complexes of HCl, HBr, and HNO₃ with ammonia, trimethylamine, nitrogen, ammonia, and waters.



Appendix 22

